Heavy neutrino balls and the supermassive dark object at the Galactic center

Faustin Munyaneza

Thesis Presented for the Degree of

DOCTOR OF PHILOSOPHY

in the Department of Physics

UNIVERSITY OF CAPE TOWN

August 1999

To the memory of my mother

Abstract

Massive neutrinos were the first proposed, and still remain the most natural, particle candidate for the dark matter. We investigate here the properties and astrophysical implications of self-gravitating degenerate heavy neutrino matter.

Neutrinos of 10 to 25 keV/c^2 might cluster around the sun forming a halo of a few solar masses and a few light years radius. We calculate the perihelion shifts of planetary and asteroidal orbits that are expected due to the presence of a conjectured degenerate heavy neutrino halo around the sun. While the General Relativistic perihelion shifts are positive, those due to a possible dark matter halo are in general negative. A neutrino mass around $\sim$ 16 keV is consistent with the observed mass excesses within the orbits of various outer planets, as obtained from astrometrical data and Voyager 1 and 2 and Pioneer 10 and 11 ranging data.

We then study the general relativistic effects on degenerate neutrino balls using the Tolman-Oppenheimer-Volkoff (TOV) equations of hydrostatic equilibrium. An extension of the TOV equations is made to describe the detailed properties of supermassive neutrino balls around compact objects such as white dwarfs and neutron stars. We further show that the supermassive compact dark object near Sgr A* at the Galactic center could be an extended object rather than a black hole. In fact these two scenarios can be distinguished by tracking the orbit of one of the fast moving stars near the Galactic center. We finally calculate the emission spectrum of the supermassive compact dark object using the standard accretion theory and show that the calculated radio wave to infrared emission spectrum between $\lambda = 0.3$ cm and $\lambda = 10^{-3}$ cm is consistent with the observations.

Acknowledgments

I would like to use this opportunity to give a sincere appreciation to the following:

- My thesis supervisor, Professor Raoul D. Viollier for his continual assistance and guidance in developing the thesis.
- Dr. N. Bilić and Dr. D. Tsiklauri for useful discussions.
- Dr. R. Lindebaum for discussions and technical assistance with computers.
- My wife, C. Dushime for encouragement and patience throughout this investigation.
- The Deutscher Akademischer Austauschdienst (DAAD) for a full scholarship to do this research.
- The University of Cape Town (UCT) for partial financial support, provided by A. M . Mellon Foundation and the UCT Research Associateships programme.

Contents

Chapter 1

Introduction

The evidence for the existence of large amounts of of unseen "dark matter" in the universe, especially in halos around luminous galaxies and in groups and rich clusters of galaxies, has been known for a long time [1, 2]. The presence of the dark matter is inferred from the observed flat rotation curves in spiral galaxies, the diffuse emission of x-rays in elliptical galaxies and clusters of galaxies, as well as from cluster dynamics. Primordial nucleosynthesis entails that most of baryonic matter in this universe is nonluminous, and such an amount of dark matter falls suspiciously close to that required by galactic rotation curves. However, although a significant component of dark matter in galactic halos is presumably baryonic [3], the bulk part of dark matter in this universe is believed to be nonbaryonic.

The problem of dark matter (DM) started already with the pioneering works of Oort [4] in 1932 and Zwicky [5] in 1933. Actually, there are several dark matter problems on different scales ranging from the solar neighbourhood, galactic halos, cluster of galaxies to cosmological scales. Many candidates have been proposed [6], both baryonic as well as nonbaryonic, to explain the dark matter paradigm, but the issue of the nature of dark matter [7] is still not settled.

There are some alternatives to the existence of DM. These are based on the idea that Newtonian dynamics ceases to be valid at smaller accelerations [8] or large scales [9, 10, 11, 12]. This approach is known as Modified Newtonian Dynamics (MOND) [13]. In the framework of MOND, some observational facts related to DM in the dwarf and spiral galaxies and galaxy clusters were successfully reproduced without invoking the existence of dark matter [13, 14]. However, as the latter approach has no viable relativistic generalisation [15], it cannot be applied on cosmological scales. For completeness, we also mention a covariant alternative to general relativity, a conformally invariant fourth-order theory [16], which in the non relativistic regime leads to a linear gravitational potential in addition to the Newtonian $1/r$ term. This theory can explain some of the galactic and cluster dynamics

DM problems. But at the same time, any modification of general relativity is not accepted without debate [17].

There are essentially only two main lines of research in this field. The first focuses on the search for baryonic DM hidden in the form of nonluminous objects, such as brown dwarfs, through the gravitational microlensing events, while the second deals with the detection of DM of nonbaryonic origin, such as massive neutrinos, supersymmetric particles, axions, etc., which could serve as dark matter candidates.

One of the most natural particle candidates for nonbaryonic DM are, of course, massive neutrinos. Non-zero neutrino masses, would thus be an indication of physics beyond the Standard Model of particle physics. Since there exists a number of indications that the Standard Model cannot be the final theory, it would not be a big surprise if neutrinos were massive. As the direct experimental limits on neutrino masses show [18]

$$m_{\nu_e} < 15 \text{ eV}, \quad m_{\nu_\mu} < 0.17 \text{ MeV}, \quad m_{\nu_\tau} < 18.2 \text{ MeV},$$

the neutrino masses have to be much smaller than the corresponding quark and charged lepton masses. An intriguing explanation of this fact could be given by the so-called see-saw mechanism [19, 20] where a right-handed Majorana mass M, at a large scale, i.e. $M_{GUT} \sim 10^{15\pm2}$ GeV modifies through mixing the usual Dirac-type mass m_D of the lightest state $m_D^2/M \ll m_D$. In the simplest versions of this scheme, the neutrino masses would scale as the square of the corresponding charged lepton masses. There are variants (e.g. in models of loop-induced neutrino masses) where neutrino masses are instead linearly related to the charged lepton masses.

Indeed, there are several indications that neutrinos are not massless. Although none of the direct kinematical measurements of neutrino masses has given a value inconsistent with zero, evidence from neutrino oscillations experiments is mounting that neutrinos oscillate in flavour and hence must posses non-zero masses [21]. To give a cosmologically interesting contribution to Ω, the neutrino mass should be in a relatively narrow range $m_\nu c^2 \sim 1 - 50$ eV. A neutrino heavier than that would overclose the universe (unless $m_\nu c^2 > 4$ GeV), which for Dirac neutrinos is ruled out by accelerator and direct detection data up to the TeV range, whereas a lighter neutrino would only give a small and dynamically not important contribution to Ω.

In this thesis, we will focus on nonbaryonic DM consisting of weakly interacting heavy fermions. We are particularly interested in fermions of masses between 10 and 25 keV/c^2 which cosmologically fall into the category of cold dark matter. Fermions of such masses, interpreted in the following as heavy neutrinos, are important as they could form supermassive degenerate neutrino balls, that could mimic the properties of compact dark objects with masses ranging from $10^{6.5}$ $M_\odot$ to $10^{9.5}$ $M_\odot$ usually taken to be black holes. These have been reported to exist at the center of a number of galaxies

[22, 23, 24, 25] including our own [26, 27, 28, 29, 30, 31, 32] and quasistellar objects. It is interesting to note that neutrinos in this mass range can also cluster around ordinary stars, and thus these neutrinos could account for at least part of galactic dark matter. A further motivation for studying the collapsed structures of heavy neutrino matter is the recent increased interest in fermionic cold dark matter models [33] in which massive neutrinos play an important role in structure formation in the early universe.

Let us assume that the LSND experiment is correct and its parameters $\delta m^2_{\mu e} = m^2_{\nu_\mu} - m^2_{\nu_e} \approx 1$ eV$^2/c^4$ and $\sin^2 2\Theta_{\mu e} \approx 10^{-2}$ can be interpreted as $m_{\nu_\mu} \approx 1$ eV$/c^2 >> m_{\nu_e}$, in spite of the fact that KARMEN collaboration [31] has not observed $\nu_\mu \rightarrow \nu_e$ oscillations [35] in at least part of the parameter space advocated by LSND. Let us further assume that the original quadratic see-saw mechanism based on the up, charm and top quark masses [19, 20] , i.e. $m_\nu = m_q^2/M$ with $q = u, c, t$. Inserting the experimental quark masses $m_u \approx 5$ MeV$/c^2$, $m_c \approx 1.5$ GeV$/c^2$ and $m_t \approx 180$ GeV$/c^2$, we conclude that the ν_e and ν_τ masses are $m_{\nu_e} \approx 11.1$ μeV$/c^2$ and $m_{\nu_\tau} \approx 14.4$ keV$/c^2$, respectively. Such a heavy neutrino mass is neither in conflict with particle and nuclear physics experiments nor with astrophysical observations [36]. Here , we note that that the see-saw Majorana mass $M \approx 2.25 \times 10^9$GeV is much smaller than the GUT scale $M_{GUT} \approx 10^{16}$ GeV in this scenario. The ν_τ mass lies in the cosmological forbidden region between between 93 h^{-2} eV$/c^2$ and 4 GeV$/c^2$ [37] with $0.5 \lesssim h \lesssim 0.8$. It is well known that such a quasistable neutrino would pose serious problems in cosmology, as it would generate an early matter dominated phase, starting perhaps as early as a couple of weeks after the Big-Bang. As a direct consequence of the existence of such a heavy neutrino, a critical universe would have reached the current microwave background temperature in less than 1 Gyr, i.e., much too early to accommodate the oldest stars in globular clusters, nuclear cosmochronometry, and the Hubble expansion age.

It is well known [38], however, that there are presumably only two ways to bypass these stringent cosmological constraints on the neutrino masses: (i) reheating; (ii) either the decay or annihilation of the neutrinos and antineutrinos. Reheating of the plasma would have to take place between the nucleosynthesis and (re)combination. The temperature can only increase by a factor of 2 or 3 at most during reheating, because otherwise it would, through a baryon to photon ratio which differs from that after three minutes, also reduce the number of baryons below the number that is observed in stars of our universe. Therefore, reheating alone is certainly not sufficient to bypass the cosmological bounds on neutrino mass. If the decay involves photons, it should happen at temperatures that are not too different from the energy of the decay photons, so that they have enough time to thermalize and do not distort the microwave background. Regardless of whether photons are involved in the decay or not, this would obviously involve non-standard par-

ticle physics. Annihilation via the Z^0 can only be effective in gravitationally condensed objects. In fact, it has been shown [33] that a similar scenario, in which the cosmological bounds can be bypassed, exists in supermassive neutrino balls.

It is conceivable, however, that, in the presence of such heavy neutrinos, the evolution of the early universe will differ substantially from that of the Standard Model of Cosmology. Neutrino balls may have emerged in local condensation processes during a gravitational phase transition, after the neutrino-matter dominated epoch began. The latent heat produced in such a first-order phase transition is about 3.6% of the rest mass of the neutrino balls [39]. The latter might have reheated the radiation background apart from reheating the gaseous phase. Soon after the formation of neutrino balls, annihilation of heavy neutrinos into light neutrinos via the Z^0 would take place efficiently in the interior of neutrino balls [36, 40]. Since both these processes would increase the age of the universe, i.e. postpone the time when the universe reaches the current microwave background temperature, a quasistable neutrino in the mass range between 10 and 25 keV/c^2 is presumably not incompatible with cosmological and astrophysical observations [36, 41].

In fact, based on the Thomas-Fermi model at finite temperature, it has been shown [30, 37, 42, 43, 44] that some time during the heavy neutrino matter dominated epoch, the universe will undergo a gravitational phase transition, yielding a condensed phase that consists of degenerate neutrino balls [36, 40, 45, 46, 39]. Most of the matter, if not all, will be in the condensed phase below the critical temperature. Only a fraction of 10^{-3} of the neutrinos are estimated to be in the gaseous phase after this phase transition leading to a neutrino dominated critical universe today. Moreover, the latent heat associated with this first-order phase transition will be released and the plasma will be moderately reheated. Of course, for this phase transition to happen, one would need an efficient dissipation mechanism within or beyond the Standard Model of particle physics, in order to make sure that the neutrinos and antineutrinos can settle in the state of lowest energy in a reasonable period of time.

In this thesis, we focus primarily on gravitationally clustered, degenerate nonbaryonic matter consisting of weakly interactive fermions of mass around 15 keV/c^2 and we would like to study the influence of such a fermionic halo on the motion of planets around the sun [47]. We then consider an astrophysical system made of two types of constituents fermions: one with a mass around 15 keV/c^2 which we subsequently call "neutrino", and the other with a mass around 1 GeV/c^2 which we henceforth call "neutralino". With regards to the neutralino masses, neutralinos are generally assumed to have masses of tens of GeV. A standard $m_{\tilde{\chi}_1^0} > 23$ GeV/c^2 (C.L. = 95%) neutralino or a $m_{\tilde{\gamma}} > 15$ GeV/c^2 (C.L. = 90%) photino which are the experimental and observational limits [48], can be used as examples of neutralino masses in this approach.

However, in most models of low-energy supersymmetry in which dimension-3 supersymmetry breaking operators are highly suppressed [49], photinos and gluinos are very light. In this quite attractive supersymmetry breaking scenario, the lightest R-odd particle may be a color-singlet state containing a gluino, the R^0, with mass m_{R^0} in the 1 to 2 GeV range [50]. Moreover, it has been recently pointed out [51] within this framework, that a photino $\tilde{\gamma}$ slightly lighter than the R^0, in the mass range of 100 MeV to 1.4 GeV, would survive as the relic R-odd species and it might be an attractive dark matter candidate. Indeed, a light photino with a mass in the range $1.2 \leq m_{R^0}/m_{\tilde{\gamma}} \leq 2.2$ is cosmologically acceptable and in the range $1.6 \leq m_{R^0}/m_{\tilde{\gamma}} \leq 2.2$ even an excellent dark matter candidate. Neutralino stars could thus mimic the properties of Massive Compact Halos Objects (MACHOs) [52, 53].

It is important to mention that the chosen neutralino mass offers the possibility to replace the neutralino with a neutron, as the strong-interaction effects of the neutron in neutron star matter can be simulated by an effective mass. Of course, this substitution is only valid as long as the binding energy of the neutron is larger than the Q value for the neutron decay, so that the neutron can be considered stable in neutron star matter. Moreover, similar scenarios can be treated in the same framework: Apart from a neutrino halo around a neutron star, one might study the properties of an astrophysical system consisting of a neutrino halo around a white dwarf or around any ordinary star [45]. All these baryonic stars can be approximated by a polytropic equation of state which eventually result in the same nonlinear differential equations of Lané-Emden type. Thus the study of this simple interacting neutrino-neutralino system allows us to learn a great deal about the properties of gravitationally clustered baryonic and nonbaryonic matter.

Neutrino balls are described in this thesis as alternatives to the supermassive black holes at the Galactic centers. There are two general lines of argument that are used to "prove" the existence of black holes in Galactic nuclei. The first attempts to measure the total mass within a volume, and argues that no other form besides a black hole can have these parameters. This is done either via estimation of the volume from variability data (via the light travel argument) and mass from luminosity (via the Eddington mass limit). Alternatively, this can be determined by a measurement of velocity of matter at a specified distance from the central object, essentially using Kepler's laws. Despite the vast and tantalizing work undertaken to resolve the issue of the existence of supermassive black holes (BHs) at the centers of galaxies, it seems fair to say that, in this case, the jury is still out (for a current status see ref. [54] for a review). The discovery of quasars in the early 1960's quickly spurred the idea that these amazing powerful sources derive their energy from accretion of matter onto compact, supermassive objects of 10^6 to 10^9 solar masses. This has led many to believe that these objects are supermassive black holes [55, 56, 57]. Since then this model has provided a

highly useful framework for the study of quasars, or more generally, of the active galactic nucleus (AGN) phenomenon [58]. Yet, despite its success, there is little empirical basis for believing that this model is correct. As it has also been pointed out [59, 60], the current belief of the scientific community that the driving engines of active galactic nuclei are actually supermassive black holes largely rests on the implausibility of alternative explanations, in particular, explanations which are based on some form of clustered *baryonic* matter. Thus, as there is no compelling evidence that the supermassive BHs exist at the galactic centers, alternative scenarios ought to be developed.

A very compact dark stellar cluster [61, 62] has been suggested as an alternative to the black hole scenario. However, such dark clusters models are highly improbable [60, 63] due to stability criteria. A viable cluster must have both evaporation and collision time scales greater than the life time of the Galaxy $\sim$ 10 Gyr. This is more likely to be fulfilled with a cluster of substellar objects. But, apart from a cluster of a very low-mass black holes that is free of stability problems, the most attractive alternative to a dense stellar cluster is a cluster of elementary weakly interacting particles.

In fact, an alternative model for the supermassive compact dark objects at the Galactic centers has recently been developed [30, 31, 32, 36, 45, 46, 39, 64, 65]. It has been shown [31] that the dark matter concentration observed through stellar motion at the Galactic center [66, 67, 68] is consistent with a supermassive object of 2.5×10^6 solar masses made of self-gravitating, degenerate heavy neutrino matter. A neutrino ball at the Oppenheimer-Volkoff limit [39] which corresponds to a neutrino mass of few hundreds keV/c^2, is almost indistinguishable from a black hole of the same mass. However, these two scenarios differ substantially for neutrino masses between 10 and 25 keV/c^2. In fact, the observational data [28, 66, 67] on the supermassive dark object at the Galactic center restrict the neutrino mass to $m_\nu \geq 13.4$ keV/c^2 for $g_\nu = 4$ or $m_\nu \geq 15.9$ keV/c^2 for $g_\nu = 2$, where g_ν is the spin degeneracy factor of the neutrinos and antineutrinos. Using these lower bounds, the emitted spectrum by Sgr A* was calculated in the framework of standard accretion disk theory [32, 69] and it has been shown that the neutrino ball model explains a part of the radio wave and infrared emission of the observed spectrum if the neutrino mass and the accretion rate fulfil some constraints.

The most reliable technique to find the mass distribution at the Galactic center is based on the statistical analysis of the dynamics of stars. This is due to the fact that stars are direct tracers of the gravitational potential and are not affected by non-gravitational forces, in contrast to gas clouds, for example, which may be vastly affected by existing magnetic fields. Standard techniques based on the Jeans equation [31, 70] to determine the mass of the central object are not efficient as the results obtained in this approach are quite sensitive to the effects of velocity anisotropy [59]. While at projected distances from Sgr A* larger than 0.1 pc the number of stars observed

within a shell of a given projected thickness is large enough to make the calculation of the velocity dispersion statistically sound. this number drops only to 15 stars within 1 arcsec^2 [28], rendering a statistical treatment of the innermost stars around Sgr A* somewhat meaningless. Thus, in this thesis we would like to explore the gravitational potential of Sgr A* without using statistics, i.e. studying the motion of individual stars [71, 72]. in particular, in the immediate vicinity of the Galactic center. where statistical arguments cannot be easily applied due to the low density of stars. Such analysis has the advantage of being model *independent* as it will be solely based on the Newtonian dynamics.

This thesis is organized as follows: In chapter 2, we derive the equations that govern the structure of neutrino balls in the framework of Newtonian theory and also study the effect of such neutrino halos on the planetary and asteroidal orbits around the sun. In chapter 3, we investigate the relativistic effects on degenerate neutrino balls and generalize the Tolman-Oppenheimer Volkoff equations to include gravitationally clustered, degenerate nonbaryonic matter around compact stars such as neutralino (neutron) stars and white dwarfs. In chapter 4, we show that the supermassive compact dark object at the Galactic center could be an extended object rather than a supermassive black hole. This is achieved by considering the motion of the fastest star S1 or (S0-1) in the black hole or neutrino ball scenarios of Sgr A*. We then calculate the emission spectrum of the compact dark object at the Galactic center using the standard thin accretion disk theory and compare our predictions with the most recent observations. Our results are summarized in Chapter 5.

Chapter 2

Non-relativistic neutrino balls

2.1 The model

In this chapter, we study the properties of a non-relativistic gas made of heavy neutrinos and antineutrinos. We assume that neutrinos interact only gravitationally and neglect finite temperature effects and exchange effects a la Thomas-Fermi-Dirac. Let us denote the gravitational potential of neutrinos and antineutrinos by $\Phi(r)$, the pressure of the neutrino fluid by $P_\nu(r)$ and the density by $\rho_\nu(r)$. In non-relativistic approximation, those three quantities are linked by the equations

$$\Delta\Phi = 4\pi G\rho_\nu, \tag{2.1}$$

$$\frac{dP_\nu}{dr} = -\rho_\nu \frac{d\Phi(r)}{dr}, \tag{2.2}$$

where G is Newton's gravitational constant. In the case of spherical symmetry, the first equation can be rewritten as a system of the two differential equations

$$\frac{d\Phi}{dr} = \frac{Gm(r)}{r^2}. \tag{2.3}$$

$$\frac{dm}{dr} = 4\pi r^2 \rho_\nu, \tag{2.4}$$

where $m(r)$ is the mass of neutrinos and antineutrinos enclosed within a radius r. Equation (2.1) is the Poisson's equation while equation (2.2) constitutes the condition of hydrostatic equilibrium between the pressure and the gravitational field of neutrinos and antineutrinos. We will denote the neutrino mass by m_ν and the neutrino number density by n_ν. The mass density of neutrinos and antineutrinos ρ_ν can be written as

$$\rho_\nu = m_\nu n_\nu. \tag{2.5}$$

In order to solve the equations (2.1) and (2.2), one needs the equation of state in the form

$$P_\nu = P_\nu(\rho_\nu). \tag{2.6}$$

The choice of the equation of state (2.6) depends on the model of the neutrino gas. As neutrinos obey the Fermi-Dirac statistics, we will choose the equation of state to be that of a non-relativistic Fermi gas at zero temperature, i.e., a cold Fermi gas

$$P_\nu = K\rho_\nu^{5/3} , \tag{2.7}$$

where P_ν is the degeneracy pressure and K is a constant given by

$$K = \left(\frac{6}{g_\nu}\right)^{2/3} \frac{\pi^{4/3}\hbar^2}{5m_\nu^{8/3}} , \tag{2.8}$$

and g_ν is the spin degeneracy factor of neutrinos and antineutrinos, i.e. $g_\nu = 2$ for Majorana neutrinos and $g_\nu = 4$ for Dirac neutrinos and antineutrinos. We will assume that the pressure and density vanish at a certain radius R_0 of the neutrino ball, i.e.

$$\rho_\nu(R_0) = P_\nu(R_0) = 0 . \tag{2.9}$$

Outside the neutrino ball, the mass density vanish and we recover the standard solution of the Poisson's equation (2.1)

$$\Phi(r) = -\frac{GM}{r} , \tag{2.10}$$

where M is the mass of the neutrino ball, i.e.

$$M = \int_0^{R_0} 4\pi\rho_\nu r^2 dr. \tag{2.11}$$

2.2 Derivation of Lané-Emden equation

By using the equation of state (2.7), one can integrate the equation (2.2) of hydrostatic equilibrium to find the relation between the density of neutrinos $\rho_\nu(r)$ and their gravitational potential $\Phi(r)$

$$\rho_\nu(r) = \left(\frac{2}{5K}(\Phi_0 - \Phi(r))\right)^{3/2} , \tag{2.12}$$

where the arbitrary constant Φ_0 has been chosen such that the gravitational potential $\Phi_0 - \Phi(r)$ is zero for vanishing neutrino density. We substitute the neutrino density (2.12) into the Poisson's equation (2.1) and restricting ourselves to spherical symmetry, we get

$$\frac{1}{r^2}\frac{d}{dr}\left(r^2\frac{d\Phi}{dr}\right) = 1\pi G\frac{2^{1/2}g_\nu m_\nu^4}{3\pi^2\hbar^3}\left(\Phi_0 - \Phi(r)\right)^{3/2} . \tag{2.13}$$

Next, we introduce a new potential $u(r)$ and a point like baryonic star of mass M_B defined as

$$u = r(\Phi_0 - \Phi(r)) , \tag{2.14}$$

and

$$\lim_{r\to 0} r\left(\Phi_0 - \Phi(r)\right) = GM_B\ . \tag{2.15}$$

By substituting (2.14) into equation (2.13) we arrive at the non-linear Lané-Emden differential equation with polytrope index 3/2 [73, 74]

$$\frac{d^2u}{dr^2} = -\frac{4\sqrt{2}m_\nu^4 G g_\nu}{3\pi\hbar^3}\frac{u^{3/2}}{\sqrt{r}}. \tag{2.16}$$

The boundary conditions relevant to our problem are obviously

$$u(0) = GM_B,\ u(R_0) = 0\ , \tag{2.17}$$

where R_0 is the radius to which the neutrino halo extends, and M_B is the mass of the point like baryonic star around which the neutrino halo is clustered. Introducing, the dimensionless variables

$$x = r/a_\nu,\ v(x) = u(r)/GM_\odot, \tag{2.18}$$

with

$$a_\nu = \left(\frac{3\pi\hbar^3}{4\sqrt{2}m_\nu^4 g_\nu G^{3/2}M_\odot^{1/2}}\right)^{2/3} = 2.1376\ \text{lyr}\left(\frac{17.2\ \text{keV}}{m_\nu c^2}\right)^{8/3} g_\nu^{-2/3}, \tag{2.19}$$

where $M_\odot$ is the solar mass, we arrive at

$$\frac{d^2v}{dx^2} = -\frac{v^{3/2}}{\sqrt{x}}, \tag{2.20}$$

with the boundary conditions on the normalized potential v

$$v(0) = \frac{M_B}{M_\odot},\ v(x_0) = 0. \tag{2.21}$$

The equation (2.20) is the the Lané-Emden equation for the normalized potential v and it plays a central role in this thesis.

All physical quantities such as the gravitational potential $\Phi(r)$, the mass density ρ_ν and the neutrino degeneracy pressure P_ν can be expressed in terms of the new potential $v(x)$ and dimensionless variable x as follows

$$\Phi(r) = \Phi_0 - \frac{GM_\odot v}{a_\nu x}\ , \tag{2.22}$$

$$\rho_\nu(r) = \frac{2^{1/2}}{3}\frac{m_\nu^4 g_\nu}{\pi^2\hbar^3}\left(\frac{GM_\odot}{a_\nu}\right)^{3/2}\left(\frac{v}{x}\right)^{3/2} = \rho_0\left(\frac{v}{x}\right)^{3/2}, \tag{2.23}$$

where the constant ρ_0 is given by

$$\begin{aligned}\rho_0 &= \frac{8m_\nu^8 g_\nu^2 G^3 M_\odot^2}{9\pi^3\hbar^6} \\ &= 1.9112\times10^{-23}\mathrm{g/cm^3}\times\left(\frac{m_\nu c^2}{17.2\ \mathrm{keV}}\right)^8 g_\nu^2 \\ &= 2.8228\times10^{-1}\mathrm{M_\odot/pc^3}\left(\frac{m_\nu c^2}{17.2\ \mathrm{keV}}\right)^8 g_\nu^2,\end{aligned} \tag{2.24}$$

and

$$P_\nu(r) = \left(\frac{6}{g_\nu}\right)^{2/3}\frac{\pi^{4/3}\hbar^2}{5m_\nu^{8/3}}\rho_\nu^{5/3}. \tag{2.25}$$

2.3 Lané-Emden and Thomas-Fermi equations

Let us study an electron gas in an atom around a nucleus of charge Z. In such a gas the electrons are distributed among the various quantum states so that the total energy of the gas has its least possible value. Since no more than one electron can be in the same quantum state, the electrons occupy all states with energies from the smallest value to some largest value, i.e., Fermi energy, which of course depends on the number densities of electrons in the gas. The atomic number Z should be greater or equal to the number of electrons N (atom or an ion). The degeneracy pressure of electrons can be therefore written in the following form

$$P_e = \frac{\hbar^2}{5m_e}\left(\frac{6\pi^2}{g_e}\right)^{2/3} n_e^{5/3}, \tag{2.26}$$

where m_e stands for the electron mass, $g_e = 2$ its spin degeneracy factor and n_e is the electron number density. If we approximate the nucleus as a point source, we can use the Poisson's equation (2.1) which is valid everywhere except at the origin, with the electron number density in the right side instead of the mass density, i.e.

$$\Delta\Phi(r) = 4\pi e n_e(r). \tag{2.27}$$

The equation of hydrostatic equilibrium (2.2) can be integrated and in result

$$n_e(r) = \frac{g_e}{6\pi^2\hbar^3}\left[2m_e e(\Phi(r)-\Phi_0)\right]^{3/2}. \tag{2.28}$$

Inserting the expression for the number density in the right side of the Poisson's equation and assuming spherical symmetry, we arrive at the equation

$$\frac{d^2\Phi(r)}{dr^2} + \frac{2}{r}\frac{d\Phi}{dr} = \frac{4\pi e g_e}{6\pi^2\hbar^3}\left[2em_e(\Phi(r)-\Phi_0)\right]^{3/2}. \tag{2.29}$$

Introducing new potential $u(r)$ as in the last section defined by $u(r) = r(\Phi(r) - \Phi_0)$, one finds the Thomas-Fermi equation [75, 76] for an electron gas around a point like nucleus,

$$\frac{d^2u(r)}{dr^2} = \frac{2\epsilon g_e}{3\pi\hbar^3}(2em_e)^{3/2}\frac{u^{3/2}}{\sqrt{r}}. \tag{2.30}$$

The electron number density and degeneracy pressure can be written in terms of the potential $u(r)$ as

$$n_e(r) = \frac{g_e}{6\pi^2\hbar^3}(m_e e)^{3/2}\left(\frac{2u(r)}{r}\right)^{3/2}, \tag{2.31}$$

$$P_e(r) = \frac{(m_e e)^{5/2}}{5m_e\hbar^3}\frac{g_e}{6\pi^2}\left(\frac{2u(r)}{r}\right)^{5/2}. \tag{2.32}$$

In order to specify the solution of the equation (2.30), we need boundary conditions. The first boundary is due to the fact that at the classical turning point r_0 the electron number vanishes. The second boundary is that, as r tends to zero, the potential should become Coulomb like. Our boundary conditions are therefore

$$u(r_0) = 0 \text{ and } u(0) = Ze\ . \tag{2.33}$$

We can define dimensionless variables defined as $x = r/a_e$ and $v = u/\epsilon$ yielding the Thomas-Fermi equation for an ion

$$\frac{d^2v}{dx^2} = \frac{v^{3/2}}{x^{1/2}}\ . \tag{2.34}$$

with the boundary conditions

$$v(0) = Z \text{ and } v(x_0) = 0 \text{ for } x_0 = r_0/a_e\ . \tag{2.35}$$

The scale parameter a_e which plays the role of length unit is given by

$$a_e = a_0\left(\frac{3\pi^2}{32g_e^2}\right)^{1/3} = 0.71370\text{Å}\left(\frac{0.511\ \text{MeV}}{m_e c^2}\right)g_e^{-2/3}, \tag{2.36}$$

where $a_0 = \hbar^2/(m_e c^2)$ is the Bohr's radius in an atom. Let us point out that the characteristic scale of length a_e is of the order of the Bohr's radius in the case of an electron cloud around an atomic nucleus while for a neutrino halo around a baryonic star, the similar scale a_ν is of the order of a few light years. This seems to be a non-trivial coincidence, as the scale a_ν depends strongly on the value of the neutrino mass m_ν ($\sim m_\nu^{-8/3}$), while it is rather insensitive to the value of the solar mass $M_\odot$. We note that the Thomas-Fermi equation (2.34) for an electron cloud around the nucleus is similar

to the Lané-Emden differential equation (2.20) for neutrino halos around a baryonic star, except for the minus sign that is due to the gravitational attraction of the neutrinos, as opposed to the electrostatic repulsion between the electrons. The solutions of the Thomas-Fermi equation are concave while the ones corresponding to the Lané-Emden equation are convex as we will see below. An other difference between those two equations is that Lané-Emden equation for neutrinos halos admit a solution without a baryonic mass at the center, i.e. $M_B = 0$ while the Thomas-Fermi has no solution for $Z = 0$. The solution of Lané-Emden equation with $M_B = 0$ will be referred to as a pure neutrino ball.

2.4 Homology theorem

Both the Lané-Emden and Thomas-Fermi equations admit an homology group of transformations. Indeed, if $v(x)$ is a solution of the equation

$$\frac{d^2v}{dx^2} = \pm\frac{v^{3/2}}{\sqrt{x}}, \tag{2.37}$$

then

$$\tilde{v} = A^3 v(Ax), \tag{2.38}$$

is also a solution of the same equation (2.37), where A is any positive real number.

Proof:

From the fact that

$$\tilde{v} = A^3 v(Ax), \tag{2.39}$$

the second derivative with respect to x reads

$$\tilde{v}'' = A^5 v''(Ax). \tag{2.40}$$

Hence

$$\frac{\tilde{v}^{3/2}}{\sqrt{x}} = \frac{A^{9/2}[v(Ax)]^{3/2}}{\sqrt{Ax}}\sqrt{A} = \frac{A^5[v(Ax)]^{3/2}}{\sqrt{Ax}}, \tag{2.41}$$

and therefore it follows that

$$\tilde{v}''(x) \pm \frac{\tilde{v}^{3/2}(x)}{\sqrt{x}} = A^5\left(v''(Ax) \pm \frac{[v(Ax)]^{3/2}}{\sqrt{Ax}}\right). \tag{2.42}$$

The right side of the last equation is zero due the the assumption (2.37) and thus

$$\tilde{v}''(x) \pm \frac{\tilde{v}^{3/2}(x)}{\sqrt{x}} = 0\,. \tag{2.43}$$

As consequence of the homology group of transformations, if $v(x)$ extends from 0 to $x = x_0$ then $\tilde{v}$ will extend from 0 to x_0/A. The masses and the radius of the halo and baryonic star will thus scale as

$$\begin{aligned} \tilde{M}_\nu &= M_\odot \int_0^{x_0} [A^3 v(Ax)]^{3/2} x^{1/2} dx \\ &= A^3 M_\odot \int_0^{x_0} [v(x)]^{3/2} x^{1/2} dx = A^3 M_\nu \ , \end{aligned} \tag{2.44}$$

$$\tilde{M}_B = M_\odot \tilde{v}(0) = A^3 M_\odot v(0) = A^3 M_B \ , \tag{2.45}$$

with

$$\tilde{R}_0 = R_0/A \ , \tag{2.46}$$

and in result the products $M_\nu R_0^3$, $M_B R_0^3$ and M_B/M_ν are independent of the scaling parameter A. The same scaling property holds for the Thomas-Fermi equation. In this case NR_0^3, ZR_0^3 and Z/N will all be independent of A.

Let us find the total mass M of the neutrino halo around a baryonic star of mass M_B. Using the Eq. (2.11) and the expression for the neutrino density in terms of v, M can be written as

$$M = M_\odot \int_0^{x_0} v^{3/2}(x) x^{1/2} dx \ . \tag{2.47}$$

Next we use the Lané-Emden equation for v to express the integrand as

$$M = -M_\odot \int_0^{x_0} \frac{d^2 v}{dx^2} x dx. \tag{2.48}$$

Integrating by parts and using the boundary conditions (2.21), we obtain for the total mass M

$$M = M_B + M_\nu = -x_0 v'(x_0) M_\odot, \tag{2.49}$$

where M_ν is the mass of neutrinos and antineutrinos around a baryonic star of mass M_B. An analogous expression can be obtained in the case of Thomas-Fermi equation and reads

$$Z - N = -x_0 v'(x_0) \ , \tag{2.50}$$

where N is the number of electrons and Z is the atomic number. The scaling property can be used to construct a solution of Lané-Emden equation with any desired mass $\tilde{M}$ of the halo. From the relation $MR^3 = \text{const}$, it is clear that by dividing the radius by a constant A and multiplying the same expression by A^3 we still get the same constant, i.e. $MA^3(\frac{R}{A})^3 = MR^3$. If we want to get a neutrino halo of mass $\tilde{M}$ from a solution with mass $2.71406 M_\odot$, we therefore choose the constant A to be $\left(\tilde{M}/(2.71406 M_\odot)\right)^{1/3}$. The radius of such object is $3.65375\ a_\nu/A$ which obviously depends on the neutrino mass.

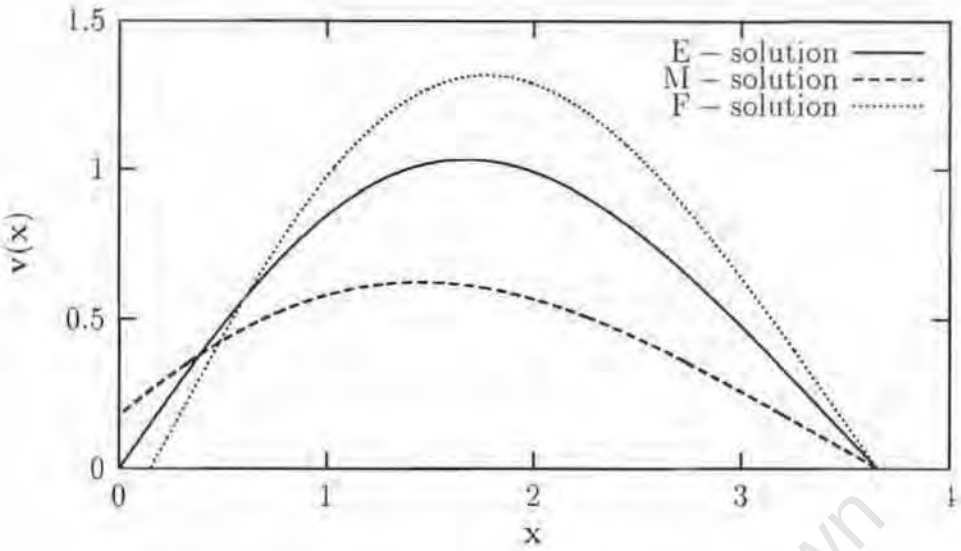

Figure 2.1: Typical Solutions of Lané-Emden differential equation: pure neutrino ball (F-solution), and neutrino halo around a pointlike baryonic star (M-solutions). The F-solutions are unphysical.

2.5 Pure neutrino balls

2.5.1 Gravitational potential of a pure neutrino ball

For a pure neutrino ball, i.e., a halo without a baryonic star at the centre, we have $M_B = 0$ and thus $v(0) = 0$. By choosing $v'(0) = 1$ and solving the differential equation (2.20), we obtain the E- type solution [36] shown as the solid curve in Fig. 2.1. The radius of the halo will occur at $x_0 = 3.65375$ and the slope at this position will be given by $-x_0 v'(x_0) = 2.71406$. The total mass of this solution is

$$M_\nu = -x_0 v'(x_0) M_\odot = 2.71406\ M_\odot, \tag{2.51}$$

and its radius is 3.65375 a_ν where a_ν is the length scale as given by Eq. (2.19). We can integrate the equation (2.20), starting from the point x_0 and varying the slope at x_0. If $-x_0 v'(x_0) < 2.71406$, we arrive at $v(0) > 0$, an M-type solution [36], which corresponds to $M_B > 0$ (dashed line). For $-x_0 v'(x_0) > 2.71406$, $v(x)$ will have at least one zero in the interval $0 < x < x_0$, which obviously represents a gravitational unstable and thus unphysical solution [36] that must be discarded. We thus see that Lané-Emden equation admits two types of physical solutions: one without a baryonic star at the center (pure neutrino ball) and the other with baryonic mass at the center of the neutrino halo.

Let us now turn to the study of the gravitational potential of a pure

neutrino ball. Using the Eq. (2.22), the gravitational potential of a pure neutrino ball can be written as

$$\Phi(r) = \begin{cases} \Phi_0 - \dfrac{GM_\odot v(x)}{a_\nu x} & r \leq R_0 \\ \dfrac{-GM_\nu}{r} & r > R_0 \ , \end{cases} \tag{2.52}$$

where M_ν is the the total mass of the neutrino ball. In this case $M_\nu = -x_0 v'(x_0)$. By requiring the continuity of the potential and its derivative at the boundary of the neutrino ball, the constant of integration Φ_0 can be found to be $\Phi_0 = GM_\odot v'(x_0)/a_\nu$ and we get for the gravitational potential

$$\Phi(r) = \frac{GM_\odot}{a_\nu} \begin{cases} v'(x_0) - \dfrac{v}{x} & x \leq x_0 \\ \dfrac{x_0 v'(x_0)}{x} & x > x_0 \ . \end{cases} \tag{2.53}$$

Let us recall that x_0 is the boundary of the neutrino ball in dimensionless variables, i.e. $x_0 = R_0/a_\nu$. By solving the Lané-Emden equation for a pure neutrino ball, we can thus plot its gravitational potential as a function of the radius as shown in Fig. 2.2. In the same figure the gravitational potential of a black hole and that due to a constant density object of the same mass as the neutrino ball are shown for comparison.

Near the center of the neutrino ball, the gravitational potential has an harmonic oscillator type which reveals that the density distribution near the center is almost constant as it can be shown from Fig. 2.3. This can be seen by writing the expansion of Emden function with index 3/2 (see Appendix A) near the origin

$$v(x) = x - \frac{1}{3!}x^3 + \frac{3/2}{5!}x^5 - \frac{8 \times (3/2)^2 - 5 \times 3/2}{3.7!}x^7 + \cdots \ . \tag{2.54}$$

With the use of equation (2.53), the gravitational potential becomes

$$\Phi(r) = \frac{GM_\odot}{a_\nu}(v'(x_0) - 1 + \frac{1}{3!}x^2 + \cdots), \tag{2.55}$$

which is approximately a harmonic oscillator potential.

2.5.2 The mass limit of neutrino balls

We have seen in the previous sections that the radius and the mass of a pure neutrino ball obey the relation

$$M R_0^3 = \text{const} \ . \tag{2.56}$$

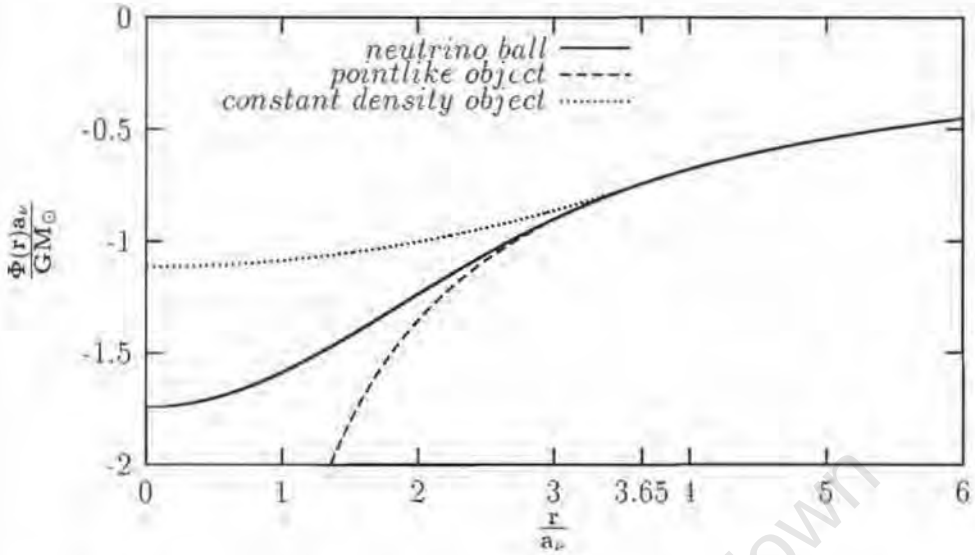

Figure 2.2: The gravitational potential $\Phi(r)$ of a pure neutrino ball of mass 2.71406 $M_\odot$ as a function of the radius r. The gravitational potentials of a black hole as well as of a constant density object of the same mass as the neutrino ball are shown on the graph for comparison.

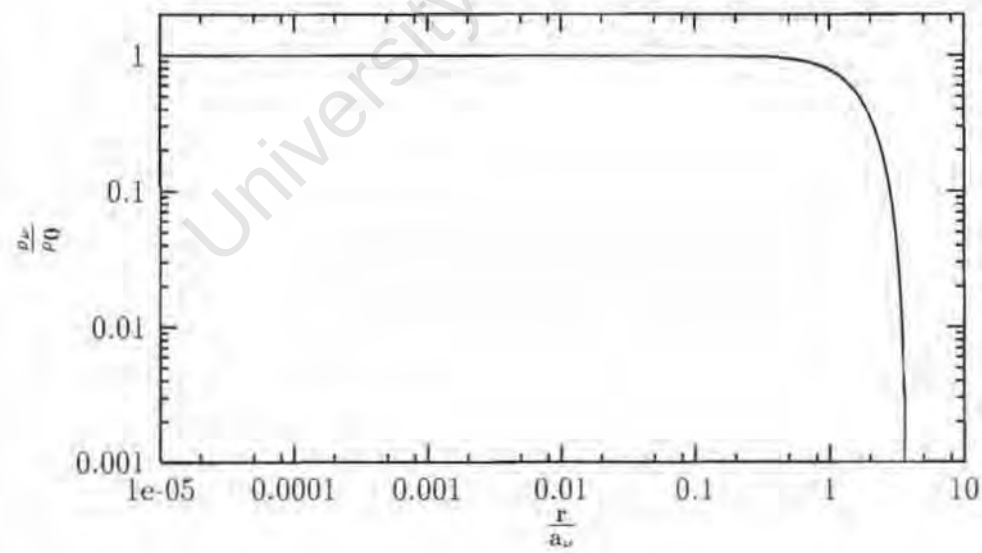

Figure 2.3: The density ρ_ν of a pure neutrino ball as a function of the radius r. Near the center, the density of neutrinos is almost constant. At the radius of the neutrino ball, its density ρ_ν vanishes.

Using the the solution of Lané-Emden equation with mass $M = 2.71406\ M_\odot$ and a radius $R_0 = 3.65375\ a_\nu$, one can compute the value of the constant in the last equation, and we obtain the mass-radius relationship

$$\begin{aligned} M_\nu R_0^3 &= \frac{91.869\hbar^6}{G^3 m_\nu^8}\left(\frac{2}{g_\nu}\right)^2 \\ &= 6.3003\times 10^{10} M_\odot \mathrm{ld}^3 \left(\frac{17.2\ \mathrm{keV}}{m_\nu c^2}\right)^8 g_\nu^{-2}. \end{aligned} \tag{2.57}$$

The neutrino ball will exist as long as its radius R_0 is greater than the corresponding Schwarzschild radius, otherwise it will be a black hole. The Schwarzschild radius R_s corresponding to a mass M_ν is given by

$$R_s = \frac{2GM_\nu}{c^2}\ . \tag{2.58}$$

One can find the mass M_ν for which the neutrino ball becomes a black hole. This is done by substituting the expression for R_s in the place of R_0 and solving for M_ν from the equation (2.57). Let us denote the obtained M_ν by M_{BH} the black hole mass limit for neutrino balls.

$$\begin{aligned} M_{\mathrm{BH}} &= 2.6034\frac{M_{\mathrm{Pl}}^3}{m_\nu^2 g_\nu^{1/2}} \\ &= 1.4375\times 10^{10} M_\odot \times \left(\frac{17.2\ \mathrm{keV}}{m_\nu c^2}\right)^2 g_\nu^{-1/2}\ , \end{aligned} \tag{2.59}$$

where $M_{\mathrm{Pl}} = (\frac{\hbar c}{G})^{1/2}$ is the Planck's mass. Using the last expression, the Schwarzschild radius R_s is

$$\begin{aligned} R_s &= 1.6388 \times \left(\frac{17.2\ \mathrm{keV}}{m_\nu c^2}\right)^2 g_\nu^{-1/2}\ \mathrm{ld} \\ &= 4.2452\times 10^{10} \times \left(\frac{17.2\ \mathrm{keV}}{m_\nu c^2}\right)^2 g_\nu^{-1/2}\ \mathrm{km}\ . \end{aligned} \tag{2.60}$$

Of course, general relativity corrections will reduce this mass limit by a factor of ~ 4.8 (see chapter 3) while the inclusion of the rotation of the neutrino ball will increase it. There might be other small corrections due to exchange and finite temperature effects, as well as baryonic impurities. For neutrino balls consisting of of 10 to 25 keV/c^2 neutrinos, the mass limit M_{BH} can go up to few times $10^9\ M_\odot$, which is about the upper limit for the masses of the purported black holes at the centres of galaxies.

2.5.3 The mass distribution at the Galactic center

From the analysis of an extensive set of near-IR radial velocities of individual stars around the Galactic center, Genzel et al. [67, 77] found a a highly

statistically significant rise in the radial velocity dispersion between 5 and 0.1 pc from the dynamical center. Assuming an isotropic velocity dispersion, the observations require a dark mass of $\sim 3 \times 10^6 M_\odot$ within $r = 0.1$ pc and a mass to light ratio M/L greater than 100, the dark mass must have a density in excess of $10^9 M_\odot \mathrm{pc}^{-3}$, which could be a supermassive black hole (SMBH). These conclusions and a suspicion nearly three decades old [78], have finally been vindicated by recent measurements of stellar proper motions within the central 1 pc region using high -resolution K-band astrometric maps [27, 66, 68, 28]. The main results are as follows:(1) the stellar radial velocities agree with the proper motion of stars, which implies that that on average the velocities are close to isotropic; (2) the combined velocities imply a dark mass within 0.016 pc of $2.61 \times 10^6 M_\odot$; (3) the density, therefore, has an astonishing high value of $\gtrsim 2 \times 10^{12} M_\odot \mathrm{pc}^{-3}$, which leaves almost no room to escape the conclusion that the dark mass must be in the form of a SMBH. The presence of a large mass is also supported by by the detection of several stars, within 0.01 pc from the central radio source Sgr A*, moving at speeds in excess of 1000 km/s. The recent observations of the dynamics of stars around the Galactic center imply that there is a supermassive dark object of mass $(2.6 \pm 0.2) \times 10^6 M_\odot$ concentrated within a radius of 0.015 pc. However, the radius of this object is still 40000 times larger than the Schwarzschild radius corresponding to a mass of $2.6 \times 10^6 M_\odot$ and therefore the black hole scenario of Sgr A* is not necessarily the only solution. Here, we explore an alternative scenario for Sgr A*, in which we assume that self-gravitating, degenerate heavy neutrino matter can form a long-lived configuration of mass of $2.6 \times 10^6 M_\odot$ and a radius of a few tens of light days [31, 71]. By assuming the supermassive dark object at the center of our galaxy to be a neutrino ball, the maximal size of this object yields a lower limit on the neutrino mass. A neutrino ball of $2.6 \times 10^6 M_\odot$ composed of neutrinos with masses

$$\begin{aligned} m_\nu c^2 &\geq 15.9 \text{ keV for } g_\nu = 2, \\ m_\nu c^2 &\geq 13.4 \text{ keV for } g_\nu = 4, \end{aligned} \tag{2.61}$$

is consistent with the recent observational data [28] as shown in Fig. 2.1 where we present the mass enclosed in a neutrino ball of mass $M = 2.6 \times 10^6 M_\odot$ for various values of the neutrino mass.

2.6 Neutrino halo around the sun

2.6.1 Heavy neutrino dark matter in the solar system

In this section, we will consider the second type of the physical solution [47]. For this purpose, we solve the Lané-Emden equation (2.20) with M_B different from zero. Let us study the halo of neutrino around the sun, i.e. $M_B = M_\odot$.

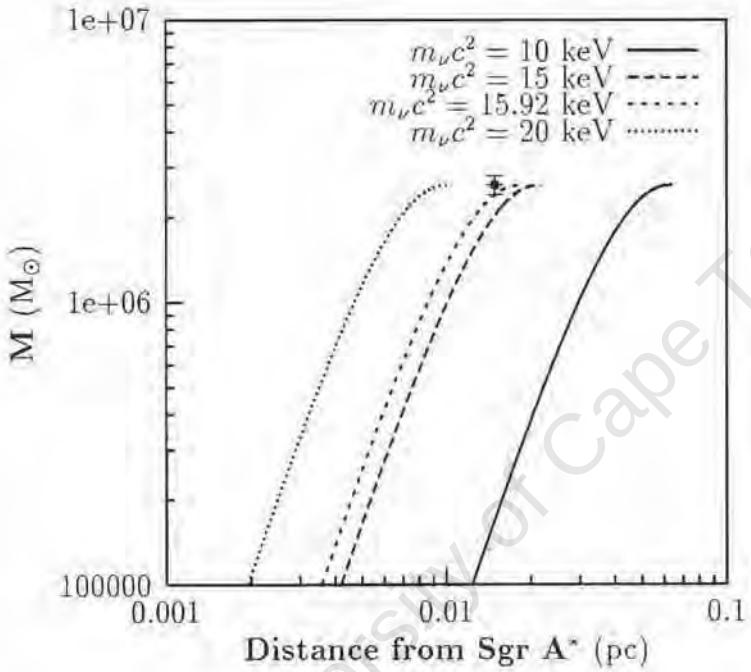

Figure 2.4: Mass enclosed M as a function of the distance from Sgr A* for different values of the neutrino mass m_ν. The spin degeneracy factor is $g_\nu = 2$. A neutrino mass of 15.9 keV/c^2 for $g_\nu = 2$ or 13.4 keV/c^2 for $g_\nu = 4$ is consistent with the the observed mass distribution at the Galactic center. The radius of a neutrino ball of $M = 2.6 \times 10^6 M_\odot$ would be 1.88×10^{-2} pc for the chosen value of the neutrino mass.

The gravitational potential due to a neutrino halo around the sun can then be written as

$$\Phi(r) = \frac{-GM_\odot}{r} + \frac{GM_\odot}{a_\nu}\left(\frac{1-v}{x} + v'(x_0)\right) = \Phi_B(r) + \delta\Phi_\nu(r), \tag{2.62}$$

where $\Phi_B(r)$ is the Newtonian potential due to the sun. i.e.

$$\Phi_B(r) = -\frac{GM_\odot}{r}, \tag{2.63}$$

and $\delta\Phi_\nu(r)$ is the contribution in the potential due to the presence of a neutrino halo around the sun

$$\delta\Phi_\nu(r) = \frac{GM_\odot}{a_\nu}\left(\frac{1-v}{x} + v'(x_0)\right). \tag{2.64}$$

Here v is the normalized potential that satisfies the Lané-Emden equation with a solar mass source at the center, i.e.

$$\frac{d^2v}{dx^2} = \frac{-v^{3/2}}{x^{1/2}}, \quad \text{with} \quad v(0) = 1 \quad \text{and} \quad v(x_0) = 0. \tag{2.65}$$

The mass of neutrinos and antineutrinos enclosed within a radius r of the halo is given by

$$M_\nu = -M_\odot\left(xv'(x) - v(x) + 1\right). \tag{2.66}$$

In Fig. 2.5 we plot the mass enclosed within a radius r from the sun for various values of the neutrino masses. The slope of v at the center has been chosen to be 1, i.e. $v'(0) = 1$ yielding a total mass of the halo of 0.7 $M_\odot$. Of course, by varying $v'(0)$ the halo could have any mass as we will see below. In this plot, we have included the observed mass excesses within the orbits of various outer planets, as obtained from astrometrical data and Voyager 1 and 2 and Pioneer 10 and 11 ranging data [80, 81], from which it is known that the dark mass within Jupiter's orbit is $M_d = (0.12 \pm 0.027)M_\odot$ while within Uranus' orbit $M_d \leq 0.5 \times 10^{-6} M_\odot$, and finally the dark mass within Neptune's orbit has been estimated to be $M_d \leq 3 \times 10^{-6} M_\odot$. Of course, the Jupiter data should be taken only as a lower limit, as Jupiter tends to eject almost any matter within its orbit [80]. Nevertheless, taking the Jupiter data at face value and interpreting dark matter as degenerate neutrino matter, the neutrino mass limits are

$$\begin{aligned} 12.8 \text{ keV} \leq \ & m_\nu c^2 \ \leq 14.2 \text{ keV for } g_\nu = 2, \\ 10.8 \text{ keV} \leq \ & m_\nu c^2 \ \leq 11.9 \text{ keV for } g_\nu = 1. \end{aligned} \tag{2.67}$$

For dark matter within Neptune's orbit, the neutrino mass range is

$$\begin{aligned} & m_\nu c^2 \ \leq 17 \text{ keV for } g_\nu = 2, \\ & m_\nu c^2 \ \leq 14.3 \text{ keV for } g_\nu = 4. \end{aligned} \tag{2.68}$$

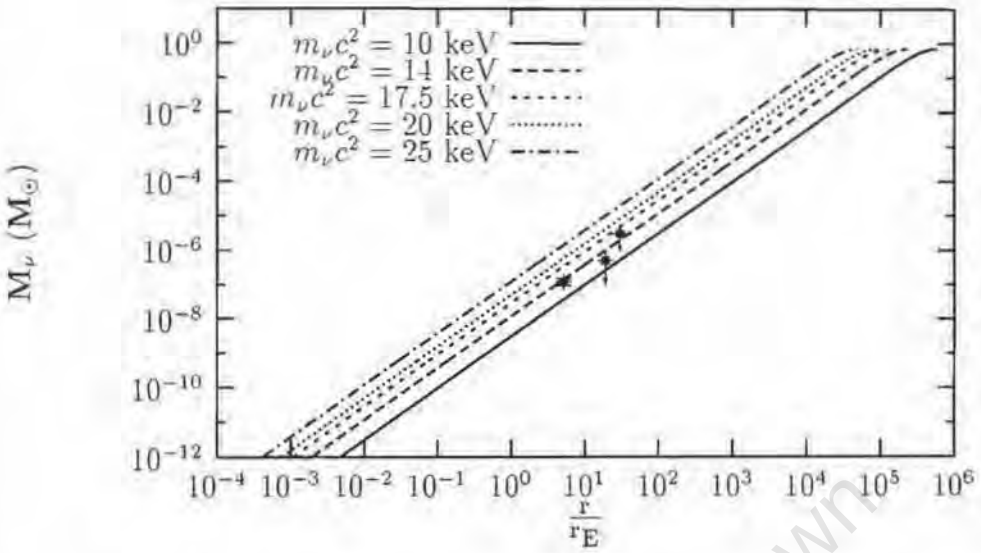

Figure 2.5: Mass of the neutrinos M_ν enclosed within a radius r in units of $r_E = 1$ AU from the sun for various neutrino masses. The total mass of the halo is $0.7M_\odot$. The observational data points with error bars [80] are also included. The arrows indicate upper limits.

Let us investigate how massive the halo of neutrinos should be in order to be consistent with the observed data. For this purpose, we have plotted the mass enclosed within a radius r for different masses of the halo in Fig. 2.6. The neutrino mass is fixed to 14 keV/c^2. It can be seen from this plot that a mass of the halo of more than $100M_\odot$ will not be consistent with the observed mass excesses within different orbits of the planetary system. In Fig. 2.7, the induced acceleration a due to the presence of a neutrino halo is plotted as a function of the radius from the center. In this plot, we have included the expected values of the acceleration within the orbits of different planets [81]. From this plot, we deduce that our model is consistent with the observations [81] but it cannot explain the apparent anomalous, weak, long-range acceleration from Pioneer 10/11, Galileo, and Ulysses Data [82, 83]. These groups claim that there is an anomalous acceleration a_P, towards the sun of $\sim 7.5 \times 10^{-8}$cm/s^2. No magnitude variation of a_P with distance was found, over a range of 40 to 60 AU. The discrepancy between the predicted values from our model and the anomalous acceleration is due to the fact that the mass of the neutrino halo enclosed with a radius r from the sun scales as $r^{3/2}$, whereas in the light of the recent observations [82, 83], the mass enclosed should go like r^2. In Fig. 2.8, we present the mass radius relation of neutrinos around the sun which shows a solution with a mass of $\sim 3M_\odot$ and a maximum radius of a few light years.

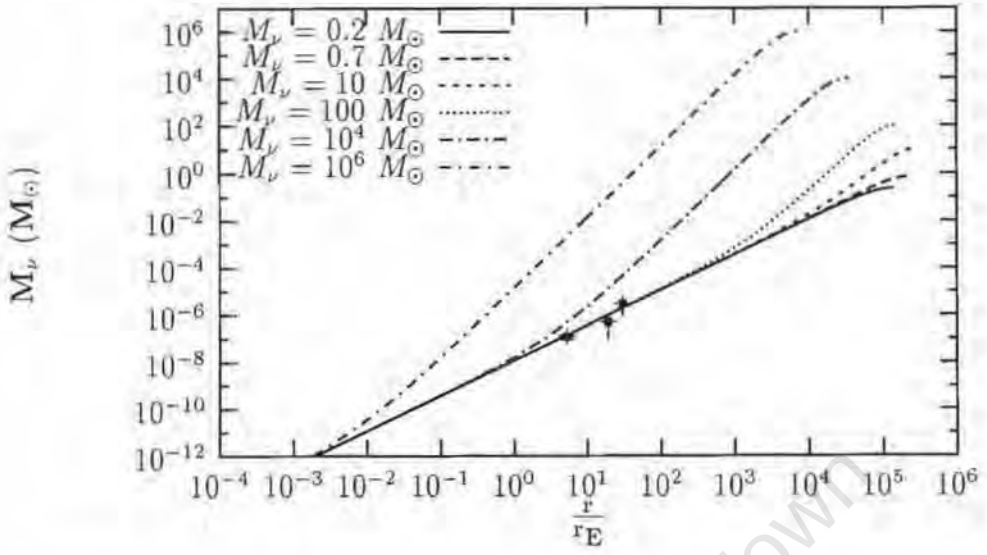

Figure 2.6: Mass of the neutrinos M_ν enclosed within a radius r from the sun. The total mass of the halo is varied and the neutrino mass is fixed to 11 keV/c^2. A neutrino halo of more than 100$M_\odot$ would not be consistent with the observed mass excess data from Pioneer 10 and 11 [80].

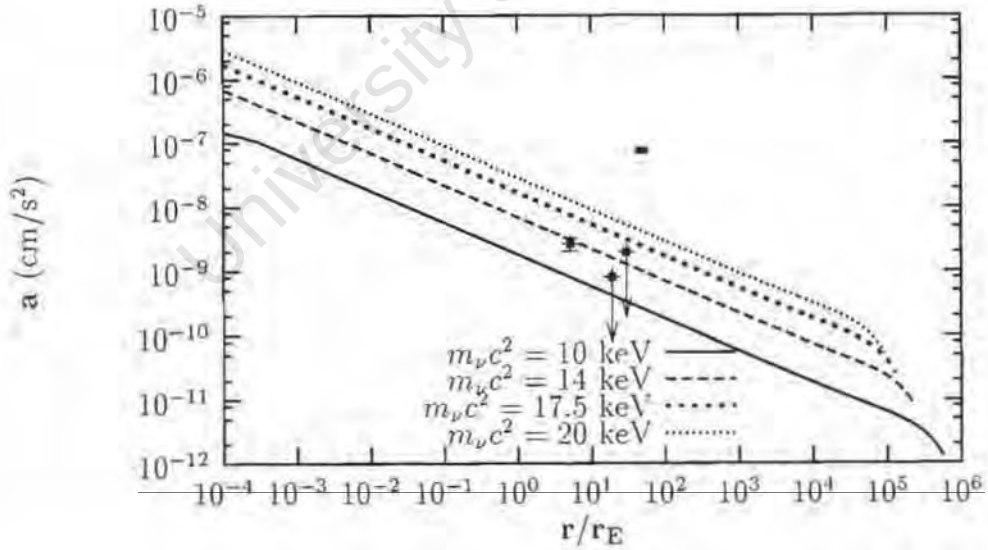

Figure 2.7: Excess acceleration a due to an assumed neutrino halo around the sun. The total mass of the halo is 0.7 $M_\odot$. The expected values of the acceleration using observational data points [80] are shown by points with arrows. The anomalous acceleration at 40-60 AU is indicated by a box.

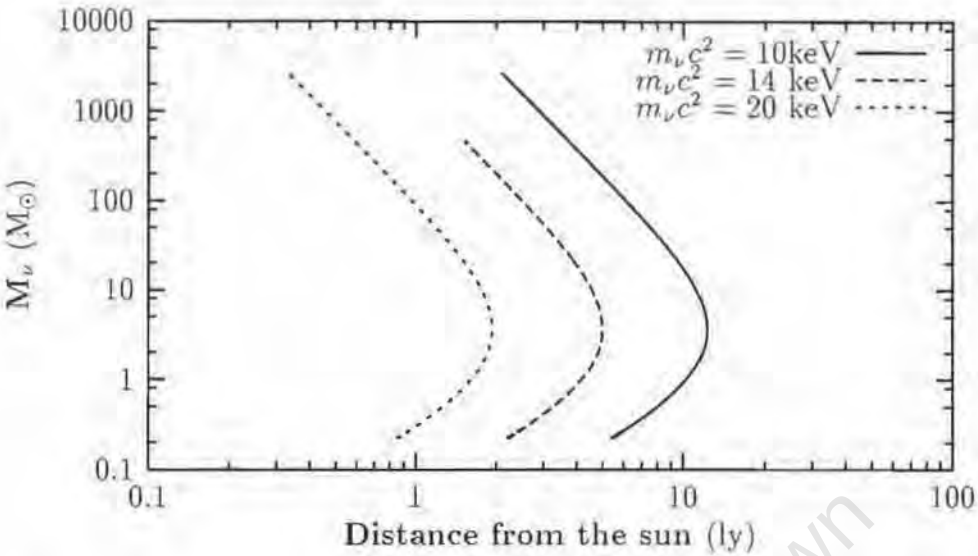

Figure 2.8: Mass radius-relationship of neutrino halos around the sun. The neutrino mass is varied as shown on the graph. The halo should have a maximum radius of a few light years.

2.6.2 Planetary perihelion shifts

We have shown in the previous section that the gravitational potential of the neutrinos around the sun can be written as sum of two terms. The first term is the gravitational potential due to the presence of a solar mass point source and the second term is due to an assumed degenerate heavy neutrino halo around the sun. In the vicinity of the sun, the second term $\delta\Phi_\nu(r)$ is much smaller than the first one, but it might have an effect on the motion of planets in the solar system. Near the center, the normalized potential $v(x)$ has the asymptotic behaviour

$$v(x) \approx \frac{-4}{3}x^{3/2} + v'(0)x + 1 \ , \tag{2.69}$$

where $v'(0)$ is the slope of the potential v at the point $x = 0$, and parametrizes solutions with different masses of the halo around the sun. Inserting the last expression into the equation (2.64) we find the additional potential energy due to the neutrinos

$$\delta U = m\delta\Phi_\nu(r) = \frac{4mGM_\odot}{3a_\nu^{3/2}}r^{1/2} + C, \tag{2.70}$$

where $C = v'(x_0) - 1$ is a constant. Our problem reduces to the investigation of the perihelion shifts of planets due to a small perturbation given by eq. (2.70) in addition to $-1/r$ potential.

In order to calculate the perihelion shifts, we use the fact that when a small correction $\delta U(r)$ is added to the potential energy $U = -\alpha/r$, the paths of finite motion are no longer closed, and at each revolution, the perihelion is displaced through a small angle $\delta\varphi$ [79] given by

$$\delta\varphi = \frac{\partial}{\partial L}\left(\frac{2m}{L}\int_0^{\pi} r^2 \delta U d\varphi\right). \tag{2.71}$$

Here L is the angular momentum, m is the mass of the particle and the unperturbed orbit of the particle has the standard elliptic equation, i.e.,

$$r = \frac{p}{1 + e\cos\varphi}, \tag{2.72}$$

with

$$p = a(1-e^2),\ e = 1 + \frac{2EL^2}{m\alpha^2},\ a = \frac{\alpha}{2E},\ \alpha = mGM_{\odot},\ L^2 = pm\alpha, \tag{2.73}$$

where e is the eccentricity, E is the energy of the particle ($E < 0$), a is the semi-major axis and p is the latus rectum.

Proof: For a finite motion in a central potential $U(r)$, the orbit is bound between circles of radii $r = r_{min}$ and $r = r_{max}$. During the time in which r varies from r_{min} to r_{max} and back, the radius vector turns through an angle $\delta\varphi$, which is given by

$$\delta\varphi = 2\int_{r_{min}}^{r_{max}} \frac{L dr/r^2}{\sqrt{[2m(E-U) - L^2/r^2]}}. \tag{2.74}$$

The last formula for $\delta\varphi$ can be rewritten as

$$\delta\varphi = -2\frac{\partial}{\partial L}\int_{r_{min}}^{r_{max}} \sqrt{\left[2m(E-U) - \frac{L^2}{r^2}\right]}\, dr\ . \tag{2.75}$$

We put $U = -\alpha/r + \delta U$, and expand the integrand in powers of δU; the zeroth-order term in the expansion gives 2π while the first order term gives the required change $\delta\varphi$, i.e.

$$\delta\varphi = \frac{\partial}{\partial L}\int_{r_{min}}^{r_{max}} \frac{2m\delta U dr}{\sqrt{\left[2m(E+\frac{\alpha}{r}) - \frac{L^2}{r^2}\right]}} = \frac{\partial}{\partial L}\left(\frac{2m}{L}\int_0^{\pi} r^2\delta U d\varphi\right)\ , \tag{2.76}$$

where we have changed the integration over r to one over φ, along the path of the "unperturbed" motion.

In the case of a halo of neutrino around the sun, the perturbation potential to $-\alpha/r$ is given by Eq. (2.70) and we can thus apply the formula (2.71) to calculate the perihelion shifts. It can be easily shown that the constant in

$\delta U'$ does not give any contribution to the shifts. Inserting $\delta U'$ in the equation (2.71), we obtain the following expression to be evaluated,

$$\begin{aligned}\delta\varphi &= \frac{8m^2GM_\odot}{3a_\nu^{3/2}}\frac{\partial}{\partial L}\left(\frac{1}{L}\int_0^\pi r^{5/2}d\varphi\right)\\ &= \frac{8m^2GM_\odot}{3a_\nu^{3/2}}\frac{\partial}{\partial L}\left(\frac{p^{5/2}}{L}\int_0^\pi \frac{1}{(1+e\cos(\varphi))^{5/2}}d\varphi\right)\end{aligned} \tag{2.77}$$

where p depends on the angular momentum L according to the equation (2.73). After integration and a little bit of straightforward algebra, we find the following expression for the shifts per one revolution:

$$\delta\varphi = -\frac{8}{3}\left(\frac{a}{a_\nu}\right)^{3/2}\frac{(e+1)(1-e)^{1/2}}{e^2}\Big[E(\pi/2,k)+(e-1)F(\pi/2.k)\Big], \tag{2.78}$$

where k is given by

$$k=\sqrt{\frac{2e}{1+e}}\,, \tag{2.79}$$

and $F(\pi/2,k)$ and $E(\pi/2,k)$ are the elliptic integrals of first and second kinds (see Appendix B), respectively, and they can be expressed as

$$F(\pi/2,k)=\int_0^{\pi/2}\frac{d\varphi}{\sqrt{1-k^2sin^2\varphi}}\,, \tag{2.80}$$

$$E(\pi/2,k)=\int_0^{\pi/2}d\varphi\sqrt{1-k^2sin^2\varphi}\,. \tag{2.81}$$

We can now write the expression for the shifts for a 100 years, to compare with the observed experimental values for different planets.

$$\begin{aligned}\delta\varphi &= -\frac{8}{3}\left(\frac{a}{a_\nu}\right)^{3/2}\frac{(e+1)(1-e)^{1/2}}{e^2}\Big[E(\pi/2,k)+(e-1)F(\pi/2,k)\Big]\\ &\times\frac{180\times 3600''}{\pi}\times\frac{100}{T}\,.\end{aligned} \tag{2.82}$$

In the last equation, T and a stand for the period and the semi-major axis of the planet, respectively. We then use the Kepler's third law to find the period of the planet as

$$T=T_E\frac{a^{3/2}}{a_E^{3/2}}, \tag{2.83}$$

where T_E and a_E are the period and the semi-major axis of the earth orbit, respectively. Excluding T from the Eq. (2.82), we get the final formula for the perihelion shifts due to a halo of neutrino around the sun, i.e.

$$\begin{aligned}\delta\varphi &= -5.5032''\times 10^5\left(\frac{a_E}{a_\nu}\right)^{3/2}\frac{(e+1)(1-e)^{1/2}}{e^2}\\ &\times\Big[E(\pi/2,k)+(e-1)F(\pi/2,k)\Big]\times\frac{100}{T_E}.\end{aligned} \tag{2.84}$$

The shifts do not depend on the semi-major axis a and are a function of the eccentricity only. Moreover, the shifts are negative in contrast to the general relativistic ones which are positive. In Fig. 2.9, we present the shifts due a neutrino halo as a function of the eccentricity. The data points show the difference between the experimental (Exp.) values and those due to general relativity theory (GRT), i.e. $\delta\varphi_{Exp.} - \delta\varphi_{GRT}$. A neutrino mass of 14 keV/c^2 has been used for the calculations and $g_\nu = 2$. The general relativistic perihelion shifts as well as the experimental values are taken from ref. [84]. It can be seen from Fig. 2.9 that, for planets with a very small eccentricity, the data points have large error bars. We can therefore obtain an upper bound for the neutrino mass using the perihelion shifts data of Icarus. In Fig. 2.10, the expected shifts are plotted for Icarus as a function of the neutrino mass. The horizontal lines show the predicted shifts $\delta\varphi_{Exp.} - \delta\varphi_{GRT}$. By assuming that the shifts due to a neutrino halo cannot be larger than the value of the error bars, i.e. $-1.3''$ as the shifts due to a degenerate neutrino halo are negative, we can find the upper bounds on the neutrino mass to be

$$\begin{aligned} m_\nu c^2 &\leq 16.4 \text{ keV for } g_\nu = 2, \\ m_\nu c^2 &\leq 13.8 \text{ keV for } g_\nu = 4\ . \end{aligned} \tag{2.85}$$

as can be seen from Fig. 2.10. Considering all the constraints on the neutrino mass (2.61),(2.68) and (2.85), we can conclude that a neutrino mass-range

$$\begin{aligned} 15.9 \text{ keV} \leq\ & m_\nu c^2 \leq 16.4 \text{ keV for } g_\nu = 2, \\ 13.4 \text{ keV} \leq\ & m_\nu c^2 \leq 13.8 \text{ keV for } g_\nu = 4. \end{aligned} \tag{2.86}$$

seems to be consistent with all reliable data.

2.6.3 Dark matter of constant density around the sun

In this section, we will study the shifts due a constant density distribution of dark matter around the sun using the method developed in the last section. With this assumption, the potential energy can be written as

$$\delta U(r) = -\left(3 - \left(\frac{r}{R}\right)^2\right)\frac{GmM}{2R}, \tag{2.87}$$

where M is the total mass of the dark matter ,i.e. $M = \frac{4\pi}{3}\rho_0 R^3$ and R is the radius up to which the halo of dark matter can extend. A model of dark matter with constant density using general relativity was considered [85] and it has been shown that one can put an upper bound on the density of dark matter from the perihelion motion of Icarus. We can use the equation (2.71) as in the previous section to calculate the planetary perihelion shifts due to

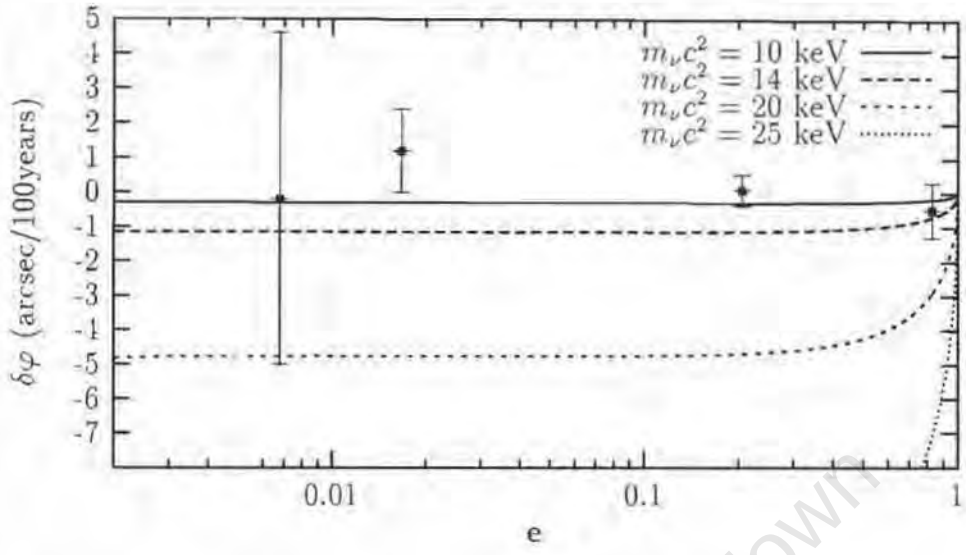

Figure 2.9: Perihelion shifts $\delta\varphi$ due to an assumed neutrino halo as a function of the eccentricity e. The data points with error bars denote the difference between the experimental (Exp.) and theoretical (GRT) values for the perihelion shifts.

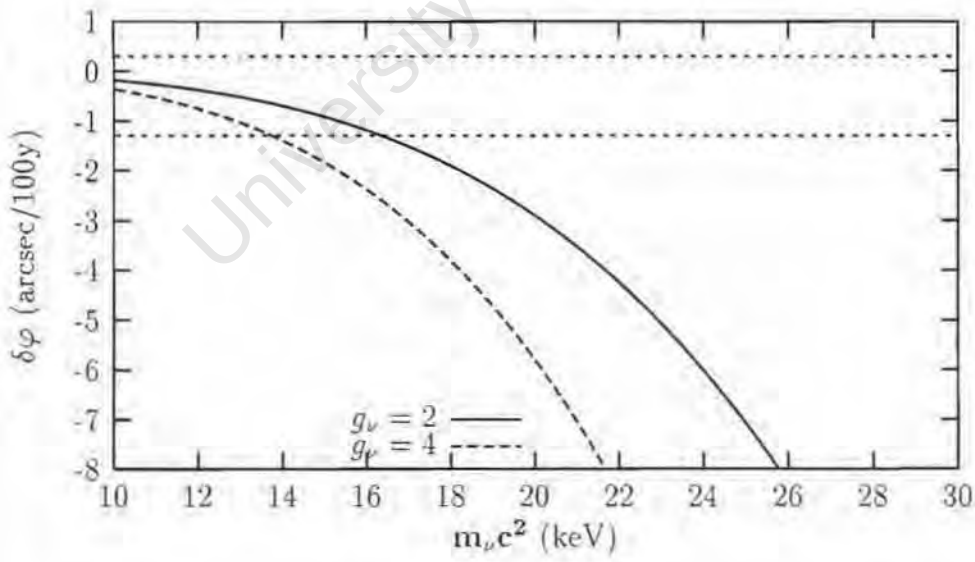

Figure 2.10: Icarus perihelion shifts $\delta\varphi$ as a function of the neutrino mass m_ν. The horizontal lines show the difference between the predicted values from experiments and general relativity theory (GRT).

the presence of a constant density dark matter. We get after integration, the following expression for the shifts

$$\delta\varphi = -\frac{4\pi^2\rho_0 a^3}{M_\odot}(1-e^2)^{1/2}, \tag{2.88}$$

which shows that the shifts are negative as in the previous case but depend on two parameters : the semi-major axis a and the eccentricity e.

We now apply this formula to Icarus. Its eccentricity e is 0.827, and its semi-major axis $a = 1.61 \times 10^{13}$ cm. The experimental value for the perihelion shifts is $9.8'' \pm 0.8''$ which gives a lower bound of $9''$ and an upper value of $10.6''$. The general relativistic shifts $6\pi GM_\odot/(a(1-e^2))$ are $10.3''$ [84]. By requiring that the shifts for 100 years should be less than $-1.3''$, i.e.

$$\delta\varphi \leq \delta\varphi_{Exp.} - \delta\varphi_{GRT}. \tag{2.89}$$

we get a bound on the density of dark matter in the solar system, i.e.

$$\rho_0 \leq 1.533 \times 10^{-15}\ \mathrm{g/cm^3}. \tag{2.90}$$

Using the value obtained for the density, one can estimate the mass of a spherical distribution of dark matter within the orbits of various planets. The mass within the earth orbit should be less than $1.1 \times 10^{-8} M_\odot$ which is in agreement with the bound obtained in ref. [86]. The dark mass within Uranus orbit should be less than $7.6 \times 10^{-5} M_\odot$ and finally the mass within Neptune is estimated to be less than $2.9 \times 10^{-4} M_\odot$.

2.7 Conclusion

In this chapter, we have shown that a neutrino ball is described by Lané-Emden equation and its gravitational potential is much shallower than that of a black hole of the same mass. We have shown that near the center, the neutrino ball potential can be approximated by an harmonic oscillator potential. We have established that neutrino balls can have a mass up to a few $10^9 M_\odot$ which is the upper limit for the purported black holes at the galactic centers. We have shown that the mass distribution at the Galactic center observed through stellar motion can be described by a neutrino ball of $2.6 \times 10^6 M_\odot$ made of neutrino of masses $m_\nu \geq 15.9\ \mathrm{keV}/c^2$ for $g_\nu = 2$ and $m_\nu \geq 13.4\ \mathrm{keV}/c^2$ for $g_\nu = 4$.

By considering a neutrino halo around the sun, we have found that the gravitational potential is dominated by the sun as a point source. We have established that the mass of an assumed neutrino halo around the sun is of the order of a few times $10^{-6} M_\odot$ within Neptune's orbit which is consistent with available observational data. We have found that the perihelion shifts due to

such a neutrino halo are negative in contrast to the general relativistic ones which are positive. In addition, the perihelion shifts depend only on one parameter, the eccentricity e while those due to general relativistic effects depend on the eccentricity e and the semi-major axis a. We have established a mass-radius relationship of neutrino halos around the sun and have shown that there is a solution with a mass of $\sim 3\ M_{\odot}$ and a maximum radius of a few light years.

In order to explain the mass excesses within the orbits of different orbits from Voyager and Pioneer 10/11, the bounds on the neutrino mass have been established. The predicted values of the acceleration in the solar system have been compared to those obtained from the recent observations. Finally, we have shown that in order to be consistent with observations, the mass of the neutrino halo cannot exceed $\sim 100\ M_{\odot}$.

Chapter 3

Degenerate relativistic neutrino halos around compact stars

3.1 Degenerate relativistic neutrino balls

3.1.1 Relativistic equations of hydrostatic equilibrium

A spherically symmetric cloud of degenerate neutrino matter can be characterized by its mass density $\rho_\nu(r)$, pressure $P_\nu(r)$, and the metric in the Schwarzschild form [87, 88]

$$ds^2 = e^{\nu}c^2dt^2 - e^{\lambda}dr^2 - r^2(d\theta^2 + \sin^2\theta d\phi^2). \tag{3.1}$$

The pressure and the density satisfy the relativistic Tolman-Oppenheimer Volkoff (TOV) equations of hydrostatic equilibrium [89, 90]

$$\frac{dP_\nu}{dr} = -\frac{1}{2}(\rho_\nu c^2 + P_\nu)\frac{d\nu}{dr}, \tag{3.2}$$

$$e^{\lambda} = \left(1 - \frac{2Gm}{c^2 r}\right)^{-1}, \tag{3.3}$$

$$\frac{dP_\nu}{dr} = -G\frac{(\rho_\nu + P_\nu/c^2)(m + 4\pi r^3 P_\nu/c^2)}{r(r - 2Gm/c^2)}, \tag{3.4}$$

$$\frac{dm}{dr} = 4\pi r^2 \rho_\nu(r), \tag{3.5}$$

where $m(r)$ is the mass enclosed within a radius r. The relevant boundary conditions are $m(0) = 0$, $P_\nu(R) = 0$, and $\rho_\nu(R) = 0$, as the pressure and the density vanish at the radius R of the neutrino ball. Outside the ball, the functions ν and λ are determined by the usual Schwarzschild solution

$$e^{\nu} = e^{-\lambda}, \qquad e^{\lambda} = (1 - 2GM/c^2 r)^{-1}, \tag{3.6}$$

$$M = \int_0^R 4\pi \rho_\nu(r) r^2 dr. \tag{3.7}$$

We now introduce the equation of state, neglecting possible effects of the dissipation mechanism. Of course, in the formation process, which will not be discussed in this thesis, such a dissipation mechanism is very important. However, as soon as the degenerate ball is formed, the dissipation mechanism is irrelevant and does not affect the equation of state. Thus, the equation of state may be approximated by that of a degenerate relativistic Fermi gas [91], parameterized as

$$P_\nu = K\left[X(1+X^2)^{1/2}\left(\frac{2}{3}X^2 - 1\right) + \log\left(X + (1+X^2)^{1/2}\right)\right]. \tag{3.8}$$

$$\rho_\nu = \frac{K}{c^2}\left[X(1+X^2)^{1/2}(2X^2+1) - \log\left(X + (1+X^2)^{1/2}\right)\right], \tag{3.9}$$

$$n_\nu = \frac{8KX^3}{3m_\nu c^2}. \tag{3.10}$$

Here, n_ν denotes the neutrino-number density, and K and X are given by

$$K = \frac{g_\nu m_\nu^4 c^5}{16\pi^2\hbar^3}, \quad X = \frac{p_\nu}{m_\nu c}. \tag{3.11}$$

where p_ν stands for the local Fermi momentum of the neutrinos of mass m_ν, and g_ν is the spin degeneracy factor of neutrinos and antineutrinos, i.e., $g_\nu = 2$ for Majorana and $g_\nu = 4$ for Dirac neutrinos and antineutrinos. Using (3.8) and (3.9), and introducing dimensionless variables $x = r/a_\nu$ and $\mu = m/b_\nu$ with the scales

$$a_\nu = 2\sqrt{\frac{\pi}{g_\nu}}\left(\frac{M_{\rm Pl}}{m_\nu}\right)^2 L_{\rm Pl} = 2.88233 \times 10^{10} g_\nu^{-1/2}\left(\frac{17.2\ {\rm keV}}{m_\nu c^2}\right)^2 {\rm km}, \tag{3.12}$$

$$b_\nu = 2\sqrt{\frac{\pi}{g_\nu}}\left(\frac{M_{\rm Pl}}{\pi m_\nu}\right)^2 M_{\rm Pl} = 1.95197 \times 10^{10} M_\odot g_\nu^{-1/2}\left(\frac{17.2\ {\rm keV}}{m_\nu c^2}\right)^2, \tag{3.13}$$

where $M_{\rm Pl} = (\hbar c/G)^{1/2}$ and $L_{\rm Pl} = (\hbar G/c^3)^{1/2}$ denote Planck's mass and length, respectively, the TOV equations (3.4) and (3.5) can be written as

$$\begin{aligned}\frac{dX}{dx} &= -\frac{1+X^2}{X(x^2 - 2\mu x)}\Big\{\mu + x^3\Big[X(1+X^2)^{1/2}\left(\frac{2}{3}X^2 - 1\right) \\ &\quad + \log\left(X + (1+X^2)^{1/2}\right)\Big]\Big\},\end{aligned} \tag{3.14}$$

$$\frac{d\mu}{dx} = x^2\left[X(1+X^2)^{1/2}(2X^2+1) - \log\left(X + (1+X^2)^{1/2}\right)\right], \tag{3.15}$$

subject to the boundary conditions $X(0) = X_0$ and $\mu(0) = 0$. In addition to (3.14) and (3.15), there is also an equation governing the number of neutrinos n within a radius $r = a_\nu x$

$$\frac{d\tilde{n}}{dx} = x^2 X^3 (1 - 2\mu/x)^{-1/2} , \tag{3.16}$$

where $\tilde{n} = n/N_0$ is the rescaled number of neutrinos subject to the boundary condition $\tilde{n}(0) = 0$, with

$$N_0 = \frac{8b_\nu}{3m_\nu} = 3.3765 \times 10^{72} \left(\frac{17.2 \text{ keV}}{m_\nu c^2}\right)^3 g_\nu^{-1/2}. \tag{3.17}$$

The central number density can be obtained from Eq. (3.10) and has the following form

$$n_c = \frac{8KX_0^3}{3m_\nu c^2} = n_0 X_0^3, \tag{3.18}$$

where the the constant n_0 is given by

$$n_0 = \frac{8K}{3m_\nu c^2} = 1.1190 \times 10^{25} g_\nu \left(\frac{m_\nu c^2}{17.2 \text{ keV}}\right)^3 \text{ cm}^{-3}. \tag{3.19}$$

3.1.2 Solutions of the Tolman-Oppenheimer Volkoff equations

Equations (3.14)-(3.16) may be solved numerically. Picking up a value X_0 for the Fermi momentum at the center (in units of $m_\nu c$), one obtains the total mass of the ball M, the radius R, and the total number of particles N, by integrating outward until X vanishes.

The results are summarized in Figs. 3.1 to 3.6. The total mass M, the radius R and the total number of particles N are presented as functions of the central number density n_c in Fig. 3.1 to Fig. 3.3, respectively. In Fig. 3.4, the total mass is plotted against the radius of the neutrino ball. The curve has a maximum, namely, the Oppenheimer-Volkov (OV) limit [90], at $\mu_{\rm OV} = 0.15329$, which corresponds to a neutrino ball mass of

$$\begin{aligned} M_{\rm OV} &= 0.15329\, b_\nu = 0.54195\, M_{\rm Pl}^3 m_\nu^{-2} g_\nu^{-1/2} \\ &= 2.9924 \times 10^9 M_\odot \left(\frac{17.2 \text{ keV}}{m_\nu c^2}\right)^2 g_\nu^{-1/2}. \end{aligned} \tag{3.20}$$

The total mass of the neutrino ball M is plotted against the total number of particles N in Fig. 3.5. For masses much smaller than the OV limit, the relation between M and N is unique. However, as M approaches the OV limit, M becomes a multivalued function of N. The part of the curve on the

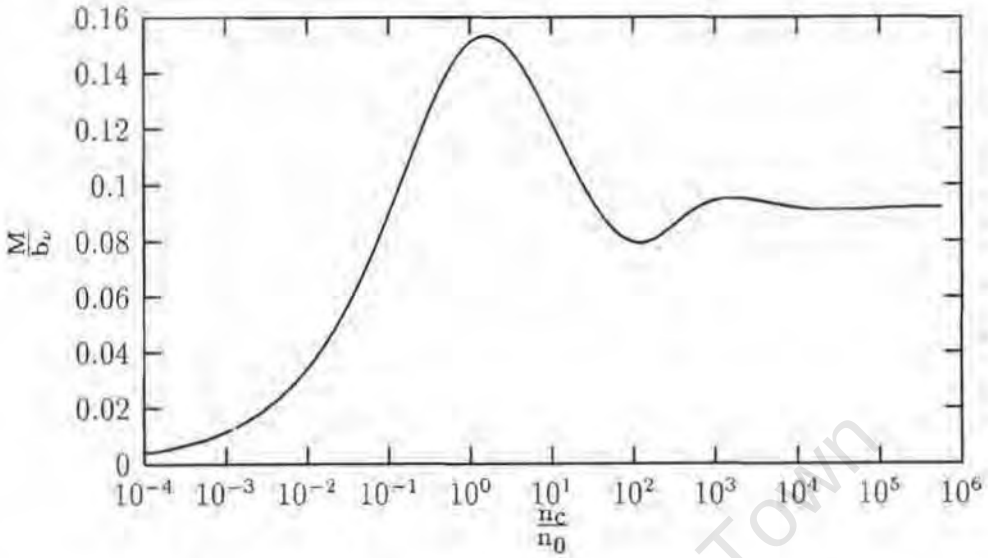

Figure 3.1: Total mass M of the neutrino ball in units of b_ν as a function of the central number density n_c in units of n_0.

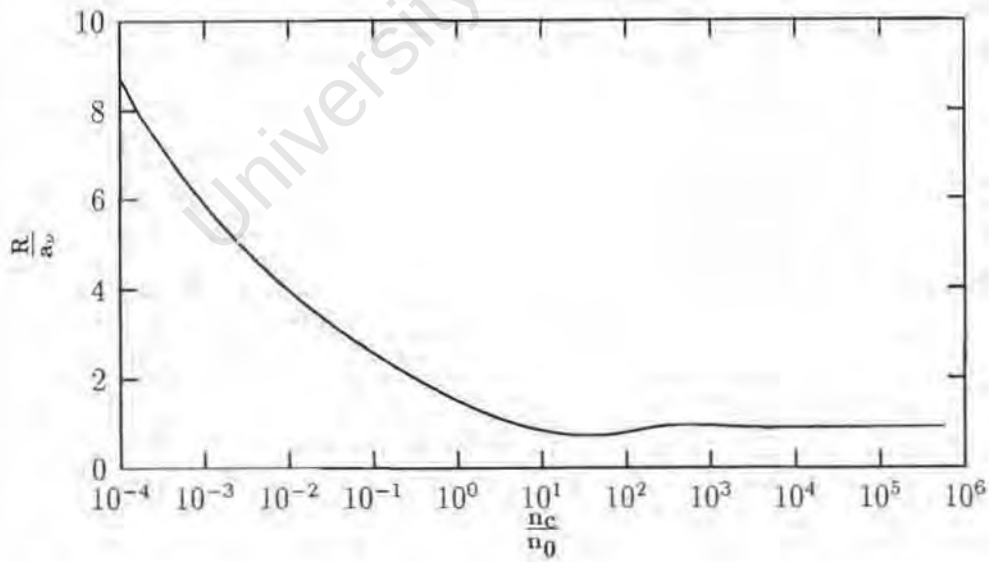

Figure 3.2: The radius R of the neutrino ball in units of a_ν as a function of the central number density n_c in units of n_0.

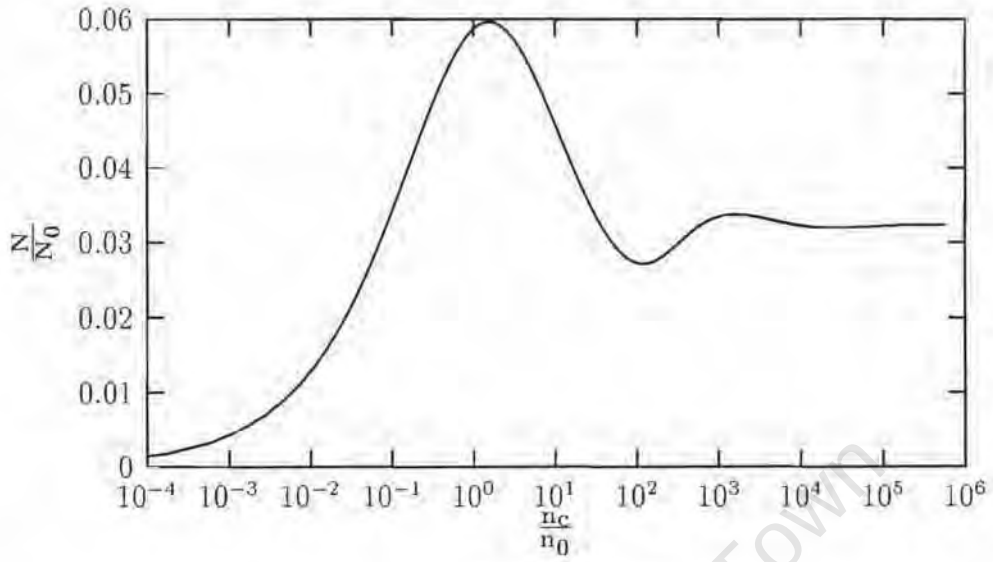

Figure 3.3: The total number of particles N in units of N_0 as a function of the central number density n_c in units of n_0.

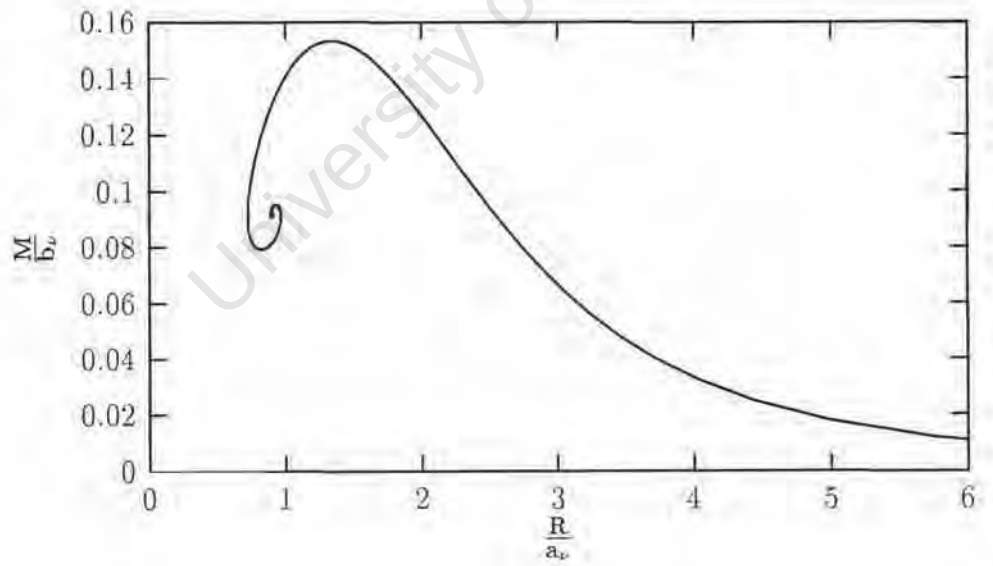

Figure 3.4: The total mass M of a neutrino ball in units of b_ν as a function of its radius R in units of a_ν. The maximum corresponds to the OV limit. The curve left from the maximum represents unstable configurations curling up around the point of infinite central density.

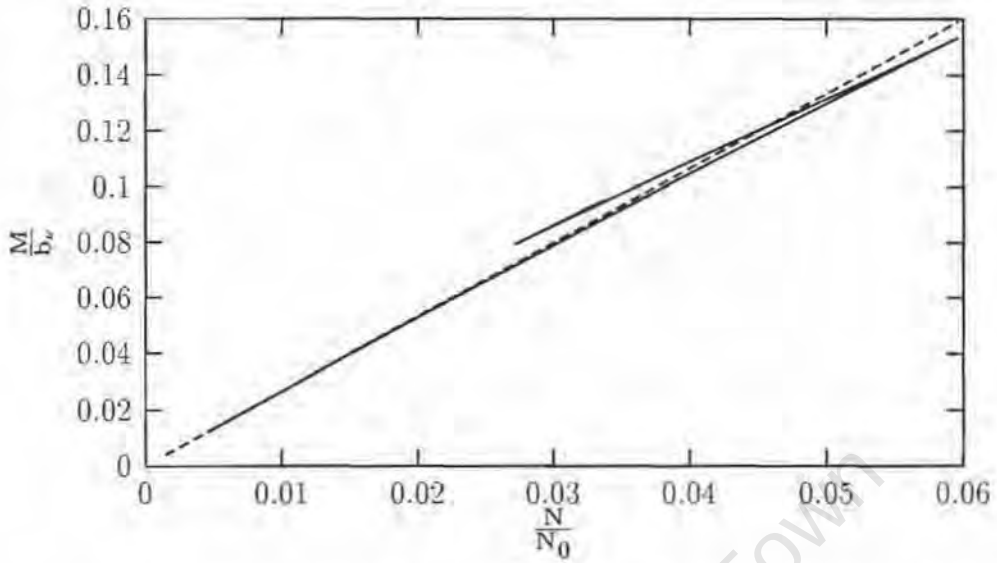

Figure 3.5: The total mass M of a neutrino ball in units of b_ν as a function of its total number of particles N in units of N_0. The dashed line corresponds to $M = Nm_\nu$. The configurations left from the point of intersection of the two curves lie deeply in the instability region.

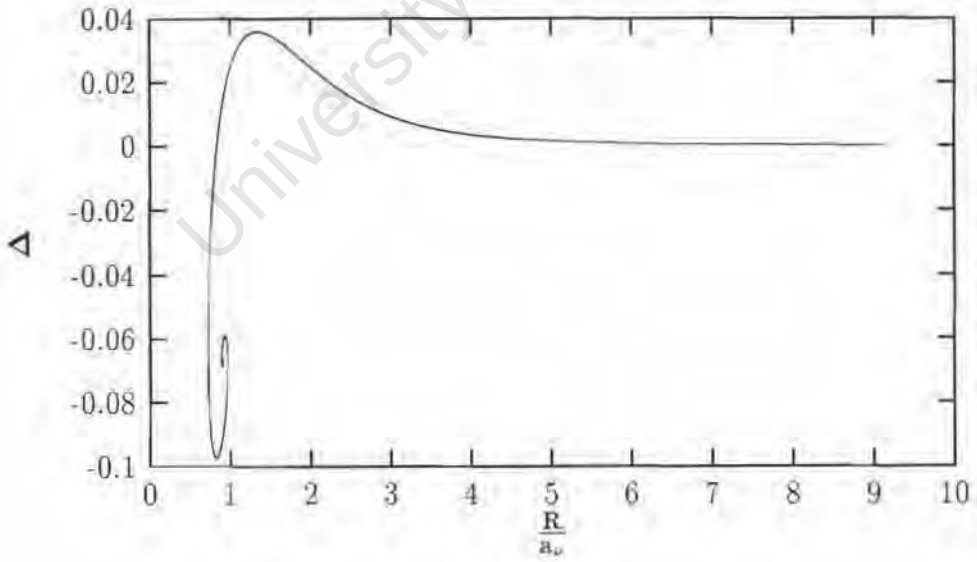

Figure 3.6: The relative mass defect Δ as a function of the radius R of the neutrino ball. The configurations with $\Delta < 0$ are absolutely unstable since the system can gain energy by disintegrating.

left side of the maximum in Fig. 3.4, which corresponds to the upper part of the curve in Fig. 3.5, represents unstable configurations [87, 92] for which the relative mass defect

$$\Delta = \frac{Nm_\nu - M}{Nm_\nu}, \tag{3.21}$$

eventually becomes negative, as seen in Fig. 3.6. Thus, for $\Delta < 0$, the system can gain energy by disintegrating. The maximal relative mass defect, or the strongest binding, is obtained at the OV limit with $\Delta_{\rm OV} = 3.5807 \times 10^{-2}$.

3.1.3 The Oppenheimer-Volkoff and the black hole limits

We have seen from the last section that the TOV equations admit a solution with a maximum mass M_{OV} given by Eq. (3.20). The radius of such a neutrino ball that is close to being a black hole is

$$\begin{aligned} R_{\rm OV} &= 4.8329 \times \left(\frac{\hbar^3}{Gc}\right) m_\nu^{-2} g_\nu^{-1/2} \\ &= 1.5171 \times \left(\frac{17.2\ {\rm keV}}{m_\nu c^2}\right)^2 g_\nu^{-1/2}\ {\rm ld} \\ &= 4.4166 R^S_{\rm OV}, \end{aligned} \tag{3.22}$$

where $R^S_{\rm OV} = 2GM_{\rm OV}/c^2$ is the Schwarzschild radius of the mass $M_{\rm OV}$. Thus, at a distance of a few Schwarzschild radii away from the supermassive object, there is little difference between a neutrino ball at the OV limit and a black hole, in particular since the last stable orbit around a black hole already has a radius of 3 $R^S_{\rm OV}$. A neutrino ball of mass $M_{\rm OV} = 3 \times 10^9\ M_\odot$ would have a radius $R_{\rm OV} = 3.9396 \times 10^{10}$ km, or 1.52 light-days.

In Fig. 3.7, the mass-radius relation of neutrino balls in general relativity and Newtonian theory is shown. We deduce from this plot, that general relativistic corrections reduce the mass limit of neutrino balls $M_{\rm BH}$ (see chapter 2) by a factor of 4.8037, i.e.

$$M_{\rm BH} = 4.8037 M_{\rm OV} \tag{3.23}$$

where $M_{\rm OV}$ is the Oppenheimer Volkoff limit as defined from Eq. (3.20).

Owing to their large mass, neutrino balls could serve as candidates for supermassive compact dark objects observed in the mass range

$$2.5 \times 10^6\ M_\odot \lesssim M \lesssim 3 \times 10^9\ M_\odot \tag{3.24}$$

at the centers of a number of galaxies. Assuming that the most massive and violent objects are neutrino balls at the OV limit with $M_{\rm OV} = (3.2 \pm 0.9) \times$

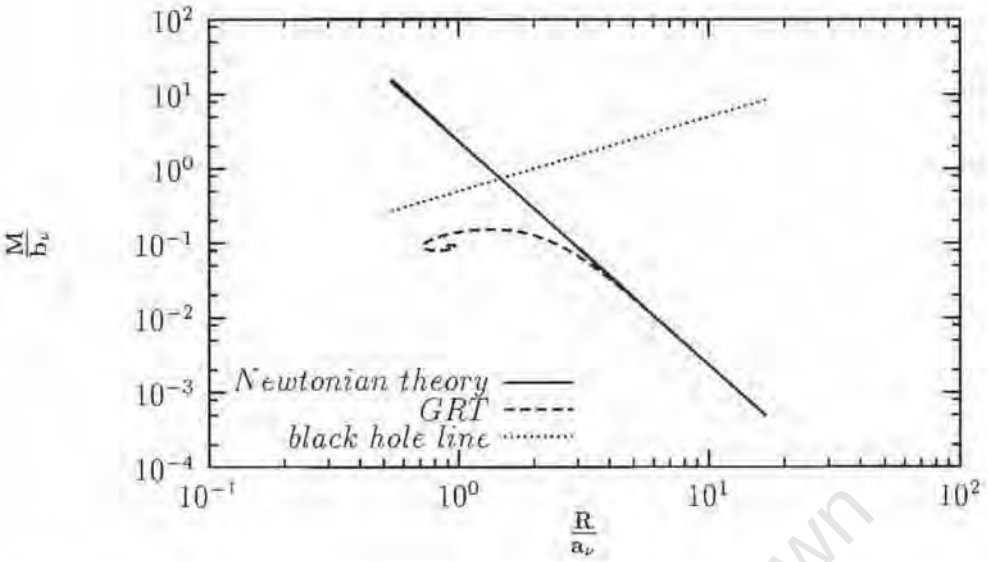

Figure 3.7: Mass radius relation of neutrino balls in general relativity theory (GRT) and Newtonian theory. The black hole line is also shown. The point where the black hole line intersects the non-relativistic mass-radius line corresponds to the black hole mass limit $M_{\rm BH}$ for neutrino balls. The general relativistic corrections reduce $M_{\rm BH}$ by a factor of 4.8037.

$10^9\ M_\odot$, such as the supermassive compact dark object at the center of M87 [25], the neutrino mass required for this scenario is

$$\begin{aligned} 12.4\,\mathrm{keV}/c^2 \leq\ & m_\nu \ \leq 16.5\,\mathrm{keV}/c^2 \quad \text{for } g_\nu = 2, \\ 10.4\,\mathrm{keV}/c^2 \leq\ & m_\nu \ \leq 13.9\,\mathrm{keV}/c^2 \quad \text{for } g_\nu = 4. \end{aligned} \tag{3.25}$$

Of course, neutrino balls that are well below the OV limit will have a size much larger than black holes of the same mass, although they will still be dark and much more compact than any known baryonic object of the same mass. As the gravitational potential of such an extended neutrino ball is much shallower, significantly less energy will be dissipated through accreting matter than in the case of a black hole of the same mass. In fact, there is compact dark matter at the center of our galaxy with $(2.6 \pm 0.2) \times 10^6\ M_\odot$ concentrated within a radius smaller than 0.015 pc [26, 27, 28], determined from the motion of stars in the vicinity of Sgr A*. Interpreting this supermassive compact dark object in terms of a degenerate neutrino ball of $2.6 \times 10^6\ M_\odot$, the upper limit for the size of the object provides us with a lower limit for the neutrino mass, i.e.,

$$\begin{aligned} m_\nu \ &\geq 15.92\,\mathrm{keV}/c^2 \quad \text{for } g_\nu = 2, \\ m_\nu \ &\geq 13.39\,\mathrm{keV}/c^2 \quad \text{for } g_\nu = 4. \end{aligned} \tag{3.26}$$

In this context, it is important to note that if Sgr A* is a matter-accreting neutrino ball [30, 31, 32], one can, in a natural way, explain the so-called "blackness problem" of Sgr A*, i.e., the the fact that Sgr A* does not seem to emit detectable x-rays of a few tens of keV, which would be emitted by baryonic matter falling towards a black hole (see chapter 4). As this unmistakable black hole signature is missing, the concept of a "black hole on starvation diet" has been created in order to save the black hole idea. However, the neutrino ball model also fits the enigmatic radio emission of Sgr A* much better than the "black hole on starvation diet" model .

3.1.4 TOV equations and the Newtonian limit

The Newtonian limit corresponds to the case of of small Fermi momenta, i.e. $X \ll 1$. With this assumption, the equation of state, e.g., Eqs. (3.8) and (3.9) for neutrino matter can be written as

$$P_\nu = \frac{8K}{15} X^5, \tag{3.27}$$

$$\rho_\nu = \frac{8K}{3c^2} X^3. \tag{3.28}$$

The last two equations (3.27) and (3.28) can be combined to yield the equation of state of a nonrelativistic degenerate Fermi gas, i.e.,

$$P_\nu = \left(\frac{6}{g_\nu}\right)^{2/3} \rho_\nu^{5/3} \frac{\pi^{4/3}\hbar^2}{5m_\nu^{8/3}}, \tag{3.29}$$

as expected.

For completeness, we note that in the Newtonian limit, the TOV equations (3.14) and (3.15) reduce to

$$\frac{dX}{dx} = -\frac{\mu}{x^2 X}, \tag{3.30}$$

$$\frac{d\mu}{dx} = \frac{8}{3} x^2 X^3 , \tag{3.31}$$

which, using the substitution $\Theta = X^2$ and $\xi = 4x/\sqrt{3}$, can be cast into the nonlinear Lané-Emden differential equation with the polytropic index 3/2 [93]

$$\frac{1}{\xi^2}\frac{d}{d\xi}\left(\xi^2 \frac{d\Theta}{d\xi}\right) = -\Theta^{3/2} . \tag{3.32}$$

Owing to the scaling property of the Lané-Emden equation, the mass and radius of a nonrelativistic neutrino ball scale as [36]

$$MR^3 = \frac{91.869\,\hbar^6}{G^3 m_\nu^8}\left(\frac{2}{g_\nu}\right)^2 . \tag{3.33}$$

For large central densities $X_0 \gg 1$, μ oscillates around $\mu_\infty = 0.09196$, which corresponds to a neutrino ball mass $M_\infty = 1.795 \times 10^9 M_\odot g_\nu^{-1/2}$ for a neutrino mass $m_\nu = 17.2$ keV/c^2. For a gas of neutralinos of a mass precisely equal to the neutron mass $m_n = 0.93955$ GeV/c^2 and a degeneracy factor $g_n = 2$, the infinite density limit is $M_\infty = 0.4164\ M_\odot$, whereas the OV limit is $M_{\rm OV} = 0.7091\ M_\odot$ and $R_{\rm OV} = 9.1816$ km [92]. Thus, owing to their compactness, neutralino balls could mimic the properties of "machos" which have been detected in the line-of-sight towards the Large Magellanic Cloud (LMC) [52, 53]. If these objects are located in our galactic halo (rather than in the LMC), their masses seem to be about 0.4 $M_\odot$. Thus we are faced with the dilemma that, on the one hand, they are 5 times too heavy for brown dwarfs, and, on the other hand, they cannot be luminous stars, because they would have been easily detected. Therefore, the baryonic matter interpretation of these "machos" is disfavoured [53]. If one wants to interpret these objects as neutralino stars, the mass of the neutralino m_n is restricted to 1.22 MeV/$c^2 \leq m_n < 1.251$ GeV/c^2, for a degeneracy factor of $g_n = 2$. The lower limit is obtained restricting the size of the dark object, i.e. we have somewhat arbitrarily constrained the radius of the "macho" to $R \leq 0.25$ AU which is much smaller than the average Einstein radius of about 3 AU. As 0.25 AU is the distance a star would travel at a speed of $v_\odot = 220$ km/s in approximately two days, this would not affect the light-curve too much, since the average time scale of the lensing events is about 88 days. The upper limit is obtained assuming that $M_{\rm OV} \approx 0.4\ M_\odot$ is at the Oppenheimer-Volkoff limit, i.e. it is almost a black hole.

For large X, the solutions of the TOV equations (3.11) and (3.15) tend to

$$\mu = \frac{3}{14}\, x \quad \text{and} \quad X = \left(\frac{3}{28}\right)^{1/4} x^{-1/2}. \tag{3.34}$$

The pressure and the density thus become

$$P_\nu = \frac{c^4}{56\pi}\,\frac{1}{r^2} \quad \text{and} \quad \rho_\nu = \frac{3c^2}{56\pi}\,\frac{1}{r^2}, \tag{3.35}$$

yielding the equation of state of radiation

$$P_\nu = \frac{1}{3}\, c^2 \rho_\nu, \tag{3.36}$$

as expected.

3.2 Mass-radius relation of white dwarfs

In this section, we will investigate the effects of general relativity on the structure of white dwarfs. The classical theory of white dwarfs has been

presented by Chandrasekhar in his pioneering works in which he discovered that a degenerate electron gas interacting with nucleons has a maximum mass of $\sim 1.4 M_\odot$ [93, 94]. The Chandrasekhar analysis was based on the following assumptions: (1) *Newtonian* equation of hydrostatic equilibrium, (2) cold matter, (3)pressure supplied by an ideal relativistic degenerate Fermi gas of electrons, and by this gas only; (1) the mass density and therefore the potential is provided by nucleons. This result was found after Landau [95] gave a general argument that a sufficiently large collection of cold matter cannot sustain itself against gravitational collapse. A white dwarf consists of two types of particles: nucleons which provide the gravitational potential and the electrons that are responsible for degeneracy pressure. Let us denote by Y, the normalized local Fermi momentum of electrons (in units of $m_e c$), by P_e, the electrons pressure and by ρ_{eH}, the total mass energy density of nucleons and electrons. The equation of state of a white dwarf can therefore be written as

$$P_e = K\left[Y(1+Y^2)^{1/2}\left(\frac{2}{3}Y^2-1\right)+\log\left(Y+(1+Y^2)^{1/2}\right)\right], \tag{3.37}$$

$$\begin{aligned}\rho_{eH} &= \frac{K}{c^2}\left[Y(1+Y^2)^{1/2}(2Y^2+1)-\log\left(Y+(1+Y^2)^{1/2}\right)\right] \\ &+\frac{8K}{3m_e c^2}\mu_e m_p Y^3,\end{aligned} \tag{3.38}$$

where the constant K is in this case defined as

$$K=\frac{g_e m_e^4 c^5}{16\pi^2\hbar^3}, \tag{3.39}$$

Here m_e is the electron mass, g_e is the spin degeneracy factor for electrons and is equal to 2, m_p is the proton mass, and μ_e is the molecular weight per electron, i.e. $\mu_e = A/Z$ where A is the atomic number and Z the number of electrons (μ_e is 1 for H, 2 for $^4_2$He particles and 2.17 for ^{56}Fe). The first term in the energy matter density is the electrons contribution while the second term is due to nucleons. For non-relativistic electrons, the mass energy density due to electrons is negligible compared to the contribution due to protons. Inserting the equation of state (3.37) and (3.38) into the TOV equations (3.4) and (3.5), and introducing normalized variables $x = r/a_e$ and $\mu = m(r)/b_e$, we get the following set of equations which describe a relativistic white dwarf:

$$\begin{aligned}\frac{dY}{dx} &= -\frac{1+Y^2}{Y(x^2-2\mu x)}\left(\frac{\mu_e m_p}{m_e}+(1+Y^2)^{1/2}\right)\left\{\mu+x^3\right. \\ &\left.\times\left[Y(1+Y^2)^{1/2}\left(\frac{2}{3}Y^2-1\right)+\log\left(Y+(1+Y^2)^{1/2}\right)\right]\right\}.\end{aligned} \tag{3.40}$$

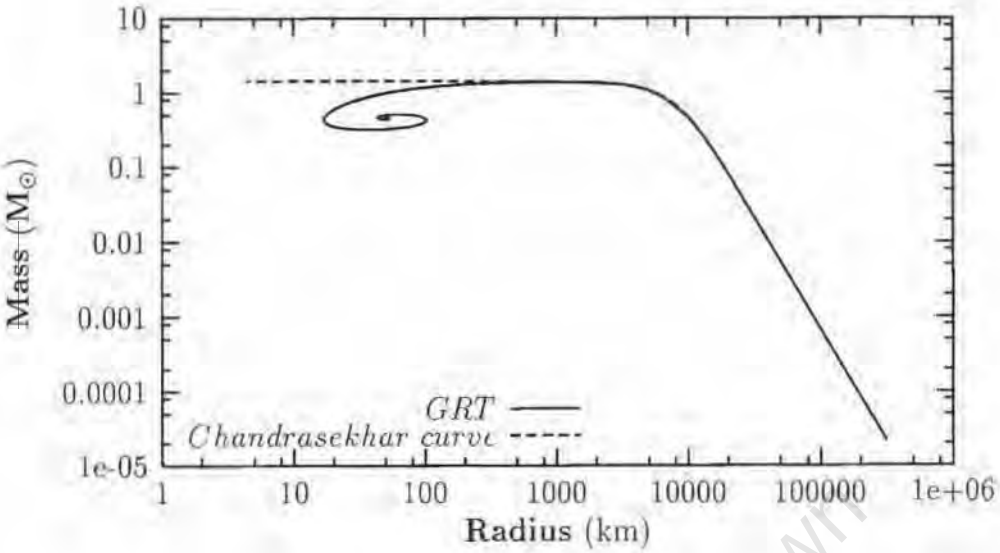

Figure 3.8: Mass radius relation of white dwarfs using general relativity theory (GRT) and Newtonian theory . In the case of GRT, the graph has a maximum, the OV limit of $M_{\rm wd} = 1.394 M_\odot$ which is almost equal to the Chandrasekhar limit of $\sim 1.4\ M_\odot$. Left from the OV limit, i.e. for radii less than 1018 km, all the solutions are unstable.

$$\frac{d\mu}{dx} = x^2\Big[\frac{8}{3}\frac{\mu_e m_p}{m_e}Y^3 + Y(1+Y^2)^{1/2}(2Y^2+1) - \log\left(Y+(1+Y^2)^{1/2}\right)\Big], \tag{3.41}$$

subject to the boundary conditions $Y(0) = Y_0$ and $\mu(0) = 0$. The constants a_e and b_e are the length and mass scales, respectively. They can be obtained from a_ν and b_ν given by Eqs. (3.12) and (3.13) by making the replacements $m_\nu \leftrightarrow m_e$, and $g_\nu \leftrightarrow g_e$, i.e.

$$a_e = 2.88233 \times 10^{10} g_e^{-1/2} \left(\frac{17.2\ \text{keV}}{m_e c^2}\right)^2 \text{km} = 2.3091 \times 10^7\ \text{km}, \tag{3.42}$$

$$b_e = 1.95197 \times 10^{10} M_\odot g_e^{-1/2} \left(\frac{17.2\ \text{keV}}{m_e c^2}\right)^2 = 1.5638 \times 10^7 M_\odot. \tag{3.43}$$

In the Newtonian limit, i.e. $X_0 \ll 1$ the equation of state for the white dwarf can be written as

$$P_e = \frac{8K}{15}X^5, \tag{3.44}$$

$$\rho_{eH} = \frac{8K}{3m_e c^2}\mu_e m_p X^3, \tag{3.45}$$

Here, the constant K is given by Eq. (3.39). From Eq. (3.45) one can express X as a function of ρ_{eH}

$$X = \left(\frac{3c^2\rho_{eH}}{8aK}\right)^{1/3}, \tag{3.46}$$

where $a = \mu_e m_p/m_e$. Next, we insert the expression for X into the Eq. (3.44) and obtain the equation of state in the following form

$$P_e = \frac{1}{5}\left(\frac{6}{g_e}\right)^{2/3}\frac{\pi^{4/3}\hbar^2}{m_e^{8/3}a^{5/3}}\rho_{eH}^{5/3} = \frac{1}{5}\left(\frac{6}{g_e}\right)^{2/3}\frac{\pi^{4/3}\hbar^2}{m_{eff}^{8/3}}\rho_{eH}^{5/3}, \tag{3.47}$$

where m_{eff} is the effective mass of particles associated to the white dwarf and is given by

$$m_{eff}^{8/3} = m_e^{8/3}a^{5/3}. \tag{3.48}$$

Inserting a, the last expression yields

$$m_{eff} = m_e^{3/8}\mu_e^{5/8}m_\mu^{5/8}. \tag{3.49}$$

In the case of white dwarf with α particles, $\mu_e = 2$ and the effective mass is $m_{eff} = 86.0287\ \mathrm{MeV}/c^2$. The equations that govern the structure of a white dwarf in this approximation reduce to

$$\frac{dX}{dx} = -\frac{\mu_e m_p}{m_e}\frac{(1+X^2)^{1/2}}{X}\frac{\mu}{x^2}, \tag{3.50}$$

$$\frac{d\mu}{dx} = \frac{8}{3}\frac{\mu_e m_p}{m_e}X^3x^2, \tag{3.51}$$

which, using the substitution $\Theta = (1+X^2)^{1/2}$ and $\xi = 2\times\sqrt{2}ax/\sqrt{3}$, can be cast into the nonlinear differential equation [93]

$$\frac{1}{\xi^2}\frac{d}{d\xi}\left(\xi^2\frac{d\Theta}{d\xi}\right) = -\left(\Theta^2-1\right)^{3/2}. \tag{3.52}$$

The last equation is the Chandrasekhar equation for white dwarfs. In Fig. 3.8, we present the mass radius relation obtained using the relativistic TOV equations of hydrostatic equilibrium, i.e. Eqs. (3.40) and (3.41) and the Chandrasekhar equation (3.52). We deduce that the relativistic effects on the Chandrasekhar limit are very small but play an important role for the stability of white dwarfs. Left from the OV limit, there are no stable solutions. We can then conclude that stable white dwarfs solutions can exist for radii $\gtrsim$ 1018km. For the white dwarfs solutions left from the OV limit, the electrons become highly relativistic and break up the neutrons and the process of neutronisation of matter [87] takes place. In Fig. 3.9 the mass radius relation for different objects operating at different scales is plotted. It can be seen that in the mass radius relation for white dwarfs has a specific behaviour. This is due to a strong field generated by nucleons. The region of masses from $10^6 M_\odot$ to $10^9 M_\odot$ corresponds to the supermassive compact dark objects at the galactic centers.

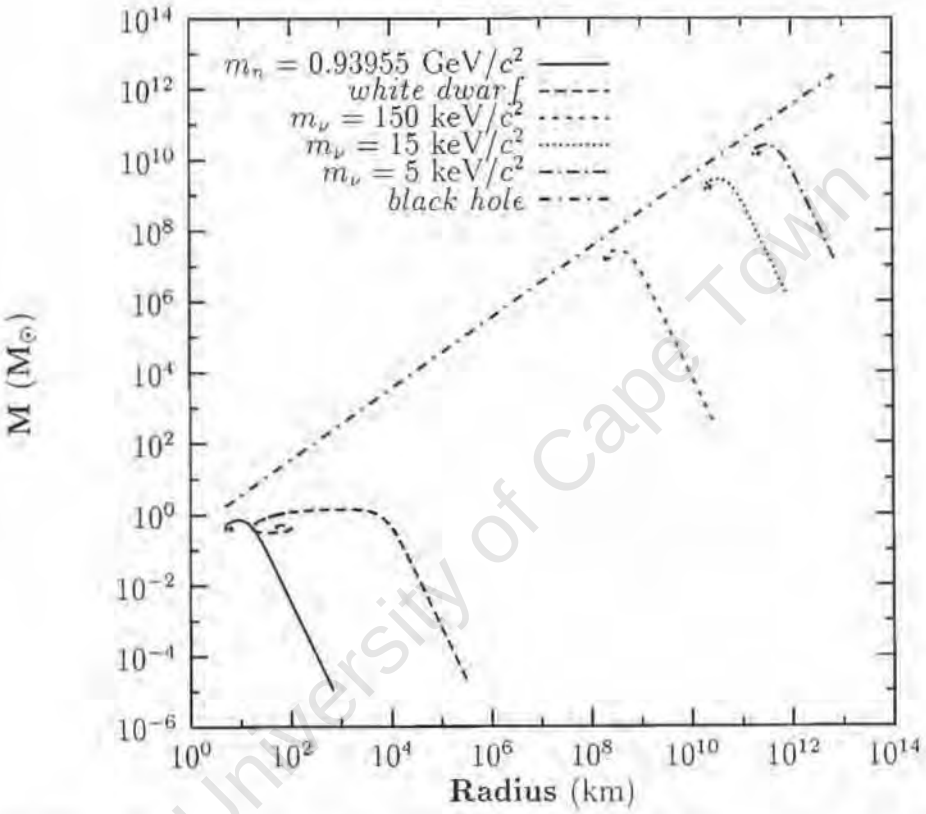

Figure 3.9: Mass radius relation of different objects compared. This plot shows how the OV limit depends on the mass of the ball constituents. The OV limit corresponding to neutron star solutions is $0.7M_\odot$. The OV limit limit for a white dwarf is almost $\sim 1.4M_\odot$. Left from the OV limit, all the solutions are unstable.

3.3 Degenerate neutrino halos around neutralino stars

We now turn to the discussion of an astrophysical system consisting of degenerate heavy-neutrino and neutralino matter that is gravitationally coupled. As each component satisfies the equation of hydrostatic equilibrium separately, i.e., Eq. (3.2) and

$$\frac{dP_n}{dr} = -\frac{1}{2}(\rho_n c^2 + P_n)\frac{d\nu}{dr}, \tag{3.53}$$

the total pressure $P = P_n + P_\nu$ and the total mass density $\rho = \rho_n + \rho_\nu$ will also obey the same equation

$$\frac{dP}{dr} = -\frac{1}{2}(\rho c^2 + P)\frac{d\nu}{dr}\,. \tag{3.54}$$

In addition to the equation of state for neutrino matter, (3.8) and (3.9), we now have the equation of state for neutralino matter

$$P_n = K_n\left[Y(1+Y^2)^{1/2}\left(\frac{2}{3}Y^2 - 1\right) + \log\left(Y + (1+Y^2)^{1/2}\right)\right], \tag{3.55}$$

$$\rho_n = \frac{K_n}{c^2}\left[Y(1+Y^2)^{1/2}(2Y^2+1) - \log\left(Y + (1+Y^2)^{1/2}\right)\right], \tag{3.56}$$

where K_n is defined by

$$K_n = K\frac{g_n}{g_\nu}\left(\frac{m_n}{m_\nu}\right)^4, \tag{3.57}$$

g_n is the spin-degeneracy factor for neutralinos and antineutralinos and K is given by Eq. (3.11). In the Eqs. (3.55) and (3.56), Y stands for the local Fermi momentum of neutralino matter (in units of $m_n c$). Inserting (3.55) and (3.56) into (3.53), after integration we arrive at

$$Y = [(1+Y_0^2)e^{\nu(0)-\nu(r)} - 1]^{1/2}\,, \tag{3.58}$$

with $Y_0 = Y(0)$. Using (3.8), (3.9), and the equation of hydrostatic equilibrium (3.2), a similar relation for the Fermi momentum of neutrinos (in units of $m_\nu c$) is obtained

$$X = [(1+X_0^2)e^{\nu(0)-\nu(r)} - 1]^{1/2}. \tag{3.59}$$

Combining (3.58) and (3.59), the two local Fermi momenta are related by

$$X^2 = \frac{(X_0^2+1)Y^2 + X_0^2 - Y_0^2}{1+Y_0^2}. \tag{3.60}$$

The condition $X^2 \geq 0$ restricts the range of allowed values of Y to

$$Y^2 \geq \frac{Y_0^2 - X_0^2}{1 + X_0^2} \,. \tag{3.61}$$

The total pressure and mass density is given by

$$P(Y) = P_n(Y) + P_\nu(X(Y)) \tag{3.62}$$

and

$$\rho(Y) = \rho_n(Y) + \rho_\nu(X(Y)), \tag{3.63}$$

respectively.

We now formulate the coupled differential equations describing a gravitationally interacting system of degenerate heavy-neutrino and neutralino matter. We first keep the mass of the neutrino halo constant while varying the mass of the neutralino star. Introducing the dimensionless variables $x = r/a_n$ and $\mu = m/b_n$ with the scales

$$a_n = \frac{2}{m_n^2}\left(\frac{\pi\hbar^3}{g_n c G}\right)^{1/2} \quad \text{and} \quad b_n = \frac{2}{m_n^2}\left(\frac{\pi\hbar^3 c^3}{g_n G^3}\right)^{1/2}, \tag{3.64}$$

the relevant TOV equations can be written in the form

$$\begin{aligned}\frac{dY}{dx} &= -\frac{+Y^2}{Y(x^2 - 2\mu x)}\Big\{\mu + x^3\Big[Y(1+Y^2)^{1/2}\left(\frac{2}{3}Y^2 - 1\right) \\ &\quad + \log\left(Y + (1+Y^2)^{1/2}\right) + \left(\frac{m_\nu}{m_n}\right)^4 \frac{g_\nu}{g_n}\Big(X(1+X^2)^{1/2}\left(\frac{2}{3}X^2 - 1\right) \\ &\quad + \log\left(X + (1+X^2)^{1/2}\right)\Big)\Big]\Big\},\end{aligned} \tag{3.65}$$

$$\begin{aligned}\frac{d\mu}{dx} &= x^2\Big\{Y(1+Y^2)^{1/2}(2Y^2+1) - \log\left(Y + (1+Y^2)^{1/2}\right) + \left(\frac{m_\nu}{m_n}\right)^4 \frac{g_\nu}{g_n} \\ &\quad \times \Big[X(1+X^2)^{1/2}(2X^2+1) - \log\left(X + (1+X^2)^{1/2}\right)\Big]\Big\}\,,\end{aligned} \tag{3.66}$$

where X is related to Y through (3.60). If the condition (3.61) is not fulfilled, i.e., the neutrino pressure and density have already vanished, the system is solved with the Y terms describing the neutralinos only.

In order to solve Eqs. (3.65) and (3.66) numerically, we fix the Fermi momentum of neutrinos (in units of $m_\nu c$) at the center and vary the central values of the corresponding quantity Y_0 for neutralinos. The total mass (including neutrinos and neutralinos) enclosed within the radius R_n of the neutralino star is shown in Fig. 3.10. Here, the neutrino mass and the degeneracy factor are taken to be $m_\nu = 17.2\ \mathrm{keV}/c^2$ and $g_\nu = 2$, respectively, while

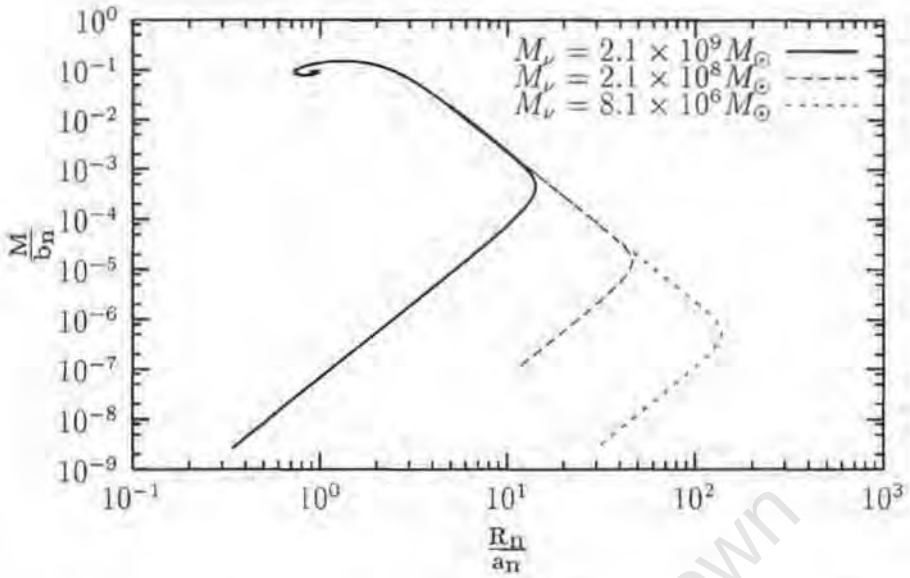

Figure 3.10: The total mass (including neutralinos and neutrinos) M enclosed within the radius R_n of the neutralino star for various masses M_ν of the neutrino halo. The maximal radius of the neutralino star decreases with increasing M_ν.

for the neutralino mass we have chosen $m_n = 939.55$ MeV$/c^2$ and $g_n = 2$, with the scales $a_n = 6.8304$ km and $b_n = 4.6257\ M_\odot$. For small neutralino-star masses, the total mass enclosed in R_n scales as R_n^3, corresponding to a constant density governed by the gravitational potential of the surrounding supermassive neutrino halo. However, as the radius of the neutralino star approaches that of a "free" neutralino star, the gravitational potential of the neutralino star becomes dominant and the mass now scales as R_n^{-3} up to the OV limit. Thus there is always a maximal radius of a neutralino star within a neutrino halo of a given mass. Substituting neutralinos by neutrons, we must take care of the fact that (i) the neutron interacts strongly in the nuclear medium (simulated, e.g., by an effective mass) and (ii) the neutron decays through weak interactions. Thus, stable neutron stars can exist only in the range from 0.2 $M_\odot$ to 2 $M_\odot$ [96], where the average binding energy is larger than the Q value for the neutron decay.

It is instructive to study the properties of a degenerate gas of neutralinos and neutrinos in the nonrelativistic approximation. In the limits $X \ll 1$ and $Y \ll 1$, (3.65) and (3.66) simplify to

$$\frac{dY}{dx} = -\frac{\mu}{x^2 Y}, \tag{3.67}$$

$$\frac{d\mu}{dx} = \frac{8}{3} x^2 [Y^3 + \frac{g_\nu}{g_n} \left(\frac{m_\nu}{m_n}\right)^4 (Y^2 + X_0^2 - Y_0^2)^{3/2}] , \tag{3.68}$$

with the boundary conditions

$$\mu(0) = 0; \quad Y^2 \geq Y_0^2 - X_0^2; \quad Y(0) = Y_0 \ . \tag{3.69}$$

This system of equations can be rewritten in the form of a Lané-Emden type equation by introducing $\Theta_n = Y^2$, $\Theta_\nu = X^2$, and a new dimensionless radial variable $\xi = 4x/\sqrt{3}$

$$\frac{1}{\xi^2}\frac{d}{d\xi}\left(\xi^2\frac{d\Theta_n}{d\xi}\right) = -[\Theta_n^{3/2} + \frac{g_\nu}{g_n}\left(\frac{m_\nu}{m_n}\right)^4(\Theta_n + \Theta_{\nu 0} - \Theta_{n0})^{3/2}] \ , \tag{3.70}$$

where Θ_{n0} and $\Theta_{\nu 0}$ are the central values of the neutralino and neutrino densities, respectively. For very small neutralino densities, i.e. $Y \ll 1$ and $Y_0 \ll 1$, the mass equation (3.68) can be integrated to give

$$\mu(x) = \frac{8}{9}\left(\frac{m_\nu}{m_n}\right)^4 X_0^3 x^3 \ , \tag{3.71}$$

which confirms the conclusion drawn in the context of Fig. 3.10.

We now turn to the case of a neutralino star of constant mass surrounded by a neutrino halo of variable mass. The TOV equations written in terms of the functions X and μ may be obtained from (3.65) and (3.66), in which we make the replacements $X \leftrightarrow Y$, $g_\nu \leftrightarrow g_n$, and $m_\nu \leftrightarrow m_n$. Thus, we find

$$\begin{aligned}\frac{dX}{dx} &= -\frac{1+X^2}{X(x^2-2\mu x)}\Big\{\mu + x^3\Big[X(1+X^2)^{1/2}\left(\frac{2}{3}X^2 - 1\right) \\ &\quad + \log\left(X + (1+X^2)^{1/2}\right) + \left(\frac{m_n}{m_\nu}\right)^4\frac{g_n}{g_\nu}\Big(Y(1+Y^2)^{1/2}\left(\frac{2}{3}Y^2 - 1\right) \\ &\quad + \log\left(Y + (1+Y^2)^{1/2}\right)\Big)\Big]\Big\}, \end{aligned} \tag{3.72}$$

$$\begin{aligned}\frac{d\mu}{dx} &= x^2\Big\{X(1+X^2)^{1/2}(2X^2+1) - \log\left(X + (1+X^2)^{1/2}\right) + \left(\frac{m_n}{m_\nu}\right)^4\frac{g_n}{g_\nu} \\ &\quad \times\left[Y(1+Y^2)^{1/2}(2Y^2+1) - \log\left(Y + (1+Y^2)^{1/2}\right)\right]\Big\} \ , \end{aligned} \tag{3.73}$$

with X and Y subject to the condition

$$X^2 \geq \frac{X_0^2 - Y_0^2}{1 + Y_0^2} \ . \tag{3.74}$$

If this condition is not satisfied, i.e., the pressure and density of neutralinos have already vanished, (3.72) and (3.73) are solved without the Y terms, i.e., for neutrinos only. Choosing the OV limit as the mass of the neutralino star, i.e., $M_{\rm OV}^n = 0.7091\ M_\odot$ for $m_n = 0.93955\ {\rm GeV}/c^2$ and $g_n = 2$, and varying

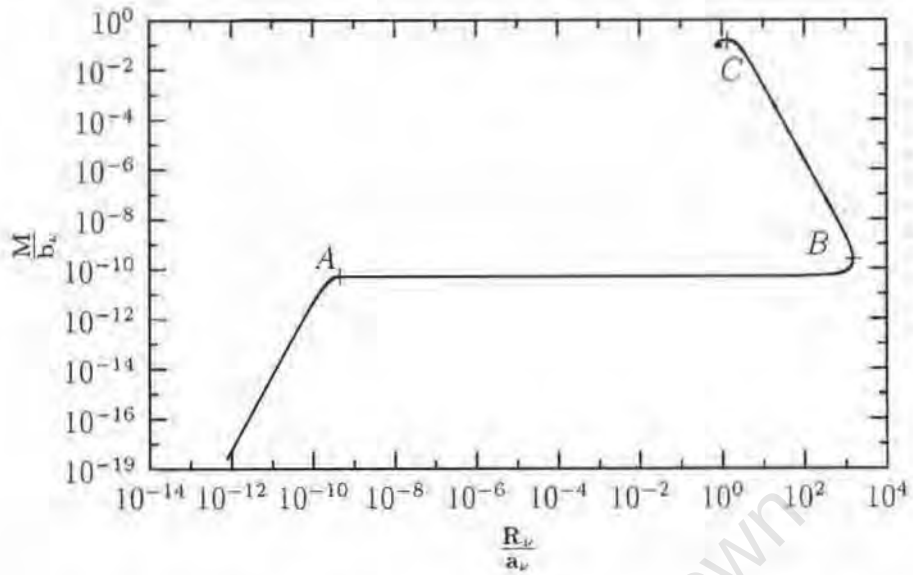

Figure 3.11: The total mass of neutralinos and neutrinos M contained within the radius R_ν of the neutrino halo around a neutralino star. The plateau between the points A and B reflects the fact that the neutralino part, which is saturated at the point A, dominates the total mass up to the turning point B. C represents the OV-limit.

the central Fermi momentum X_0, one can find the total mass (including neutralinos and neutrinos) as a function of the radius R_ν of the neutrino halo. This scenario is reflected in Fig. 3.11, where the length and mass scales are $a_\nu = 2.0381 \times 10^{10}$ km and $b_\nu = 1.3803 \times 10^{10}\ M_\odot$, respectively.

Here the neutrino mass and the degeneracy factor have been chosen as $m_\nu = 17.2$ keV$/c^2$ and $g_\nu = 2$, respectively. At the turning point A, the total mass enclosed within the radius $R_A = R^n_{\rm OV} = 9.1816$ km of the neutrino halo is $M_A = M^n_{\rm OV} = 0.7091\ M_\odot$. At the turning point B, the total mass enclosed within the radius $R_B = 0.9912$ pc of the neutrino halo is $M_B = 3.3453\ M_\odot$. It is interesting to note that, also in this case, there is a maximal radius R_B of the neutrino halo, for a given mass of the neutralino star.

Replacing the neutralino star by a baryonic star, such as a neutron star, a white dwarf, or an ordinary star, the only things that will change in Fig. 3.11 are the points A and B depending, of course, on the mass M_n of the central object as we will see below.

3.4 Degenerate neutrino halos around white dwarfs

Let us formulate a system of differential equations, that describe a white dwarf surrounded by a neutrino halo in a general relativistic context. The equation of state of neutrinos is given by Eq. (3.8) and (3.9) while that of the white dwarf is given by Eq. (3.37) and (3.38). As each component satisfies the equation of hydrostatic equilibrium separately, i.e. Eq. (3.2) and

$$\frac{dP_\nu}{dr} = -\frac{1}{2}(\rho_\nu c^2 + P_\nu)\frac{d\nu}{dr}, \tag{3.75}$$

$$\frac{dP_e}{dr} = -\frac{1}{2}(\rho_{eH} c^2 + P_e)\frac{d\nu}{dr}, \tag{3.76}$$

the total pressure $P = P_\nu + P_e$ and the total mass density $\rho = \rho_\nu + \rho_{eH}$ will also obey the same equation

$$\frac{dP}{dr} = -\frac{1}{2}(\rho c^2 + P)\frac{d\nu}{dr}. \tag{3.77}$$

Inserting (3.8) and (3.9) into (3.75), after integration, we get

$$e^{\nu(0)-\nu(r)} = \frac{1+X^2}{1+X_0^2} \tag{3.78}$$

Using the equation of state for the white dwarf, i.e. Eq. (3.37) and (3.38) and the equation of hydrostatic equilibrium (3.76) we arrive at a similar relation between the potential ν and the Fermi momentum Y (in units of $m_e c$) of electrons

$$e^{\nu(0)-\nu(r)} = \left(\frac{a+(1+Y^2)^{1/2}}{a+(1+Y_0^2)^{1/2}}\right)^2, \tag{3.79}$$

where the constant $a = \mu_e m_p/m_e$, μ_e being the molecular weight per electron and m_e and m_p are the electron and proton masses, respectively. Next, we equate the right sides of equations (3.78) and (3.79) to find the relation between the two Fermi momenta of electrons and neutrinos. After some algebraic manipulations, we get

$$X^2 = \left(1+X_0^2\right)\left[\frac{a+(1+Y^2)^{1/2}}{a+(1+Y_0^2)^{1/2}}\right]^2 - 1. \tag{3.80}$$

Here, the parameter X_0 is the neutrino Fermi momentum in units of $m_\nu c$ at the center of the neutrino ball and Y_0 stands for the central value of electrons Fermi momentum in units of $m_e c$. The condition X^2 will restrict the neutrino pressure to be negative.

The total pressure and mass density of electrons and the white dwarf are given by

$$P(Y) = P_e(Y) + P_\nu(X(Y)), \tag{3.81}$$

$$\rho(Y) = \rho_{eH}(Y) + \rho_\nu(X(Y)), \tag{3.82}$$

respectively. We can now formulate a set of two coupled differential equations that describe a system of a heavy neutrino matter and a white dwarf that interact gravitationally

$$\begin{aligned}\frac{dY}{dx} &= -\frac{(1+Y^2)^{1/2}\left(a+(1+Y^2)^{1/2}\right)}{Y(x^2-2\mu x)}\Big\{\mu + x^3\Big[Y(1+Y^2)^{1/2}\left(\frac{2}{3}Y^2-1\right)\\ &+\log\left(Y+(1+Y^2)^{1/2}\right)+\left(\frac{m_\nu}{m_e}\right)^4\frac{g_\nu}{g_e}\Big(X(1+X^2)^{1/2}\left(\frac{2}{3}X^2-1\right)\\ &+\log\left(X+(1+X^2)^{1/2}\right)\Big)\Big]\Big\}.\end{aligned} \tag{3.83}$$

$$\begin{aligned}\frac{d\mu}{dx} &= x^2\Big\{\frac{8}{3}aY^3+Y\left(1+Y^2\right)^{1/2}(2Y^2+1)-\log\left(Y+(1+Y^2)^{1/2}\right)\\ &+\left(\frac{m_\nu}{m_e}\right)^4\frac{g_\nu}{g_e}\Big[X(1+X^2)^{1/2}(2X^2+1)\\ &-\log\left(X+(1+X^2)^{1/2}\right)\Big]\Big\},\end{aligned} \tag{3.84}$$

where the function X is related to Y through the relation (3.80). Here, x and μ are the normalized radius and mass scales respectively, i.e. $x = r/a_e$ and $\mu = m(r)/b_e$. The scales a_e and b_e are defined respectively by Eq. (3.42) and (3.43). To solve the equations (3.83) and (3.84) , we fix the Fermi momentum of neutrinos, i.e. the parameter X_0 at the center and vary the electrons Fermi momentum, i.e. Y_0 at the center. The total mass of the neutrinos and white dwarf enclosed within a radius R_{wd} of the white dwarf is shown in Fig. 3.12. In this plot the neutrino mass $m_\nu c^2 = 17.2$ keV, the spin degeneracy factors g_ν and g_e are taken to be two. From Fig.3.12, one can see that the total mass enclosed within a radius R_{wd} scales as R_{wd}^3, corresponding to a constant distribution governed by the gravitational potential of surrounding supermassive neutrino halo. As the radius R_{wd} approaches that of a free white dwarf, the gravitational potential of the white dwarf becomes more important and the mass now scales as R_{wd}^{-3}. The maximum corresponds to the OV limit.

Let us turn to the case of a white dwarf of fixed mass surrounded by a neutrino halo of variable mass. To do this, we express the electrons Fermi momentum momentum as a function of the neutrino Fermi momentum:

$$Y^2 = \left(a+(1+Y_0^2)^{1/2}\right)\left(\frac{1+X^2}{1+X_0^2}\right)^{1/2} - 1, \tag{3.85}$$

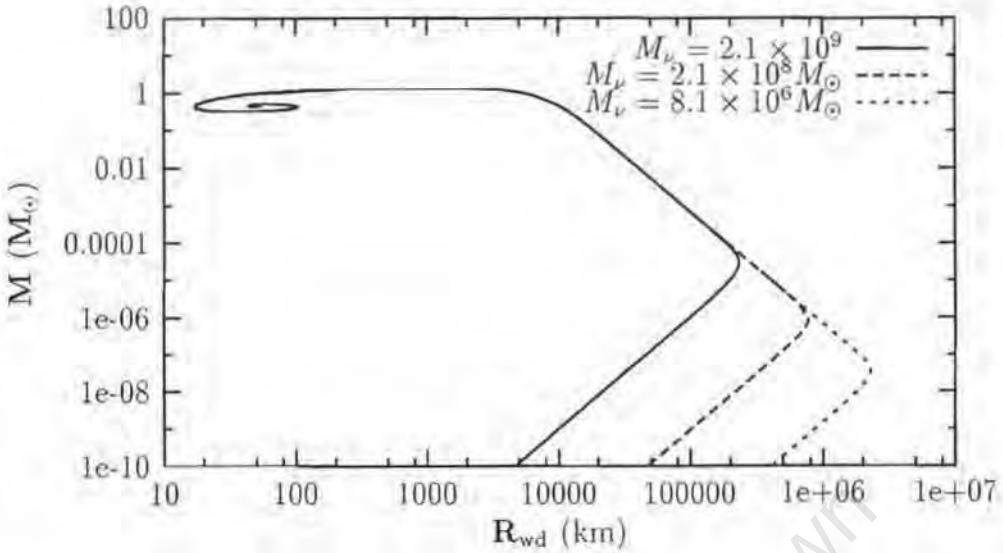

Figure 3.12: The total mass (including the white dwarf and neutrinos) M enclosed with a radius R_{wd} of the white dwarf for various masses M_ν of the neutrino halo. The maximal radius of the white dwarf decreases with increasing M_ν.

and $Y^2 \geq 0$. We can now formulate the set of equations that describe a neutrino halo of variable mass surrounding a white dwarf of constant mass

$$\begin{aligned}\frac{dX}{dx} &= -\frac{1+X^2}{X(x^2-2\mu x)}\Big\{\mu + x^3\Big[X(1+X^2)^{1/2}\left(\frac{2}{3}X^2-1\right)\\ &+\log\left(X+(1+X^2)^{1/2}\right)+\left(\frac{m_e}{m_\nu}\right)^4\frac{g_e}{g_\nu}\Big(Y(1+Y^2)^{1/2}\left(\frac{2}{3}Y^2-1\right)\\ &+\log\left(Y+(1+Y^2)^{1/2}\right)\Big)\Big]\Big\}. \qquad (3.86)\end{aligned}$$

$$\begin{aligned}\frac{d\mu}{dx} &= x^2\Big\{X(1+X^2)^{1/2}(2X^2+1)-\log\left(X+(1+X^2)^{1/2}\right)\\ &+\left(\frac{m_e}{m_\nu}\right)^4\frac{g_e}{g_\nu}\left[Y(1+Y^2)^{1/2}(2Y^2+1)-\log\left(Y+(1+Y^2)^{1/2}\right)\right]\\ &+\frac{8}{3}a\left(\frac{m_e}{m_\nu}\right)^4\frac{g_e}{g_\nu}Y^3\Big\}, \qquad (3.87)\end{aligned}$$

with the condition that $Y^2 \geq 0$. If this condition is not satisfied, i.e. the pressure and density of white-dwarf (WD) have already vanished, Eqs. (3.86) and (3.87) are solved without the Y terms, i.e. for neutrinos only. Here, $a = \mu_e m_p/m_e$, $x = r/a_\nu$ and $\mu = m(r)/b_\nu$. The length and mass scales a_ν and b_ν are given by Eqs. (3.12) and (3.13), respectively. We have numerically

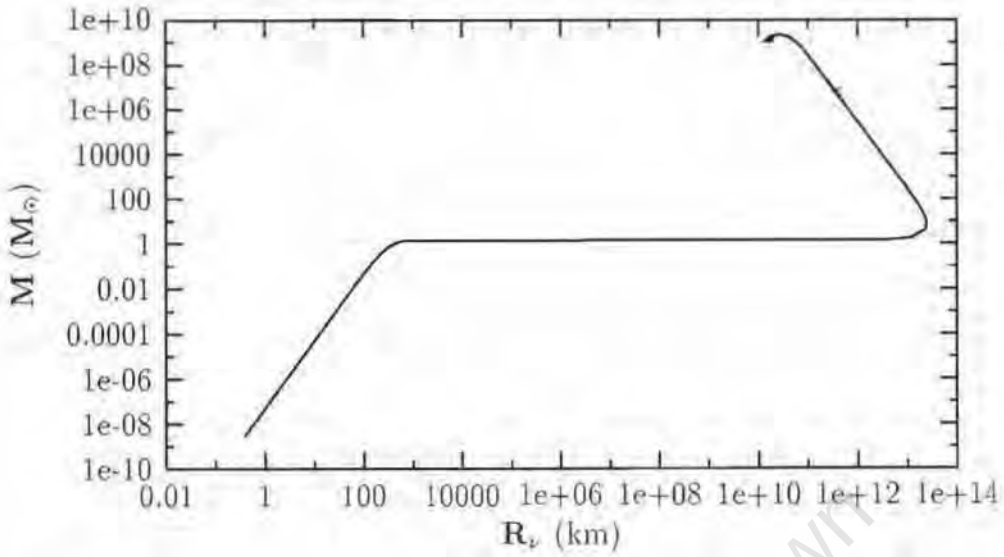

Figure 3.13: Total mass of neutrinos and white dwarf matter contained within a radius R_ν of the neutrino halo around a white dwarf. The total mass increases up to the radius of the white dwarf, then becomes constant and finally starts increasing as the gravitational potential of the neutrinos starts dominating over the white dwarf.

integrated the system of Eqs. (3.86) and (3.87) and the total mass M of neutrinos and white dwarf matter is plotted against the radius R_ν of the neutrino ball in Fig. 3.13. In this plot, the mass of the white dwarf has been chosen as 1.4 $M_\odot$ with a radius of 1018 km. The neutrino mass is chosen to be 17.2 keV/c^2. The spin degeneracy factors $g_\nu = g_e = 2$. From Fig. 3.13, we note that the neutrino halo has a maximal radius which of course depends on the mass of the compact object at the center, in this case the white dwarf.

3.5 Escape and circular velocities

Using the results from sections (3.3) and (3.4), we now turn to the study of the escape and circular velocities of matter falling onto a neutrino ball with a compact object at its center. We take a neutron star and a white dwarf as examples of compact objects. For simplicity, we assume the mass of the neutron star and the white dwarf to have a value of 1.4 $M_\odot$, which is the Oppenheimer-Volkoff limit for a white dwarf. We note here that the Chandrasekhar limit and the Oppenheimer-Volkoff limit for a white dwarf are almost the same as shown in section 3.2. Let us choose the effective neutron mass so that the Oppenheimer-Volkoff limit of the neutron star solutions is

1.4 $M_\odot$, i.e.

$$M_{OV} = 2.9924 \times 10^9 M_\odot \left(\frac{17.2 \text{ keV}}{m_n c^2}\right)^2 g_\nu^{-1/2} = 1.4\ M_\odot. \tag{3.88}$$

Solving for m_n, the effective neutron mass is found to be $m_n = 668.6775$ MeV/c^2 and the neutron star will have at the OV limit a size of $\sim$ 18 km . Here, we recall that a neutrino halo with a fixed neutron star mass is described by the system of equations (3.72) and (3.73) while a neutrino halo with a white dwarf can be characterized by the two coupled differential equations (3.86) and (3.87). By requiring the continuity of the interior and the exterior solutions at the boundary x_0 of the neutrino ball, one can express the metric functions ν and λ in terms of X and μ as follows:

$$e^{\nu} = \begin{cases} (1 - 2\mu_0/x_0)\dfrac{1}{1+X^2} & x \leq x_0 \\ (1 - 2\mu_o/x) & x > x_0, \end{cases} \tag{3.89}$$

$$e^{\lambda} = \begin{cases} \left(1 - \dfrac{2\mu}{x}\right)^{-1} & x \leq x_0 \\ \left(1 - \dfrac{2\mu_0}{x}\right)^{-1} & x > x_0, \end{cases} \tag{3.90}$$

where μ_0 is the total mass of neutrinos and neutrons at a radius x_0. For particles accreting onto the neutrino ball with a neutron star at the center, the circular velocity v_c can be expressed as [84]

$$\begin{aligned} \frac{v_c}{c} &= \left(\frac{re^{\nu}\nu'}{2}\right)^{1/2} \\ &= \frac{1}{1+X^2}\left[-x\left(1 - \frac{2\mu_0}{x_0}\right)XX'\right]^{1/2}, \end{aligned} \tag{3.91}$$

while the escape velocity v_e has the following form

$$\begin{aligned} \frac{v_e}{c} &= e^{\frac{\nu-\lambda}{2}}(-e^{\nu}+1)^{1/2} \\ &= \frac{1}{1+X^2}\left[\left(1 - \frac{2\mu_0}{x_0}\right)\left(1 - \frac{2\mu}{x}\right)\left(\frac{2\mu_0}{x_0} + X^2\right)\right]^{1/2}. \end{aligned} \tag{3.92}$$

Here, μ_0 and x_0 are the total mass of the halo and the the radius of the neutrino ball, respectively. X is the Fermi-momentum of neutrinos, and μ stands for the mass enclosed within a radius x and satisfy the system of Eqs. (3.72) and (3.73). In the case of a halo with a white dwarf, the same equations apply, the only difference is that X and μ will satisfy the system of equations (3.86) and (3.87). The density of neutrons Y_0 and the density of neutrinos X_0 are chosen so that the mass of the neutron star is 1.4 $M_\odot$

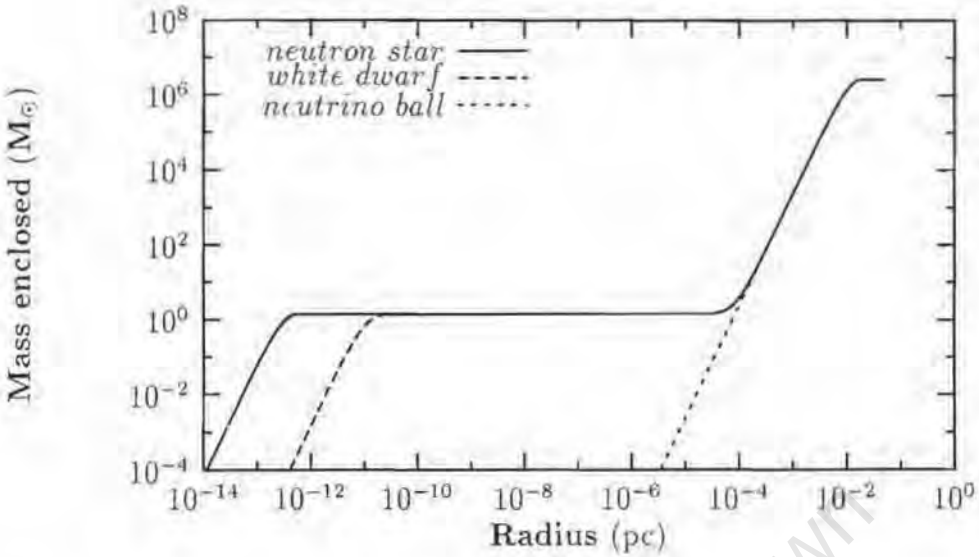

Figure 3.14: Mass enclosed as a function of the radius for different scenarios: 1) a neutron star surrounded by a neutrino ball; 2) a white dwarf surrounded by a neutrino ball; 3) a pure neutrino ball. The neutron star and the white dwarf have the same mass of 1.4 $M_\odot$. The neutrino ball has a mass of 2.6×10^6 $M_\odot$.

and the total mass of neutrons and neutrinos is $2.6 \times 10^6 M_\odot$. The neutrino mass has been taken to be 15.92 keV/c^2 and the radius of the neutrino ball is 1.88×10^{-2}pc.

In Fig. 3.14, the mass enclosed in a neutrino ball with a compact star at the center is plotted as a function of the distance from the center for three scenarios:i) a neutrino halo around a neutron star; ii)a neutrino halo around a white dwarf; iii) a neutrino halo only. The neutron star and the white dwarf have the same mass of 1.4 $M_\odot$. The total mass of the neutrino ball and the compact star is $M = 2.6 \times 10^6 M_\odot$. The circular and escape velocities of accreting matter onto a neutron star surrounded by a neutrino halo are shown in Figs. 3.15 and 3.16, respectively. It can be seen from Fig. 3.16, that the baryonic matter falling onto a neutron star must have an escape velocity of about a half the velocity of light in order to escape from the center.

3.6 Neutrino ball in a constant density background

We follow the method developed in the previous sections to investigate the equilibrium configurations of the two component gas consisting of baryonic matter of constant density and neutrinos. Baryonic matter and neutrinos will

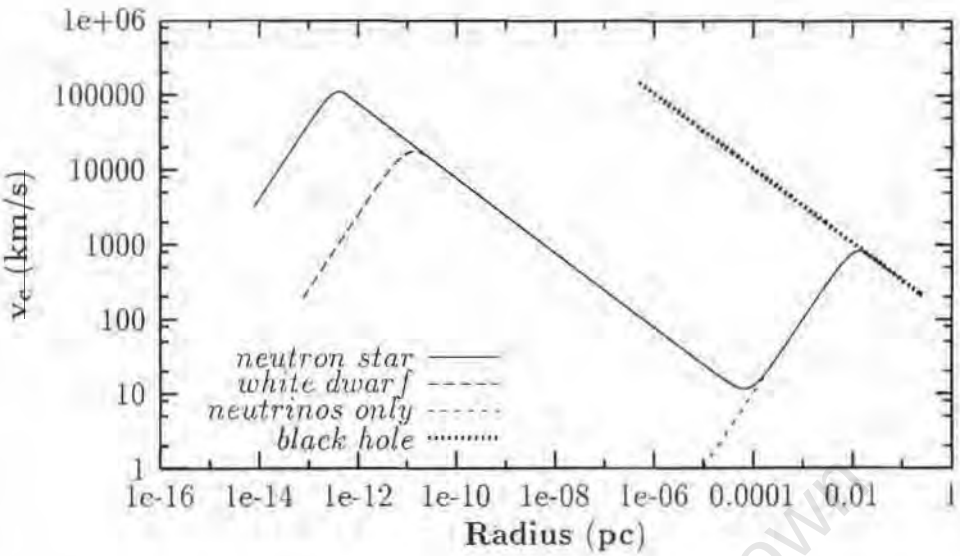

Figure 3.15: Circular velocity of accreting matter as a function of the radius for different scenarios as labelled on the graph. The neutron star and the white dwarf have a mass of 1.4 $M_\odot$. The circular velocity corresponding to a black hole of $2.6 \times 10^6 M_\odot$ has also been included.

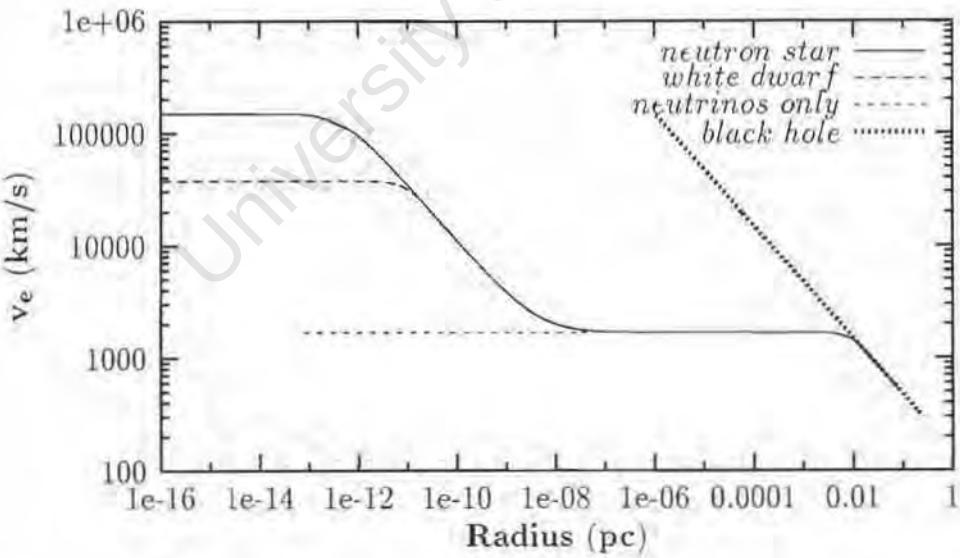

Figure 3.16: Escape velocity of accreting matter as a function of the radius for different scenarios. The neutron star and the white dwarf have the same mass of 1.4 $M_\odot$. The neutrino ball has a mass of 2.6×10^6 $M_\odot$. The escape velocity corresponding to a black hole of $2.6 \times 10^6 M_\odot$ has also been included.

interact only gravitationally through the potential $\nu(r)$. Each component thus should satisfy equation (3.2)

$$\frac{dP_B}{dr} = -\frac{1}{2}\left(\rho_B c^2 + P_B\right)\frac{d\nu}{dr}\,, \tag{3.93}$$

$$\frac{dP_\nu}{dr} = -\frac{1}{2}\left(\rho_\nu c^2 + P_\nu\right)\frac{d\nu}{dr}. \tag{3.94}$$

The indices B and ν denote baryons and neutrinos. respectively. We will assume that the density of the baryonic matter is constant $\rho_B = \rho_0$. By integrating the equation (3.93), we find the relation between the baryonic pressure and the gravitational potential

$$P_B = \rho_0 c^2\left(e^{\frac{\nu(0)-\nu(r)}{2}} - 1\right) + P_B(0)e^{\frac{\nu(0)-\nu(r)}{2}}\,. \tag{3.95}$$

Here $P_B(0)$ is the initial value of the baryonic pressure at the the center of the gas sphere of neutrinos and baryons. We adopt the relativistic equation of state of a cold Fermi gas for neutrinos as given by equations (3.8) and (3.9). The function X is related to the potential ν through the relation (3.78). Next, we use that relation to express the baryonic pressure P_B in terms of the function X. By choosing the initial values of the pressure $P_B(0)$ to be $\rho_0 c^2$, the baryonic pressure has therefore the following form

$$P_B(r) = \left(2\left[\frac{1+X^2(r)}{1+X_0^2}\right]^{1/2} - 1\right)\rho_0 c^2\,. \tag{3.96}$$

From the condition that the baryonic pressure should be positive, we deduce that

$$X^2 \geq \frac{X_0^2 - 3}{4}\,. \tag{3.97}$$

To establish the mass-radius relation for a system of neutrinos and baryonic matter, we have integrated numerically the TOV equations (3.1) and (3.5) in which

$$P_{\rm total} = P_\nu + P_B,\ \rho_{\rm total} = \rho_\nu + \rho_B = \rho_\nu + \rho_0\,. \tag{3.98}$$

Introducing dimensionless variables $x = r/a_\nu$ and $\mu = m(r)/b_\nu$ as previously, and choosing $\rho_0 = \beta b_\nu/(4\pi a_\nu^3)$, the baryonic mass M_B is given in terms of x as

$$M_B = \beta x^3 b_\nu/3\,. \tag{3.99}$$

A two component system of neutrinos and a constant density baryonic matter will then be described by the following set of equations:

$$\begin{aligned}\frac{dX}{dx} &= -\frac{1+X^2}{X(x^2-2\mu x)}\Big\{\mu + x^3\Big[X(1+X^2)^{1/2}(2X^2/3-1) + \\ &\log\left(X+(1+X^2)^{1/2}\right) + \beta\left(2\left[\frac{1+X^2}{1+X_0^2}\right]^{1/2} - 1\right)\Big]\Big\}\end{aligned} \tag{3.100}$$

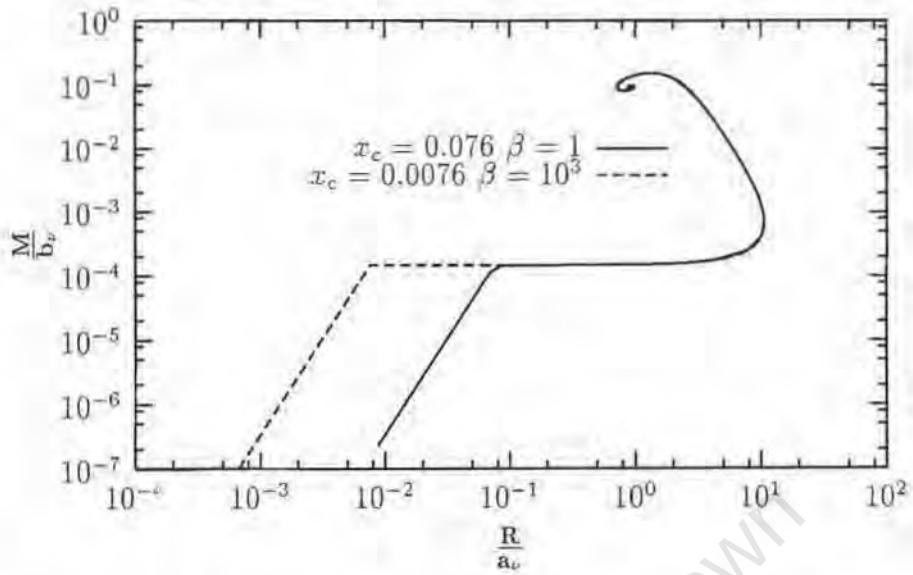

Figure 3.17: Total Mass of neutrinos and baryons within the radius R_ν of the neutrino ball. The mass of the baryonic star is fixed as shown on the graph.

$$\frac{d\mu}{dx} = \beta x^2 + x^2\left[X(1+X^2)^{1/2}(2X^2+1) - \log(X+(1+X^2)^{1/2})\right] \ , \quad (3.101)$$

subject to the conditions

$$\mu(0) = 0; \quad X(0) = X_0; \quad X^2 \geq \frac{X_0^2 - 3}{4} \ . \quad (3.102)$$

In case the last inequality is not satisfied, which means that the boundary of the baryonic star has been reached, the above system of equations is solved only for neutrinos. Fig. 3.17 shows the mass-radius relation for such an astrophysical system. The baryonic mass is fixed to $2 \times 10^6\ M_\odot$, the neutrino mass is 17.2 keV/c^2, the parameter β and the core radius x_c have been varied. The unit of length $a_\nu = 2.0381 \times 10^{10}$ km and the unit of mass $b_\nu = 1.3803 \times 10^{10}\ M_\odot$. Fig. 3.18 shows the mass versus radius for neutrinos in a constant density background. The parameters a_ν and b_ν are defined as in equations (3.12) and (3.13). The parameter β is 1 and the mass of the baryonic star is not fixed. Similar dependence of the mass on the radius has been found in strange quark stars [97].

We now turn to the case of a neutrino gas coupled to a constant density baryonic matter in the Newtonian limit. To investigate this scenario, we write the system of Eqs. (3.100) and (3.101) for small Fermi momenta of neutrinos, i.e. for $X \ll 1$, the pressure of baryons is neglected

$$\frac{dX}{dx} = -\frac{\mu}{x^2 X} \quad (3.103)$$

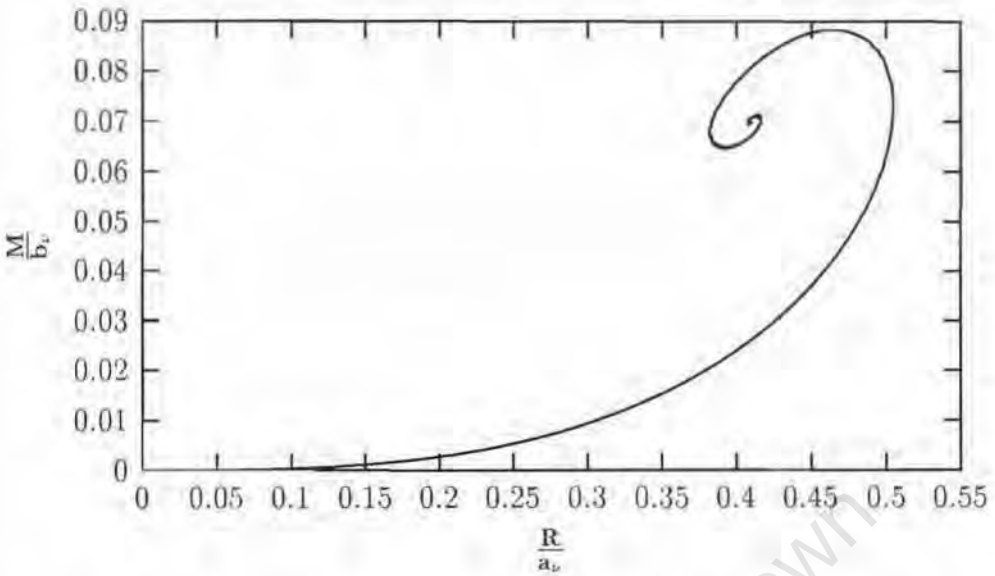

Figure 3.18: Total Mass versus radius for neutrinos in a constant density background. The mass of the baryonic star is not fixed.

$$\frac{d\mu}{dx} = x^2\left(\beta + \frac{8X^3}{3}\right). \tag{3.104}$$

This system of equations can be written as a modified Lané-Emden differential equation [93]

$$\frac{1}{\xi^2}\frac{d}{d\xi}\left(\xi^2\frac{d\Theta}{d\xi}\right) = -(\Theta^{3/2} + 3/8\beta) \tag{3.105}$$

where the function Θ has been defined as $\Theta = X^2$ and $\xi = 1x/\sqrt{3}$.

3.7 Conclusion

We have studied degenerate fermion balls, consisting of massive neutrinos or neutralinos, or both. We have shown that the existence of such objects may have important astrophysical implications. For neutrinos masses in the range of 10 to 25 keV the Oppenheimer-Volkoff limit is of the order of a few times $10^9 M_\odot$ which is the upper limit for the supermassive dark objects at the center of a number of galaxies and thus neutrino balls are natural candidates for the supermassive dark objects. We have shown that a neutrino ball at the Oppenheimer-Volkoff limit differs slightly from a black hole of the same mass. The radius of a neutrino ball at the OV limit is $R_\nu = 4.4466\ R_S$, where R_S the Schwarzschild radius corresponding to the mass M_{OV}. Assuming that the most massive object, such as the compact dark object at the center of

M87, is a neutrino ball at the OV limit, we have established the constraints on the neutrino mass to be 12.1 keV/$c^2 \leq m_\nu \leq$ 16.5 keV/c^2 for $g_\nu = 2$ and 10.4 keV/$c^2 \leq m_\nu \leq$ 13.9 keV/c^2 for $g_\nu = 4$. Furthermore, interpreting the supermassive dark object at the center of our Galaxy as a neutrino ball, we obtain from the upper limit of the size of this object, the lower bounds on the neutrino mass $m_\nu \geq 15.92$ keV/c^2 for $g_\nu = 2$ and $m_\nu \geq 13.39$ keV/c^2 for $g_\nu = 4$. Here, we point out that the supermassive dark object at the center of our Galaxy could be a neutrino ball (extended object) rather than a black hole.

By studying a two-component system consisting of neutralinos in the GeV mass range or white dwarf matter or a baryonic matter and neutrinos, we have found that there is always a maximal mass and radius of the compact star within a neutrino halo of a given mass. For a fixed mass of the compact star, the neutrino halo will always have a maximum radius which depends obviously on the mass of the compact object. Besides that, the neutrino halo will have a maximum mass that corresponds to the Oppenheimer-Volkoff limit for the chosen neutrino mass.

For an astrophysical system consisting of a neutrino ball with a compact star at its center, we have established the escape and circular velocities for the falling matter onto the system and have found that the escape velocity from the center of the neutron star can go up to a half the velocity of light.

Owing to their compactness, neutralino stars could mimic the properties of "machos" for neutralino masses between 1.22 MeV and 1.25 GeV.

Chapter 4

The compact supermassive dark object at the Galactic center

4.1 Status of the supermassive object at the Galactic center

The determination of the mass distribution near the center of our Galaxy and the question, whether it harbours a supermassive black hole (BH) or not, have been long-standing issues [26, 54, 98, 99]. Various techniques have been used to find the mass of this supermassive compact dark object which is usually identified with the radio source Sagittarius A* (Sgr A*) at or near the Galactic center. The most detailed information to date comes from the study of the dynamics of stars moving in the gravitational field of the central mass distribution [27, 28, 61, 66, 67, 68, 100, 101, 102, 103, 104]. It has been established that the central dark object has a mass of $(2.61 \pm 0.76) \times 10^6 M_\odot$, concentrated within a radius of 0.016 pc [68] and located very close to Sgr A*. In the most recent observations [28], a mass of $(2.6 \pm 0.2) \times 10^6 M_\odot$, enclosed within a radius of 0.015 pc has been confirmed. In the latter observations, the accuracy of the velocity measurements in the central arcsec^2 has been improved considerably, and thus the error bar on the central mass has been reduced by about a factor of 4. In both data sets, the presence of a supermassive compact dark object is revealed by the fact that several stars are moving within a projected distance of less than 0.01 pc from the central radio source Sgr A* at projected velocities in excess of 1000 km/s.

For completeness, we mention here that the mass distribution at the Galactic center could also be studied through the motion of gas clouds and streamers [26, 105, 106]. However, gas flows may be easily perturbed by non-gravitational forces such as shocks, radiation pressure, winds, magnetic

fields,etc., and hence this probe is considered to be less reliable for determining the mass of the compact dark object at the Galactic center.

The non-thermal spectrum of Sgr A* [107], that has been shown to originate from a very compact source [28, 68, 108, 109], and the low proper motion of Sgr A* [110, 111] have led many [78] to suggest that Sgr A* may be a supermassive BH of mass $\sim 2.6 \times 10^6 M_\odot$. Supermassive BHs have also been inferred for several other galaxies such as M87 [25, 112, 113] and NGC 4258 [114, 115].. Taking this suggestion seriously, one is immediately faced with fundamental issues such as the prevalence of supermassive BHs in the nuclei of normal galaxies and the nature of the accretion mechanism that makes Sgr A* so much fainter than typical active galactic nuclei [116, 117].

Observations of gas flows in the vicinity of Sgr A* indicate a mass accretion rate onto the central object of $\sim 10^{-4} M_\odot \mathrm{yr}^{-1}$ [99, 118]. In a standard disk theory with a reasonable efficiency of $\sim 10\%$, this accretion rate would correspond to a luminosity of $\sim 10^{42}$ ergs s^{-1}. However, the actual luminosity observed is $\sim 10^{37}$ergs s^{-1}. Moreover, the spectrum is essential flat in νL_ν from radio waves to X-rays, with the exception of a few bumps [108, 119, 120, 121, 122]. Thus both the observed low luminosity and the spectral energy distribution differ very much from the spectrum expected from a standard thin disk around a supermassive black hole. This discrepancy is known as the "blackness problem" of the Galactic center. Both the blackness of Sgr A*, and its peculiar spectrum were the source of exhaustive debate in the recent past. Several models for the accretion and emission spectrum of Sgr A* have been proposed. The spectrum of Sgr A* has been modelled as a synchrotron radiation from thermal electrons [116], heated through the dissipation of magnetic energy, as a result of a the Bondi-Hoyle accretion process fed by winds emanating from the stars in the vicinity of Sgr A*. Optically thick synchrotron radiation emitted by a jet-disk system was also proposed as an explanation for the radiation of Sgr A* [123, 124, 125]. Moreover, synchrotron radiation emitted by a quasi-monoenergetic ensemble of relativistic electrons [126] has been put forward as a possible emission mechanism.

Probably the most sophisticated model that attempts to explain the observed emission spectrum of Sgr A* from radio waves to γ rays is based on Advection Dominated Accretion Flows (ADAF) [117, 127, 128, 129]. This model is based on the concept of advection dominated flow, in which most of the energy released by viscous dissipation is stored as thermal energy in the gas and advected to the center and only a small fraction of the energy is radiated off [130, 131]. The ADAF models assume that the compact dark object at the Galactic center is a *black hole*. The existence of an event horizon in a black hole is essential in order to ensure that whatever energy falls into the central object disappears without being re-radiated. This model also requires the protons to have a much higher temperature than the electrons, and the gas must therefore have a two-temperature structure. However, it has also

been recently pointed out that ADAF models, as a solution of astrophysical accretion problems, should be treated with some caution as their physical basis is somewhat uncertain [132, 133]. It is worthwhile to note that the VLBI observations of Sgr A*, have revealed that the observed size follows a λ^2 dependence and the apparent source structure can be described by an elliptical Gaussian brightness distribution [108, 109, 134, 135, 136, 137].

A direct proof of the existence of supermassive massive black holes would require the detection of objects that are moving at relativistic velocities at distances close to the Schwarzschild radius. However, as the best current observations probe the gravitational potential at radii 4×10^4 larger than the Schwarzschild radius of a black hole of mass $2.6 \times 10^6 M_\odot$ [28], thus there is no compelling direct evidence that a supermassive black hole actually does exist at the Galactic center. It is therefore perhaps prudent not to focus too much on the black hole scenario as the only possible solution for the supermassive compact dark object at the Galactic center, without having explored alternative scenarios.

One alternative to the BH scenario is a very compact dark stellar cluster [61, 62]. However, based on the evaporation and collision time stability criteria, it is doubtful that such clusters could have survived up to the present time (see ref. [138] for an alternative point of view). Indeed, in the case of our Galaxy and NGC 4258, it has been found [60, 63] that even the lower limits to the half-mass densities of such compact clusters ($1 \times 10^{12} M_\odot \mathrm{pc}^{-3}$ for NGC 4258 and $6 \times 10^{11} M_\odot \mathrm{pc}^{-3}$ for our Galaxy) are too large that they could be due to stable clusters of stellar or substellar remnants. The estimated maximal lifetimes for such dense clusters are about 10^8 years for the Galaxy and a few 10^8 years for the NGC 4258, i.e. much shorter than the age of the Universe. This seems to rule out the existence of dense clusters at the centers of the above mentioned galaxies, unless we are prepared to believe that we happen to live in a privileged epoch of the lifetime of the Universe. Note, however, that for other galaxies, such as M31, M32, M87, NGC 3115, NGC 3377, NGC 4261, NGC 4342, NGC 4486B and NGC 4594, maximal lifetimes of dense stellar clusters are in excess of 10^{11} years. Moreover, it should be acknowledged that the uncertainties in the understanding of the core collapse process of such dense clusters still leave some room for speculation about a possible interpretation of the supermassive compact dark objects at the centers of galaxies (including both, our Galaxy and NGC 4258) in terms of e.g. core-collapsed clusters [60]. But, apart from a cluster of very low mass BH's that is free of stability problems, the most attractive alternative to a dense stellar cluster is a cluster of elementary particles.

In fact, in the recent past, an alternative model for the supermassive compact dark objects in galactic centers has been developed [30, 31, 32, 36, 45, 46, 39, 64, 65]. The cornerstone of this model is that the dark matter at the center of galaxies is made of nonbaryonic matter in the form of massive

neutrinos that interact gravitationally forming supermassive neutrino balls in which the degeneracy pressure of the neutrinos balances their self-gravity. Such neutrino balls could have been formed in the early Universe during a first-order gravitational phase transition [37, 42, 43, 44]. In fact, it has been recently shown that the dark matter concentration observed through stellar motion at the Galactic center [27, 67] is consistent with a supermassive object of 2.5×10^6 solar masses made of self-gravitating, degenerate heavy neutrino matter [31]. Moreover, it has been shown that an acceptable fit to the infrared and radio spectrum above 20 GHz, that is presumably emitted by the compact dark object, can be reproduced in the framework of standard accretion disk theory [30, 32, 69], in terms of a baryonic disk immersed in the shallow potential of the degenerate neutrino ball of 2.6×10^6 solar masses.

In this chapter we will compare the predictions of these two models for the supermassive compact dark object at the center our Galaxy, i.e. (i) the black hole scenario and (ii) the degenerate neutrino ball scenario as an example of an extended object. Both these models are not in contradiction with the technologically challenging proper motions observations [28, 68]. It is therefore desirable to have an independent test, in order to distinguish between these two scenarios describing the compact dark object at the center of our Galaxy. To do this, we perform a full analysis of the orbits [71, 72] of the fastest and the closest star in the central arcsec^2 using the most recent observations in the central arcsec^2 of our Galaxy [28, 68]. We then calculate the emission spectrum of the compact dark object in both scenarios and compare our predictions with the observed spectrum of Sgr A*.

4.2 The compact dark object as a neutrino ball

Dark matter at the Galactic center can be described by the gravitational potential $\Phi(r)$ of the neutrinos and antineutrinos that satisfies Poisson's equation

$$\Delta\Phi = 4\pi G\rho_\nu, \tag{4.1}$$

where G is Newton's gravitational constant and ρ_ν is the mass density of the neutrinos and antineutrinos. Neutrino matter will interact gravitationally to form supermassive neutrino balls in which self-gravity of the neutrinos is being balanced by their degeneracy pressure $P_\nu(r)$ according to the equation of hydrostatic equilibrium

$$\frac{dP_\nu}{dr} = -\rho_\nu \frac{d\Phi}{dr}\ . \tag{4.2}$$

In order to solve equation (4.1), one needs a relation between the pressure P_ν and the density ρ_ν. To this end we choose the polytropic equation of state

of degenerate neutrino matter, i.e.

$$P_\nu = K\rho_\nu^{5/3}, \tag{4.3}$$

where the polytropic constant K is given by (Viollier, 1994)

$$K = \left(\frac{6}{g_\nu}\right)^{2/3} \frac{\pi^{4/3}\hbar^2}{5m_\nu^{8/3}}. \tag{4.4}$$

Here, m_ν denotes the neutrino mass, g_ν is the spin degeneracy factor of the neutrinos and antineutrinos, i.e. $g_\nu = 2$ for Majorana and $g_\nu = 4$ for Dirac neutrinos and antineutrinos. We now introduce the dimensionless potential and radial variable, v and x, by

$$\Phi(r) = \frac{GM_\odot}{a_\nu}\left(v'(x_0) - \frac{v(x)}{x}\right), \tag{4.5}$$

$$r = a_\nu x, \tag{4.6}$$

where x_0 is the dimensionless radius of the neutrino ball, and the scale factor a_ν which plays here the role of a length unit is given by

$$a_\nu = 2.1376 \text{ lyr} \times \left(\frac{17.2 \text{ keV}}{m_\nu c^2}\right)^{8/3} g_\nu^{-2/3}. \tag{4.7}$$

Assuming spherical symmetry, we finally arrive at the non-linear Lané-Emden equation

$$\frac{d^2v}{dx^2} = -\frac{v^{3/2}}{x^{1/2}}, \tag{4.8}$$

with polytropic index 3/2. The boundary conditions are chosen in such a way that v vanishes at the boundary x_0 of a pure neutrino ball, i.e. $v(0) = 0$. The mass enclosed within a radius r in a pure neutrino ball can be written in terms of $v(x)$ and its derivative $v'(x)$ as

$$M(r) = \int_0^r 4\pi\rho_\nu r^2 dr = -M_\odot\left(v'(x)x - v(x)\right). \tag{4.9}$$

In order to describe the compact dark object at the Galactic center as a neutrino ball and constrain its physical parameters appropriately, it is worthwhile to use the most recent observational data [28], in which it has been established that the mass enclosed within 0.015 pc at the Galactic center is $(2.6 \pm 0.2) \times 10^6$ solar masses. We choose the minimal neutrino mass m_ν to reproduce the observed matter distribution, as can be seen from Fig. 4.1, where we have added the most recent observational data points with error bars [68, 28]. In Fig. 4.1 we include only the neutrino ball contribution to the enclosed mass, as the stellar cluster contribution is negligible by orders

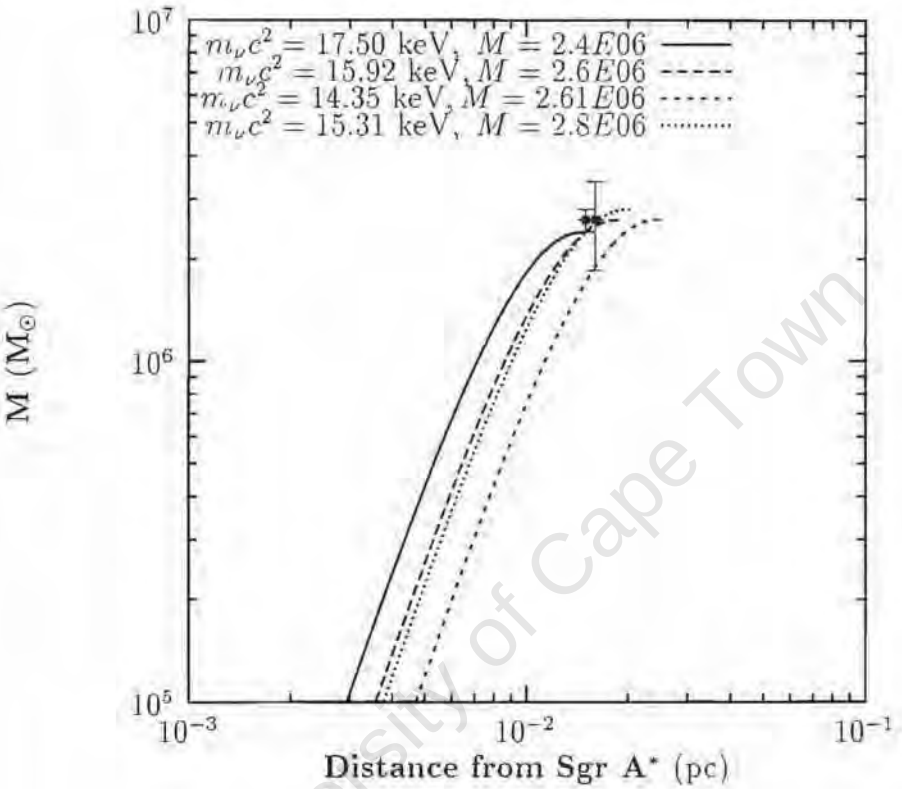

Figure 4.1: The mass enclosed in a neutrino ball of 2.4, 2.6, 2.61 and 2.8 millions solar masses. Based on the data from ref. [28], the bounds on the neutrino mass are $m_\nu \geq 17.50$ keV/c^2 for $g_\nu = 2$ or $m_\nu \geq 14.72$ keV/c^2 for $g_\nu = 4$ and $M = 2.4 \times 10^6 M_\odot$. For $M = 2.6 \times 10^6 M_\odot$ the bounds on the neutrino mass are $m_\nu \geq 15.92$ keV/c^2 for $g_\nu = 2$ and $m_\nu \geq 13.39$ keV/c^2 for $g_\nu = 4$. Finally, a neutrino mass range of $m_\nu \geq 15.31$ keV/c^2 for $g_\nu = 2$ or $m_\nu \geq 12.87$ keV/c^2 for $g_\nu = 4$ is consistent with a supermassive object of $M = 2.8 \times 10^6 M_\odot$. The data points with errorbars from ref. [68, 28] are also shown in this graph.

of magnitude at these radii. For a $M = 2.4 \times 10^6 M_\odot$ neutrino ball, the constraints on the neutrino mass are $m_\nu \geq 17.50$ keV$/c^2$ for $g_\nu = 2$ and $m_\nu \geq 14.72$ keV$/c^2$ for $g_\nu = 4$, and the radius of the neutrino ball is $R \leq 1.50 \times 10^{-2}$ pc. Using the value of $M = 2.6 \times 10^6 M_\odot$, the bounds on the neutrino mass are $m_\nu \geq 15.92$ keV$/c^2$ for $g_\nu = 2$ or $m_\nu \geq 13.39$ keV$/c^2$ for $g_\nu = 4$ and the radius of the neutrino ball turns out to be $R \leq 1.88 \times 10^{-2}$pc. Choosing a $M = 2.8 \times 10^6 M_\odot$ neutrino ball, the range of neutrino mass is $m_\nu \geq 15.31$ keV$/c^2$ for $g_\nu = 2$ and $m_\nu \geq 12.87$ keV$/c^2$ for $g_\nu = 4$ and the corresponding neutrino ball radius $R \leq 2.04 \times 10^{-2}$ pc. Finally by using the data from ref. [68] where it has been shown that the enclosed mass at the Galactic center within 0.016 pc (the innermost data point) is $(2.65 \pm 0.76) \times 10^6 M_\odot$. We find that the bounds on the mass of the neutrino are $m_\nu \geq 12.07$ keV$/c^2$ for $g_\nu = 4$ or $m_\nu \geq 14.35$ keV$/c^2$ for $g_\nu = 2$, Thus, using the value of $M = 2.61 \times 10^6 M_\odot$ [68] for the mass of the neutrino ball, the radius turns out to be $R = 2.48 \times 10^{-2}$ pc (we assume that the distance to Sgr A* is 8.0 kpc throughout this chapter).

In the following we restrict our calculations to the minimal neutrino mass or the largest neutrino ball size that is consistent with observational data [68, 28]. in order to emphasize the difference between the neutrino ball and the black hole scenarios. By varying the neutrino mass between the minimal and the maximal value, that is given by the Oppenheimer-Volkoff (OV) limit, i.e. $m_\nu = 491$ keV$/c^2$ for $g_\nu = 2$ and $M_{\rm OV} = 2.60 \times 10^6 M_\odot$, one may interpolate smoothly between the extended neutrino ball and the "almost black hole" scenarios. However, it is important to note that the duration of the neutrino burst of SN1987A restricts a possible Dirac neutrino mass to $m_\nu \lesssim 30$ keV$/c^2$ [139]. This restriction is based on the fact that trapped Dirac neutrinos eventually produce their sterile components in nuclear collisions in the nascent neutron star. The sterile neutrinos would escape too early to be consistent with the duration of the neutrino burst of SN1987A for $m_\nu \gtrsim 30$ keV$/c^2$. Moreover, if we want to explain the most massive compact dark objects at the centers of galaxies, e.g. at the center of M87 with $M = (3.2 \pm 0.9) \times 10^9 M_\odot$, as a stable degenerate neutrino ball at or below the OV limit, the neutrino mass must be smaller than 16.5 keV$/c^2$ for $g_\nu = 2$ [39] (see chapter 3).

4.3 Dynamics of the fastest star near the Galactic center

We investigate the motion of the closest star to the Galactic center and the fastest star in the central 1 arcsec^2 around Sgr A*. We study the motion

of S1[1] (or S0-1) in the gravitational potential of Sgr A* assuming that the latter is either a BH of mass M or a spatially extended object, i.e. a neutrino ball of the same mass M consisting of self-gravitating heavy neutrino matter. We use Newtonian dynamics, as the problem is essentially nonrelativistic, because the mass of the neutrino ball is much less than the Oppenheimer-Volkoff limit corresponding to this particular neutrino mass [39]. Consequently, we can write Newton's equations of motion as

$$\ddot{x} = -\frac{GM(r)}{(x^2+y^2+z^2)^{3/2}}x, \tag{4.10}$$

$$\ddot{y} = -\frac{GM(r)}{(x^2+y^2+z^2)^{3/2}}y, \tag{4.11}$$

$$\ddot{z} = -\frac{GM(r)}{(x^2+y^2+z^2)^{3/2}}z, \tag{4.12}$$

where x, y, z denote the components of the radius vector of the star S1 (S0-1) and $r = \sqrt{x^2+y^2+z^2}$, Sgr A* being the origin of the coordinate system. We assume that the center of the neutrino ball and the BH is at the position of Sgr A*. The dot denotes of course the derivative with respect to time. In the case of a BH, $M(r) = M$ is independent of r, while in the neutrino ball scenario, $M(r)$ is the mass of neutrinos and antineutrinos enclosed within a radius r and is given by Eq. (4.9). We can therefore express the escape v_e and circular velocities v_c [70] of the falling matter onto the neutrino ball as

$$v_e = \sqrt{-2\Phi(r)}, \tag{4.13}$$

and

$$v_c = \sqrt{\frac{GM(r)}{r}}, \tag{4.14}$$

where $\Phi(r)$ and $M(r)$ are given by Eqs. (4.5) and (4.9), respectively.

In Figs. 4.2 and 4.3, we plot the escape and circular velocities as functions of the distance from Sgr A*, for both black hole and neutrino ball scenarios. In these graphs, we have also included the velocities of stars around the Galactic center [28], assuming that the velocity component and distance from Sgr A* in the line-of-sight are both zero, i.e. $v_z = 0$ and $z = 0$. We, therefore, must allow for a shift of the data upwards and to the right by an unknown amount, because v_z has not been measured and z cannot be measured. Taking a reasonable shift into the data, we can say with some confidence that the nearest to the center and the fast moving star S1 [68] or S0-1 [28], moving at projected velocity $\sqrt{v_x^2+v_y^2} = (1400 \pm 100)$ km/s, is consistent with the local escape velocity at the projected velocity $\sqrt{v_x^2+v_y^2}$ of S1 (S0-1) from Sgr A*.

[1]The fastest and the closest star to the Galactic center is named S1 and S0-1 according to the nomenclature from refs. [68, 28], respectively.

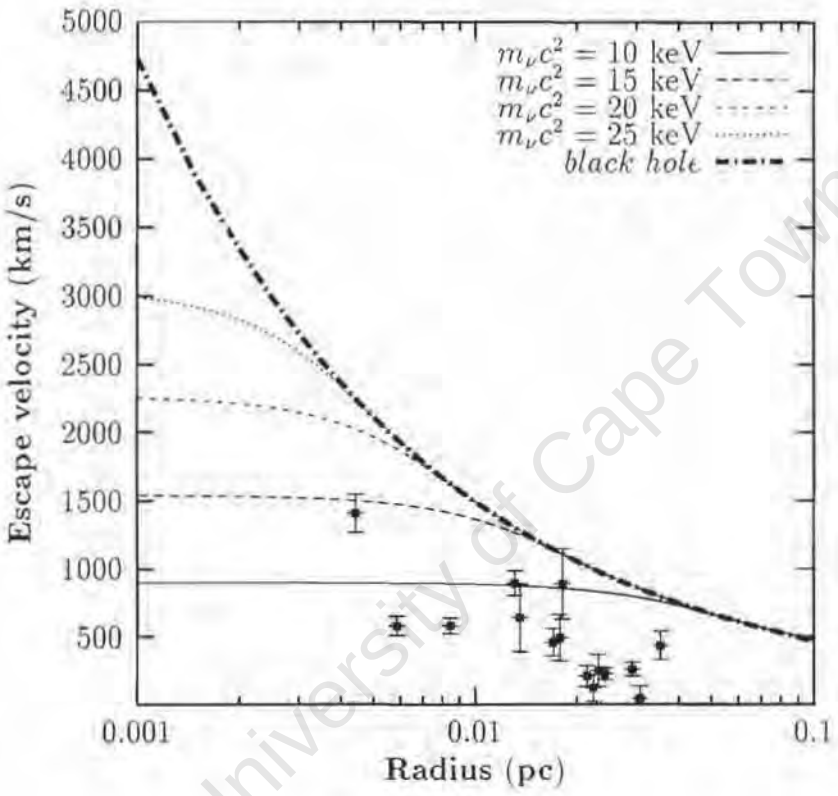

Figure 4.2: The escape velocity as a function of the distance from Sgr A* for the black hole and neutrino ball scenarios. The data are taken from ref. [28] assuming that the projected velocity and distance from Sgr A* are equal to the true velocity and distance, respectively.

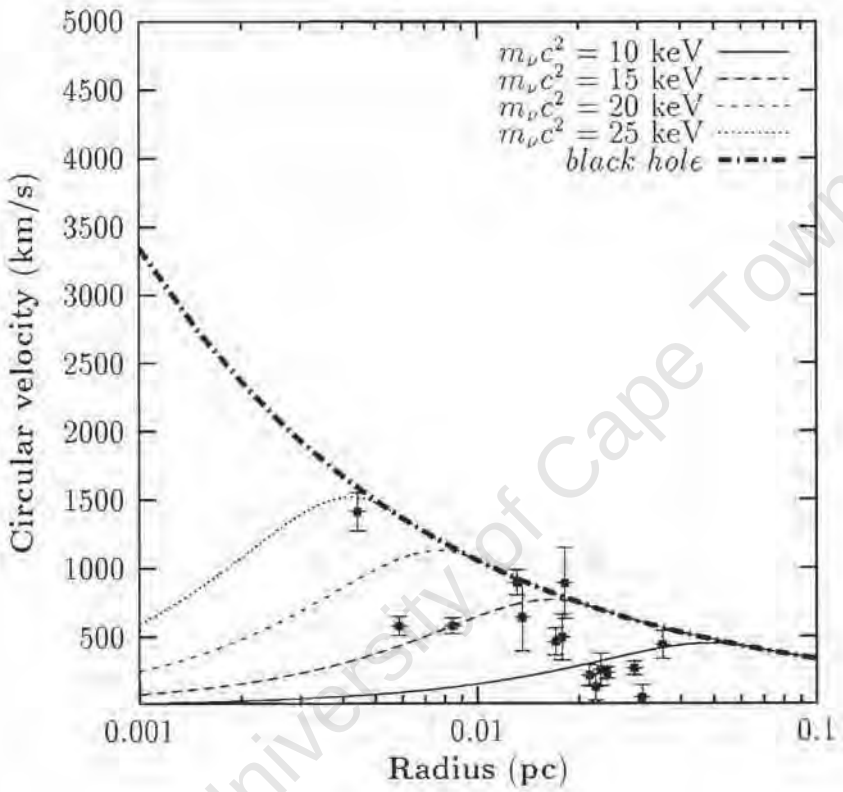

Figure 4.3: The circular velocity as a function of the distance from Sgr A* for the black hole and neutrino ball scenarios. The data are taken from ref. [28] assuming that the projected velocity and distance from Sgr A* are equal to the true velocity and distance, respectively.

4.3.1 Orbits of S1

We use the proper motion data of stars in the central cluster around Sgr A* [66, 68] to study the motion of the fastest star S1. In 1994 the coordinates of S1 were RA $= -0.19''$ and DEC $= -0.04''$, with Sgr A* being the origin of the coordinate system, and the x- and y-components of the projected velocity, $v_x = 650 \pm 400$ km/sec and $v_y = -1530 \pm 400$ km/sec, respectively, deduced from the 1994 and 1996 data. Here x is opposite to the RA direction and y is in DEC direction. We then solve Newton's equations (4.10)-(4.12) for two cases (i) a black hole with a mass $2.61 \times 10^6 M_\odot$ and (ii) a neutrino ball of the same mass, with the neutrino mass fixed at the lower limit allowed by the stellar proper motion data [68]. Note, that increasing of the neutrino mass will smoothly interpolate between the scenarios (ii) and (i). A typical result of such calculation is shown in Fig. 4.1 where we plot the two orbits of S1 corresponding to the BH and neutrino ball scenarios. The neutrino ball is represented by the dotted circle with its center (star) at the position of Sgr A*. The values for v_x and v_y are taken as 650 km/s and -1530 km/sec, respectively. Sgr A* and S1 are assumed to be at the same distance from the observer, i.e. the z coordinate of the star S1, as measured in the line-of-sight from Sgr A*, is zero. Moreover, the velocity component in the line-of-sight of the star S1, v_z, has also been set to zero in this figure. The unknown quantities, z and v_z, are the major source of uncertainty in determining the intrinsic orbit of the star S1. However, as we will see below, this shortcoming will not substantially affect the predictive power of our model if appropriately dealt with. Finally, the full square labels on the orbits denote time in years. Due to the fact that the gravitational force at a given distance from Sgr A* is determined by the mass enclosed within this distance, the star S1 will be deflected much less in the neutrino ball scenario than in the BH scenario of Sgr A*, as can be seen from Fig. 4.1.

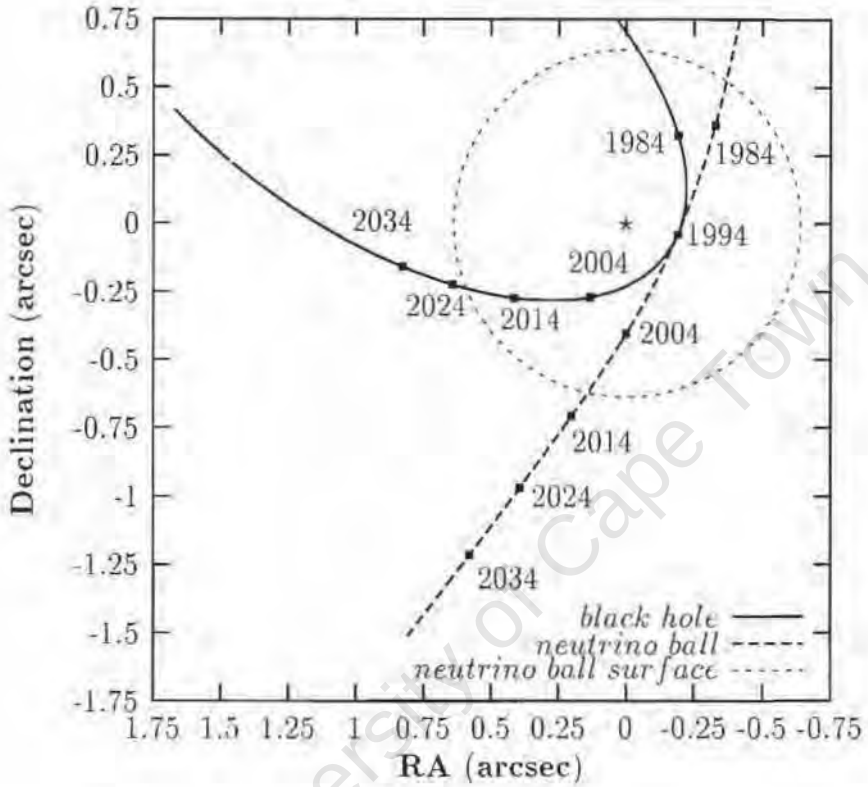

Figure 1.4: Projected orbits of the star S1 in the case of a supermassive BH of a mass $2.61 \times 10^6 M_\odot$ (solid line) and in the case of a neutrino ball (dashed line). The surface of the neutrino ball with the same mass as the BH, and consisting of heavy, degenerate neutrino matter with neutrino masses $m_\nu = 12.07$ keV$/c^2$ for $g_\nu = 4$ or $m_\nu = 14.35$ keV$/c^2$ for $g_\nu = 2$ is shown by the dotted circle The neutrino ball has a radius of 9.9182×10^4 Schwarzschild radii. The star in the upper-right corner denotes Sgr A*. In this plot $v_x = 650$ km/sec, $v_y = -1530$ km/sec and $v_z = z = 0$.

It is worthwhile to note at this stage that the observational test which we propose is somewhat reminiscent of Rutherford's experiments at the beginning of this century. These experiments led to abandoning of Thomson's "pudding" model of the atom (which described atom as an extended positively charged spherical cloud, with electrons like raisins in a pudding whose oscillation around the equilibrium point was providing electromagnetic radiation) and established the current views of the atomic structure of matter and the "compactness" of the nucleus.

Returning back to Fig. 4.4, it seems that, since the positions of the stars S1-S11 are known to 30 mas accuracy, distinguishing the BH from the neutrino ball scenario for Sgr A* might be possible in a few years time. However, as we will discuss below, this estimate is perhaps too optimistic, since it does not take into account the uncertainties due to the complete lack of information on z and v_z. Moreover, as we know, there are also large uncertainties in the determination of v_x and v_y. Of course, all these uncertainties will eventually decrease, as more data will become available, since the projected orbit, inclusive v_z and z, will be completely determined by the accurate measurement of the position of S1 as a function of time. Thus, as our next step, we will investigate the errors in the velocity components in more detail. To this end, we have performed calculations of the orbit of the star S1 in both BH and neutrino ball scenarios, taking into account the error bars of v_x and v_y. The results of this calculation are presented in the Fig. 4.5. The top panel represents the orbits in the case of a BH, whereas, the lower panel describes the neutrino ball scenario. The spread of the orbits induced by the uncertainties in v_x and v_y is quite large. In the BH scenario, the curves 1, 2 and 4 are bound orbits (ellipses with the BH in one focus), whereas in the neutrino ball scenario only one orbit is bound (curve 2, which is actually a rosette-type orbit). In both cases we assume $z = v_z = 0$. At first sight, it may seem that the results of this calculation are inconclusive, especially in view of the current complete uncertainty in z and v_z. Let us first see how the orbits of S1 (S0-1) are affected by the most recent observations [28] before coming back to the dependence of the orbits on z and v_z.

4.3.2 Orbits of S0-1

We now turn to the study of the orbits of S1 named S0-1 according to the nomenclature used in ref. [28]. The input positions and velocities for the system of Eqs. (4.10) - (4.12) are taken to be those of S0-1 in 1995.4, when the coordinates of S0-1 were RA $= -0.107''$ and DEC $= 0.039''$. The x and y components of the projected velocity are $v_x = 470 \pm 130$ km/s and $v_y = -1330 \pm 140$ km/s [28], respectively. Here x is opposite to the RA direction and y is in the DEC direction. In Fig. 4.6 we plot two typical orbits of S0-1 corresponding to the BH and neutrino ball of mass $M = 2.6 \times 10^6 M_\odot$.

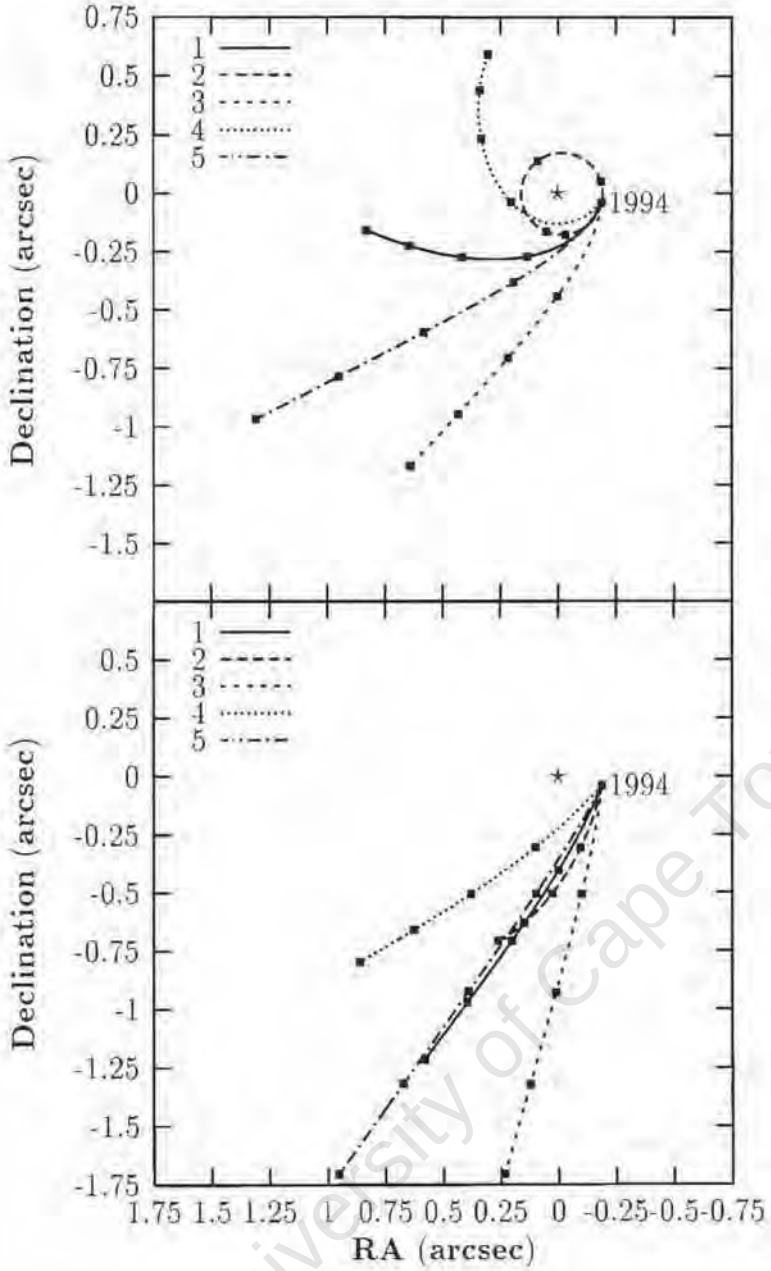

Figure 4.5: Projected orbits of the star S1 in the case of a supermassive black hole (top panel) and in the case of a neutrino ball (lower panel) for $v_z = z = 0$. In this graph we explore how the orbits are affected by the uncertainty in v_x and v_y. The labels for orbits are: 1: $v_x = 650$ km/sec and $v_y = -1530$ km/sec (median values, orbit is bound in the case of a BH and unbound for the neutrino ball); 2: $v_x = 250$ km/sec and $v_y = -1130$ km/sec (orbits are bound in both cases); 3: $v_x = 250$ km/sec and $v_y = -1930$ km/sec (orbits are unbound in both cases); 4: $v_x = 1050$ km/sec and $v_y = -1130$ km/sec (orbit is bound in the case of a BH and unbound for a neutrino ball); 5: $v_x = 1050$ km/sec and $v_y = -1930$ km/sec (orbits are unbound in both cases). The time labels (filled squares) on the orbits are placed in intervals of 10 years, up to the year 2034.

The input values for v_x and v_y are 470 and -1330 km/s, respectively. The z-coordinate of the star S0-1 is assumed to be zero and the velocity component in the line-of-sight of the star S0-1, v_z, has also been set equal to zero in this graph. The filled square labels denote the time in years from 1990 till 2015. In the case of a BH, the orbit of S0-1 is an ellipse, with Sgr A* being located in one focus (denoted by the star in the figure). The period of S0-1 is 12.7 years and the minimal and maximal distances from Sgr A* are 1.49 and 7.18 light days, respectively. In the case of a neutrino ball, the orbit will be bound but not closed (see Appendix C), with minimal and maximal distances from Sgr A* of 3.98 and 42.07 light days, respectively.

It can be seen from Fig. 4.6 that, in the case of a neutrino ball, S0-1 is deflected much less than for a BH, as the gravitational force at a given distance from Sgr A* is determined by the mass enclosed within this distance. Using Eq. (4.9) we can estimate the mass enclosed within a radius corresponding to the projected distance of S0-1 from Sgr A* (4.41×10^{-3} pc) to be $\sim 1.8 \times 10^5 M_\odot$. Thus, in the case of a neutrino ball, the force acting on S0-1 is about 14 times less than in the case of a BH. This graph can serve to establish, whether Sgr A* is a BH or an extended object, due to the quite different positions of S0-1 as a function of time in both scenarios. However, this conclusion is perhaps too optimistic, as we have not considered (i) the uncertainties in v_x and v_y, (ii) the error bars in the total mass of the BH or neutrino ball, (iii) the complete lack of information on z and v_z.

As a next step, we investigate the dependence of the orbits on the uncertainties in the velocity components. The results of this calculation are presented in Fig. 4.7 where we have set $z = v_z = 0$. In the case of a BH, the ellipses correspond to the orbits of S0-1, while the other 5 thick lines are bound orbits of S0-1 for the neutrino ball scenario. The spread of the orbits induced by the error bars in v_x and v_y is small compared to the orbits presented in Fig. 4.5 [71] using the data from ref. [68]. The time labels, represented by filled squares on the orbits, are placed in intervals of 5 years: starting from 1995.4 up to 2005 in the case of a BH, and up to 2015 in the case of a neutrino ball. The periods of S0-1 for different orbits vary between 10 and 17 years for the BH scenario. We thus see that the error bars in v_x and v_y do not alter the predictions of Fig. 4.6 in substance. We now would like to study, how the orbits are changed if we let the mass of the neutrino ball or the BH vary within the estimated error bars [28].

In Figs. 4.8 and 4.9, we present the results of our calculations, in both cases, for masses of $M = 2.4 \times 10^6 M_\odot$ and $M = 2.8 \times 10^6 M_\odot$, respectively. The neutrino masses derived are $m_\nu = 17.50$ keV/c^2 for a $M = 2.4 \times 10^6 M_\odot$ neutrino ball and $m_\nu = 15.31$ keV/c^2 for a $M = 2.8 \times 10^6 M_\odot$ neutrino ball. The filled squares represent the time labels spaced by 5 year intervals as in Fig. 4.7. In the BH scenario, the periods of S0-1 with $M = 2.4 \times 10^6 M_\odot$ vary between 11 years and 20 years, while in the case of a $M = 2.8 \times 10^6 M_\odot$,

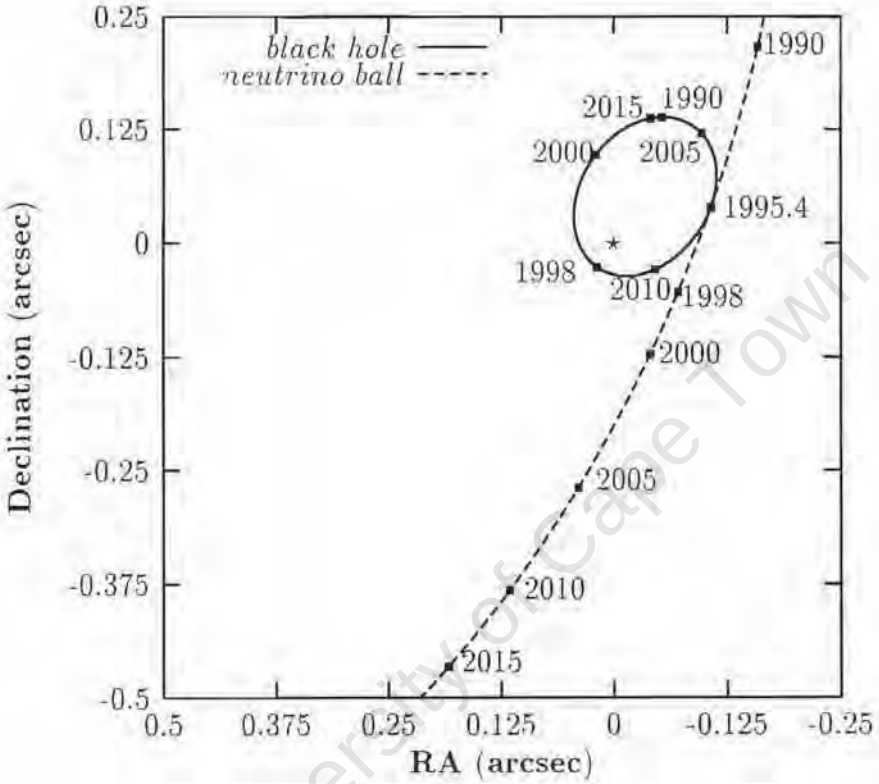

Figure 1.6: Projected orbits of the star S0-1 for BH and neutrino ball scenarios with $M = 2.6 \times 10^6 M_\odot$ and $v_z = z = 0$. The velocity components of S0-1 are taken to be $v_x = 470$ km/s and $v_y = -1330$ km/s. The filled squares denote the time labels. The period of S0-1 in a the BH scenario is 12.7 years and the minimal and maximal distances from Sgr A* are 1.49 and 7.18 light days. The orbit of S0-1 in the neutrino ball scenario is bound with minimal and maximal distances from Sgr A* of 3.98 and 42.07 light days, respectively.

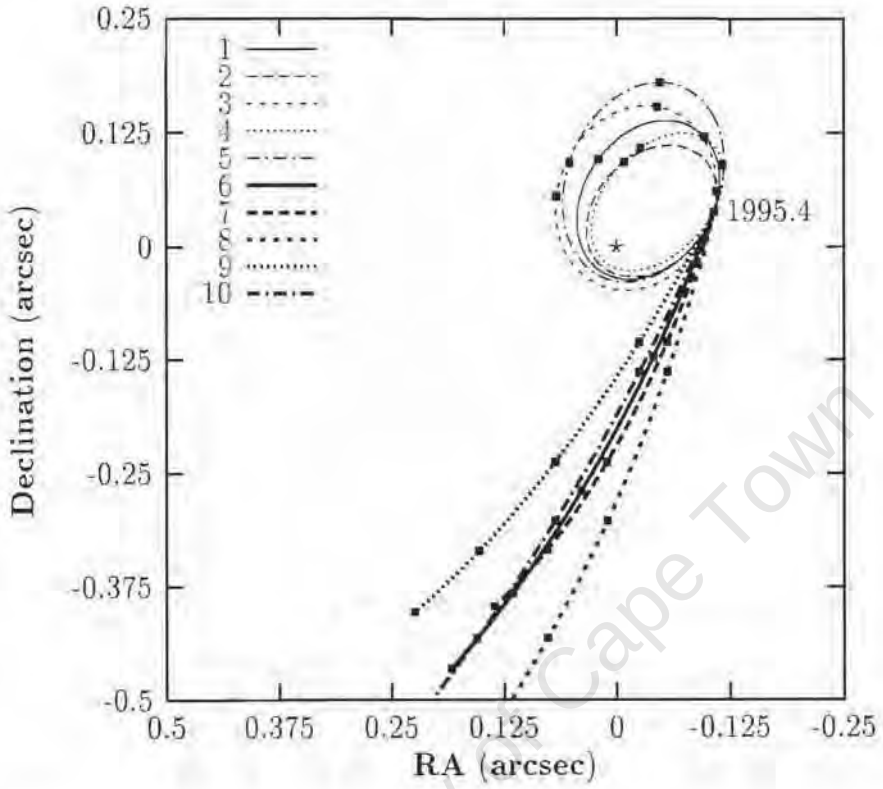

Figure 4.7: Projected orbits of the star S0-1 in the case of a BH or a neutrino ball of $M = 2.6 \times 10^6 M_\odot$ taking into account the error bars in the velocity components. The labels for the different orbits are: 1: $v_x = 470$ km/s and $v_y = -1330$ km/s (median values), 2: $v_x = 340$ km/s and $v_y = -1190$ km/s, 3: $v_x = 340$ km/s and $v_y = -1470$ km/s, 4: $v_x = 600$ km/s and $v_y = -1190$ km/s, 5: $v_x = 600$ km/s and $v_y = -1470$ km/s. The periods of S0-1 for different orbits in the BH scenario vary between 10 and 17 years. The thick lines 6 to 10 correspond to the orbits in the neutrino ball scenario with the following description: 6: $v_x = 470$ km/s and $v_y = -1330$ km/s (median values), 7: $v_x = 340$ km/s and $v_y = -1190$ km/s, 8: $v_x = 340$ km/s and $v_y = -1470$ km/s, 9: $v_x = 600$ km/s and $v_y = -1190$ km/s, 10: $v_x = 600$ km/s and $v_y = -1470$ km/s. All the orbits in both scenarios are bound. The time labels (filled squares) on the orbits are placed in intervals of 5 years, up to the year 2005 in the case of a BH and up to 2015 in the case of a neutrino ball.

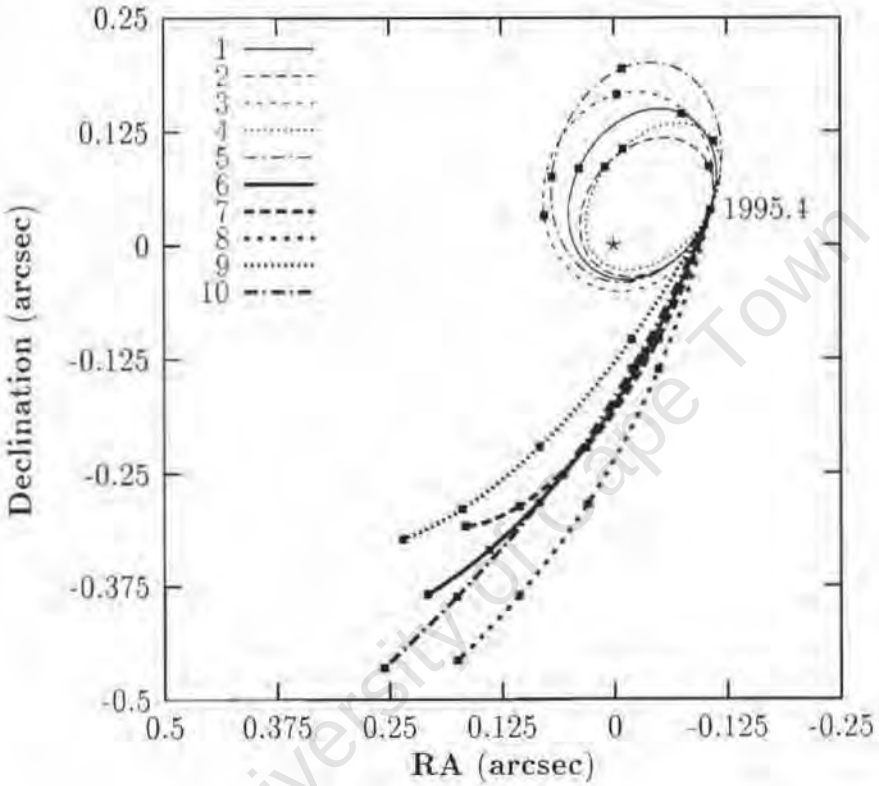

Figure 4.8: Projected orbits of the star S0-1 in the case of a BH or neutrino ball with $M = 2.4 \times 10^6 M_\odot$. In this graph we explore how the orbits are affected by the uncertainty in the mass of the BH or neutrino ball. The orbits are calculated for $z = v_z = 0$. The description of the orbits are the same as Fig. 4.7. The periods of S0-1 in the BH scenario vary between 11 and 20 years and all the orbits are bound in both scenarios.

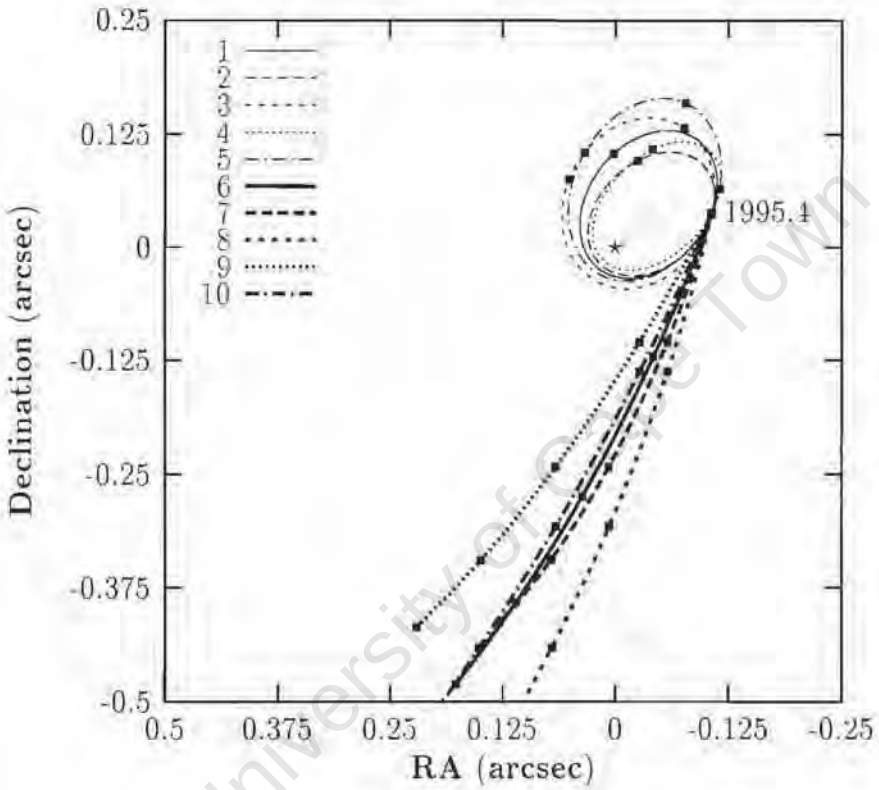

Figure 4.9: Projected orbits of the star S0-1 for $M = 2.8 \times 10^6 M_\odot$. All the orbits are bound and calculated for different values of the velocity components as in Fig. 4.7. The periods of S0-1 vary between 9.5 years and 14.7 years in the BH scenario.

the periods vary between 9.5 and 15 years. Comparing the orbits of S0-1 in Figs. 4.9 and 4.8 with those in Fig. 4.7, we conclude that the errors bars in the total mass of the BH or neutrino ball have no significant effect on the motion of S0-1. In both scenarios of the supermassive compact dark object, all the orbits considered for three different values of the BH or neutrino ball mass are bound, as can be seen from Figs. 1.10 and 4.11, where we plot the escape and circular velocities as functions of the distance from Sgr A*. In these graphs, we have also included the data from ref. [28] with error bars, for the 15 stars in the central arsec^2, assuming that the velocity component and distance from Sgr A* in the line-of-sight are both zero, i.e. $v_z = 0$ and $z = 0$. Thus, the data points are lower bounds on the true circular or escape velocity and radius, and the real values lie in the quarter plane to the right-and-up of the measured data point. For instance, the innermost data point describing the star S0-1 is in both scenarios, consistent with a bound orbit if $|z|$ and $|v_z|$ are not too large, as can be seen from the escape velocity in Fig. 4.10. However, S0-1 cannot be interpreted as a virialised star in the neutrino ball scenario, as is evident from the plot of the circular velocity in Fig. 4.11 ; it thus would have to be an intruder star. If the projected velocity of a star at a given projected distance from Sgr A* is larger than the escape velocity at the same distance (assuming $z = 0$), the neutrino ball scenario is virtually ruled out, since the kinetic energy of the star would have to be very large at infinity.

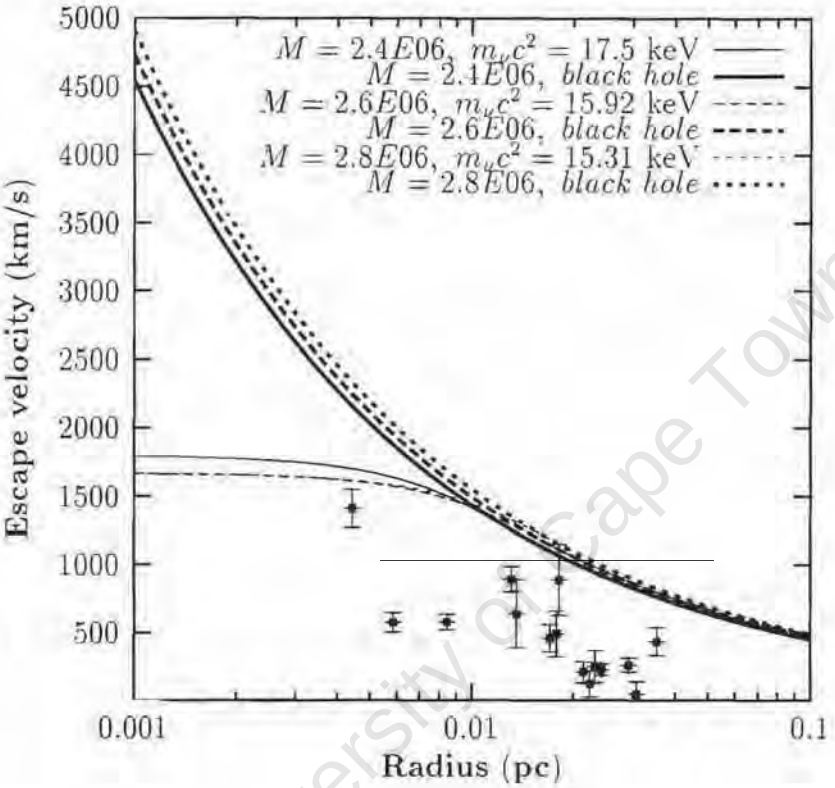

Figure 4.10: The escape velocity as a function of the distance from Sgr A* for BH and neutrino ball scenarios. The value of the mass of the central object is varied as indicated on the graph. The data points with error bars of 15 stars in the central arcsec^2 are taken from ref. [28] assuming that the projected velocity and distance from Sgr A* are equal to the true velocity and distance, respectively, i.e. $z = 0$ and $v_z = 0$. This graph shows that S0-1 is bound in both scenarios for different values of the mass of the central object.

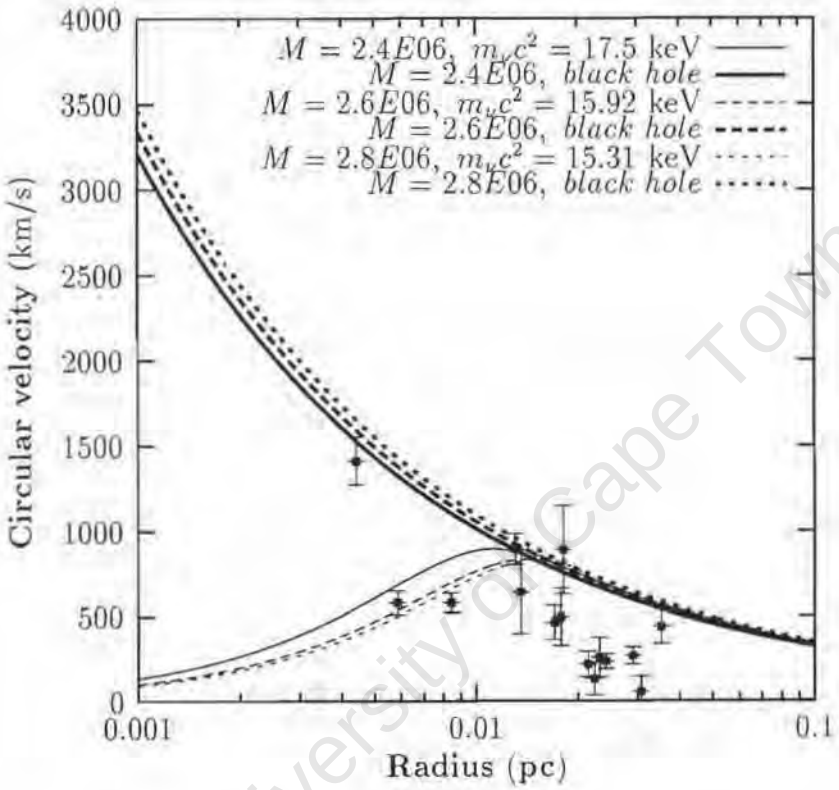

Figure 4.11: The circular velocity as a function of the distance from Sgr A* for BH and neutrino ball scenarios. The mass of the central object is varied as indicated on the graph. The data points with error bars of 15 stars in the central arcsec^2 are taken from ref. [28] assuming that the projected velocity and distance from Sgr A* are equal to the true velocity and distance, respectively. i.e. $z = 0$ and $v_z = 0$. This graph shows that the orbits of S0-1 are almost circular in the case of the BH scenario.

We now turn to the investigation of the dependence of the orbits on the z coordinate and z component of the velocity of the star S0-1. The two quantities z and v_z, are the major source of uncertainty in determining the exact orbit of the star S0-1. However, this shortcoming will not substantially affect the predictive power of our model, as we will see below. In Fig. 4.12 we show the results of a calculation of the dependence of the orbit on z for a $M = 2.6 \times 10^6 M_\odot$ neutrino ball or BH. The input values for v_x and v_y are fixed at 470 km/s, -1330 km/s, and v_z is assumed to be 0. The z-coordinate is varied from zero up to the radius of the neutrino ball, i.e. the distance from Sgr A* beyond which there is obviously no difference between the BH and the neutrino ball scenarios. In this case, the radius of the neutrino ball is 1.88×10^{-2} pc or 0.485″. The top panel represents the orbits in the case of a BH, for different values of z, while the lower panel describes the dependence of the orbit on z in the neutrino ball scenario. We conclude from this plot that, increasing $|z|$ has the effect of shifting the orbits towards the lower right corner of the graph. This is, obviously, due to the fact that increasing $|z|$ means going further away from the scattering center, thus yielding less deflection of the orbit. Moreover, in the neutrino ball scenario, the dependence on z is relatively insignificant, as long as $|z|$ is smaller than the radius of the neutrino ball. This is in accordance with the fact that for small distances from the center, the potential of a neutrino ball can be approximated by a harmonic oscillator-type potential, where the Newtonian equations of motion decouple in Cartesian coordinates. The dependence of the orbits of S0-1 on v_z has a similar effect as in the previous graph but, in this case, we have fixed z to zero and v_z has been varied as an input parameter. Increasing $|v_z|$ yields a greater velocity of the star and, obviously, a fast moving star will be deflected less than a star with smaller $|v_z|$. The results of this calculation are summarized in Fig. 4.13.

In Fig. 4.14 three orbits are plotted: the upper-leftmost orbit of S0-1 corresponding to the neutrino ball scenario (actually, line 9 of Fig. 4.8) and two orbits in a BH scenario with the smallest minimal and maximal distances from Sgr A* (ellipses 2 and 4 from Fig. 4.9).

If the star is found in the region F inside the ellipses, this will rule out both the BH and the neutrino ball scenario of Sgr A*, as seen in Fig. 4.14. We can estimate the minimal distance of approach to Sgr A* to be 0.909 light days. If the orbit of S0-1 ends up in the upper-left zone of the thick line, this will clearly rule out the neutrino ball scenario for the chosen neutrino mass. However, if S0-1 is found in the lower right corner of the same line (i.e. below the thick line), then the supermassive object can be interpreted as either a neutrino ball or a BH with a large z or v_z parameter.

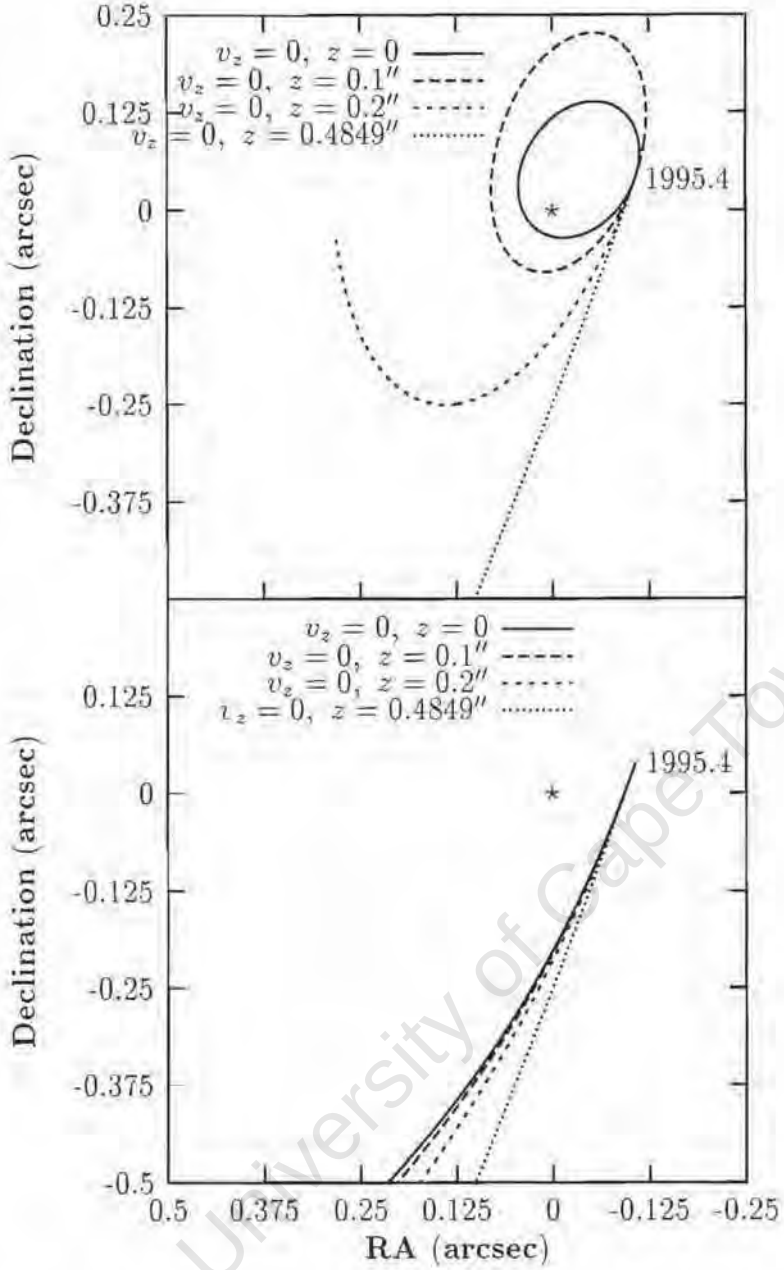

Figure 4.12: Projected orbits of the star S0-1 in the case of a supermassive BH (top panel) and in the case of a neutrino ball (lower panel) with $M = 2.6 \times 10^6 M_\odot$. In this graph we explore how the orbits are affected by the uncertainty in the z-parameter. The labels for the orbits are given in the graph. Note, that for $z = 0.4849''$, which corresponds to the radius of the neutrino ball for the assumed distance to the Galactic center, the orbits for a BH and neutrino ball are identical, as it should be. In this graph $v_x = 470$ km/s, $v_y = -1330$ km/s and $v_z = 0$.

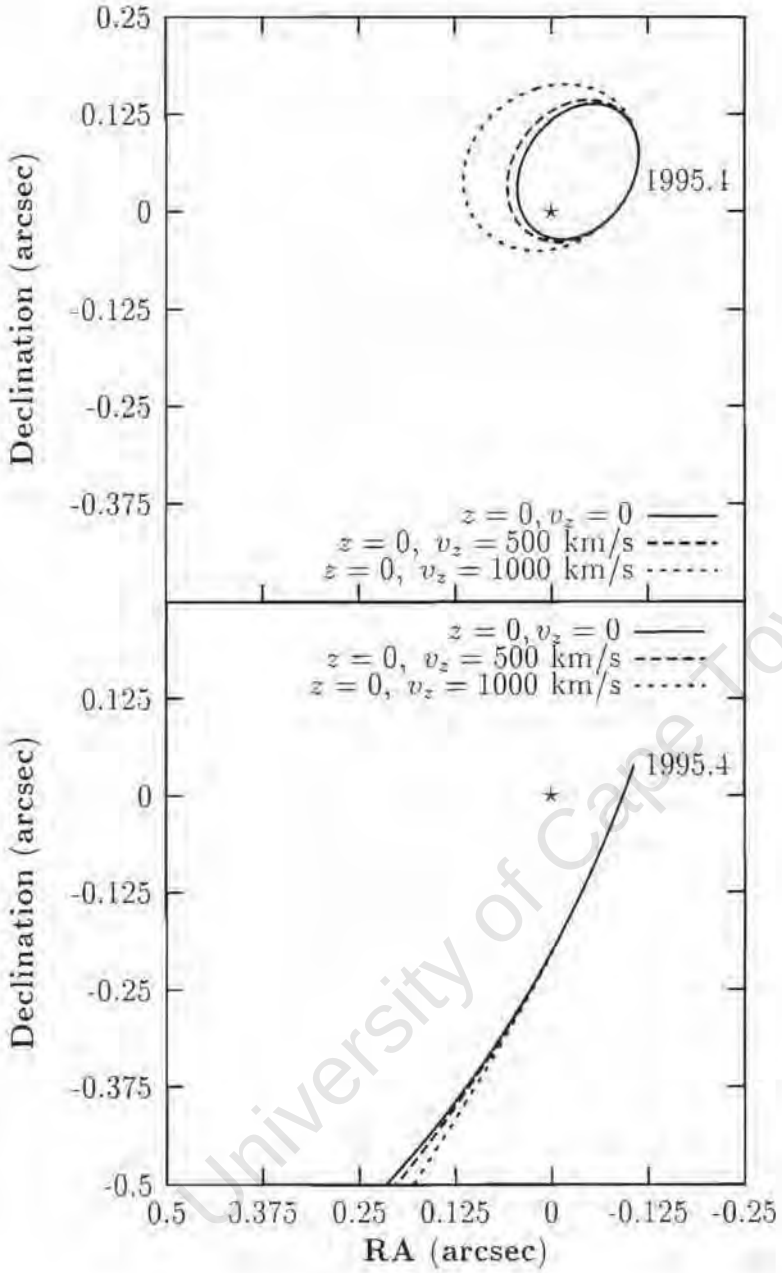

Figure 4.13: Projected orbits of the star S0-1 in the case of a supermassive BH (top panel) and in the case of a neutrino ball (lower panel) of $M = 2.6 \times 10^6 M_\odot$. In this graph we explore how the orbits are affected by the uncertainty in v_z. The labels for the orbits are given in the graph. Here, $v_x = 470$ km/s, $v_y = -1330$ km/s and $z = 0$.

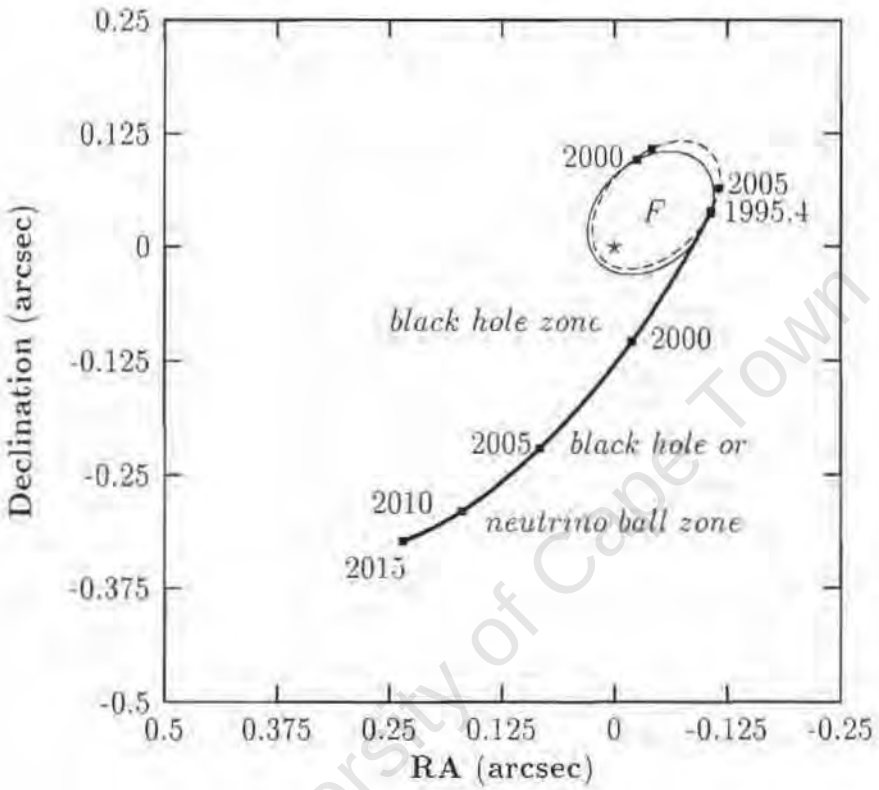

Figure 4.14: Prediction regions for the supermassive central object. This graph combines line 9 from Fig. 4.8 and lines 2 and 4 from Fig. 4.9. If the star S0-1 will be found inside the ellipses (region F), this will rule out both the BH and the neutrino ball models . If the star S0-1 will eventually be found in the upper-left zone of the graph, i.e. up and left of the thick orbit, this will rule out the neutrino ball interpretation for the chosen neutrino mass. Finally, if S0-1 will be found to the right and below the thick line, then the supermassive central object should be interpreted either as a BH with large z or as a neutrino ball.

4.4 Emission spectrum of the supermassive dark object

Here we calculate the emission spectrum of the compact dark object assuming that it is a supermassive degenerate neutrino ball (extended object) rather than a black hole . In the standard theory of steady and geometrically thin accretion disks, the power liberated in the disk per unit area is given by [140, 141]:

$$D(r) = -\frac{\dot{M}\Omega(r)\Omega'(r)r}{4\pi}\left[1-\left(\frac{R_i}{r}\right)^2\left(\frac{\Omega_i}{\Omega}\right)\right] , \tag{4.15}$$

where $\dot{M}$ characterizes the accretion rate parametrized as

$$\dot{M} = \dot{m}\dot{M}_{\rm Edd} . \tag{4.16}$$

Here $\dot{M}_{\rm Edd} = 2.21 \times 10^{-8} M$ yr^{-1} denotes the Eddington limit accretion rate and M is the total mass of the neutrino ball. The maximal and minimal accretion rates allowed by observations are $\dot{m} = 4 \times 10^{-3}$ and 10^{-4} [127] . The outer radius of the disk has been taken as 10^5 Schwarzschild radii, since for larger radii, the disk is unstable against self-gravity [127]. In the Eq. 4.15, Ω denotes the angular velocity of the accreting matter, R_i is the inner radius of the disk and Ω_i defines the angular velocity at the radius where $\Omega(r)$ has a maximum, $\Omega_i = \Omega(R_i)$. Finally the prime on the function $\Omega(r)$ denotes the derivative with respect to r. Since the motion of accreting matter in the bulk of the disk is Keplerian, the angular velocity Ω can be expressed as

$$\Omega = \sqrt{\frac{GM(r)}{r^3}}, \tag{4.17}$$

where $M(r)$ is the mass enclosed within a radius r of the neutrino ball and is given by Eq. (4.9). In Fig. 4.15, the angular velocity is plotted as a function of the distance from the center of the neutrino ball.

We now use Stefan Boltzmann's law, assuming that the gravitational binding energy is immediately radiated away

$$D(r) = \sigma T_{\rm eff}^4(r) , \tag{4.18}$$

where σ is the Stefan-Boltzmann constant. The effective temperature $T_{\rm eff}$ can be easily derived using the Eqs. (4.15)- (4.17) yielding

$$T_{\rm eff}(r) = \left(\frac{\dot{M}_{\rm Edd}GM_\odot}{8\pi\sigma a_\nu^3}\right)^{1/4} \dot{m}^{1/4}\left(\frac{3\,(v-v'x)-v^{3/2}x^{1/2}}{x^3}\right)^{1/4} \times\left[1-\left(\frac{x_i}{x}\right)^2\frac{\Omega_i}{\Omega}\right]^{1/4} . \tag{4.19}$$

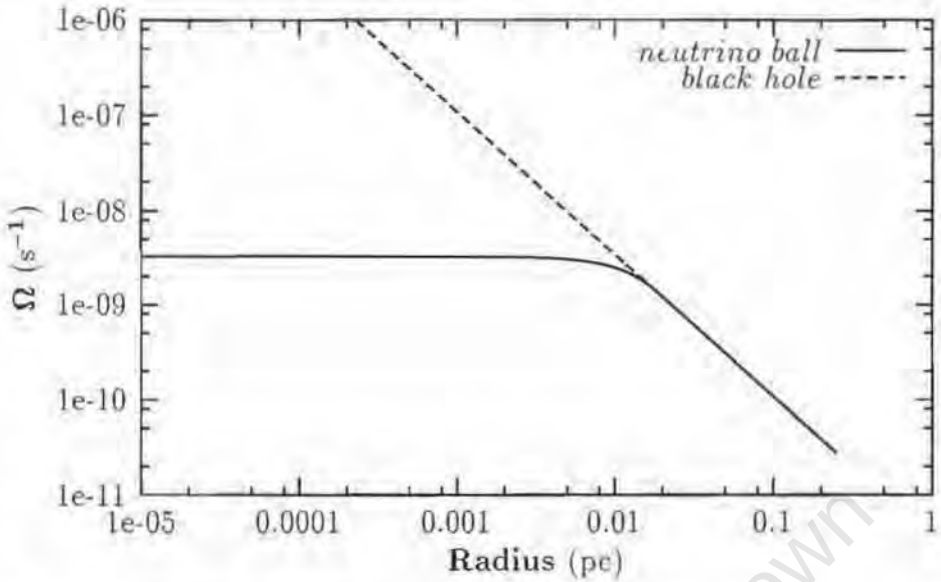

Figure 4.15: The angular velocity as a function of the distance from the center for both scenarios. The neutrino ball and the black hole have the same mass $M = 2.6 \times 10^6 M_\odot$.

Here, a_ν is the length scale which depends obviously on the neutrino mass and is given by Eq. (4.7). The function v is a solution of Lané-Emden equation .

Once the temperature distribution in the disk is specified, one can find its luminosity at a frequency ν using

$$\frac{dL_\nu}{dr} = \frac{16\pi^2 h\nu^3 \cos(i)}{c^2} \frac{r}{\exp\left(\frac{h\nu}{k_B T_{\rm eff}}\right) - 1} \ . \tag{4.20}$$

with the luminosity at the inner radius of the disk set equal to zero, i.e. $L_\nu(x_i) = 0$. In the last equation, h is Planck's constant, k_B denotes Boltzmann's constant and the disk inclination angle i is assumed to be 60^0 [127]. Picking up a particular value for ν, we have performed a numerical integration of the Eq. (4.20), taking the inner radius of the disk to be determined by $\Omega'(r) = 0$. However, the inner radius of the accreting disk can be chosen to be zero, as the inner region, where $\Omega(r)$ is nearly constant. does not contribute to the emission spectrum anyway. It is worthwhile to note, that in the case of a neutrino ball, there is no last stable orbit in contrast to the black hole case, where the inner radius of the disk is taken to be three Schwarzschild radii. The results of this integration are shown in Fig. 4.16, where the spectrum obtained in the case of an accretion onto a black hole (dotted lines) of $2.6 \times 10^6 M_\odot$ is shown as well. Here, accretion rates of $\dot{m} = 10^{-3}, 10^{-4}$ and 10^{-9} have been assumed for both scenarios.

In this plot, we have included the most up-to date observations of the Galactic centre and the data points are taken from ref. [127]. The arrows

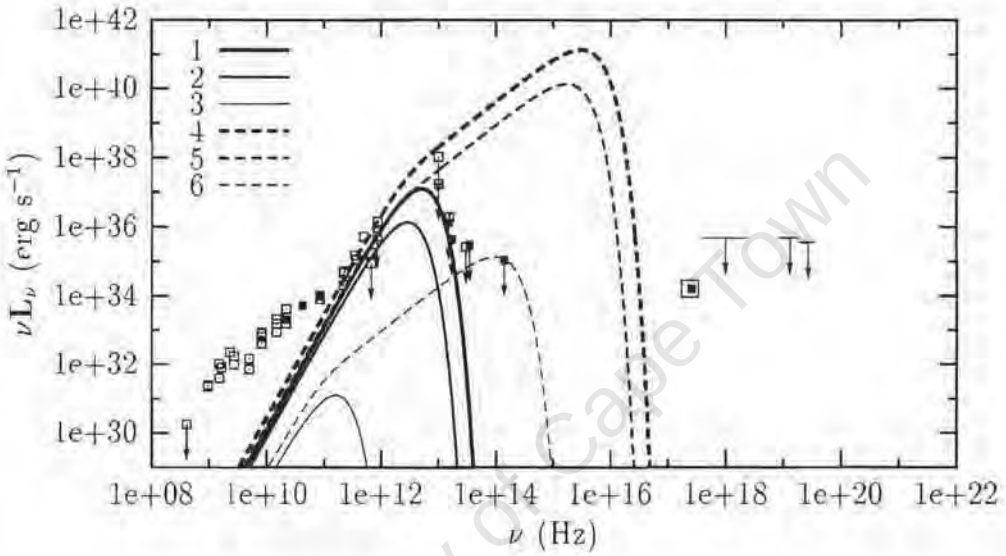

Figure 4.16: The spectrum of Sgr A* in both scenarios for different accretion rates. The solid curves (lines 1,2,3) correspond to a disk immersed in the potential of a neutrino ball while the dashed lines (lines 4,5,6) correspond to a disk immersed in the potential of a black hole. Lines 1 and 4 stand for an accretion rate of $\dot{m} = 10^{-3}$, while lines 2 and 5 have an accretion rate of $\dot{m} = 10^{-4}$. Finally, an accretion rate of $\dot{m} = 10^{-9}$ for a starving disk is represented by lines 3 and 6. The observed data points [127] have been included in this plot. The arrows denote upper bounds. The filled squares denote data with high resolution while the open circles represent the data with less resolution.

represent the upper limits, and the box at frequency $\sim 10^{17}$ Hz represents the uncertainty in the observed X-ray flux. The open and filled squares represent various flux measurements and upper limits of Sgr A*. The open squares represent the low angular resolution points while the filled ones represent the data points with best resolution. The observed spectrum rises at radio and submillimetre frequencies $\nu \simeq 10^9 - 10^{12}$Hz, where most of the emission occurs, and has a sharp drop in the infrared. The X-ray observations consist of a possible detection at soft X-ray energies, and firm upper limits in the hard X-rays. As seen in Fig. 4.16, the neutrino ball model reproduces the observed spectrum from the radio to the near infrared band very well. Thus, as our model fulfils two of the most stringent conditions, i.e. the mass distribution [28, 68] and the bulk part of the emitted spectrum, we conclude that the neutrino ball scenario is consistent with the currently available observational data. It is clear from Fig. 4.16 and also as pointed out in ref. [127], the curves corresponding to the black hole (lines 4. 5 and 6) provide a poor fit to the observational data. A starving black hole, with a an accretion rate of $\dot{m} = 10^{-9}$ (line 6 in Fig. 4.16) would not fit the observed spectrum either. Actually, this is the main reason why the standard accretion disk theory was abandoned as a possible candidate for the description of Sgr A* spectrum [117]. Fig. 4.17 shows the temperature in a disk as a function of the radius for an accretion rate of $\dot{m} = 10^{-3}$ in both scenarios.

In Fig. 4.18 we present the emission spectrum of Sgr A* with a neutrino ball mass at the Oppenheimer-Volkoff (OV) limit, i.e. $M_{\rm OV} = 2.6 \times 10^6 M_\odot$ and the neutrino mass is 491 keV/c^2. It is seen from this plot that the neutrino ball scenario at the OV limit is almost indistinguishable from the black hole scenario. These two scenarios differ only between 3 R_S and 4.4 R_S where R_S is the Schwarzschild radius corresponding to the mass $M_{\rm OV}$. The solid lines (1,2) correspond to a disk immersed in a neutrino ball at the OV limit while lines 3 and 4 are drawn for the case of a black hole of the same mass as the neutrino ball. Here, the accretion rate $\dot{m}$ has been taken to be 4×10^{-3} for lines 1 and 3 whereas lines 2 and 4 are drawn for $\dot{m} = 10^{-4}$.

The emission spectrum presented in Fig. 4.16 corresponds to a neutrino ball or black hole of $M = 2.6 \times 10^6 M_\odot$. To draw definite conclusions about the emission spectrum of a neutrino ball, it is necessary to investigate the dependence of the spectrum on i) the mass of the neutrino ball; ii) the neutrino mass m_ν, both with the ranges allowed by the currently available observational data [28]. In Fig. 4.19, we present the spectrum for different values of the neutrino ball masses, i.e. $M = 2.4, 2.6, 2.8 \times 10^6 M_\odot$. From this plot, we conclude that, within the uncertainties, the total mass of the neutrino ball has no significant effect on the spectrum of the neutrino ball. In Fig. 4.20. we plot the spectrum as a function of the neutrino mass for different accretion rates. The top panel represents the spectrum for an accretion rate of $\dot{m} = 10^{-4}$ while the lower describes an accretion rate of $\dot{m} = 10^{-3}$. As

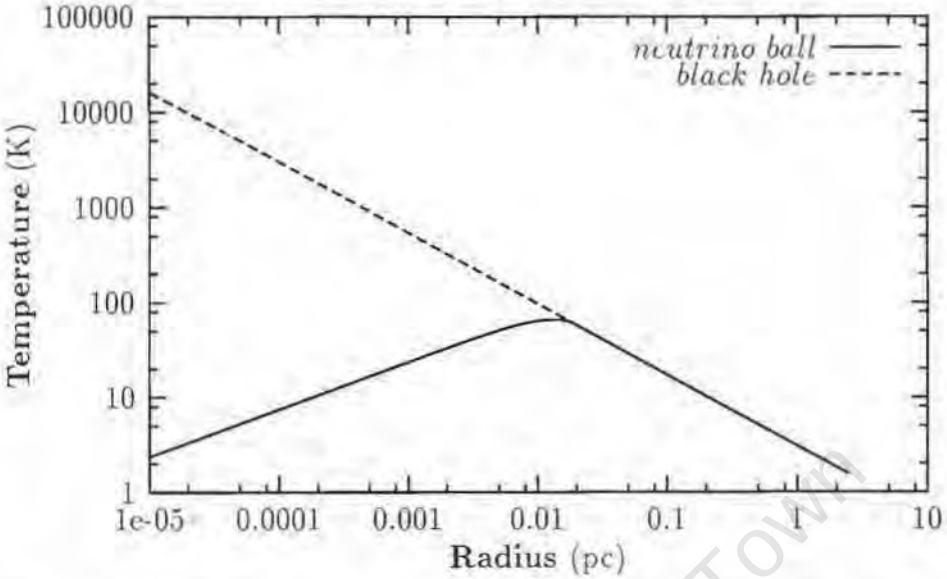

Figure 4.17: The temperature of the disk as a function of the distance from the center for both scenarios. The accretion rate is $\dot{m} = 10^{-3}$.

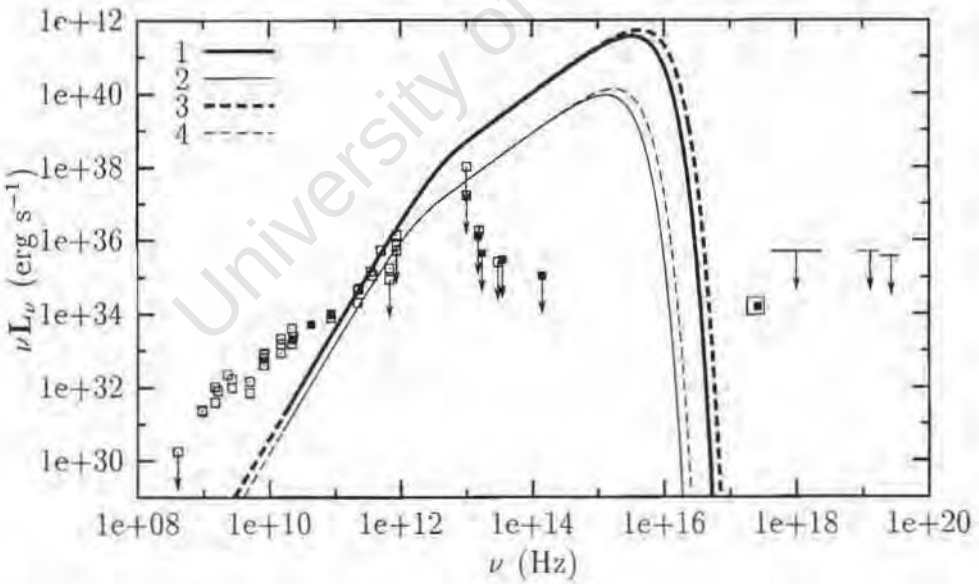

Figure 4.18: The Sgr A* emission spectrum for a neutrino ball of mass $M_{\rm OV} = 2.6 \times 10^6 M_\odot$ at the Oppenheimer-Volkoff limit (lines 1 and 2). The neutrino mass is 491 keV/c^2. The emission spectrum onto a black hole of the same mass as the neutrino ball is also shown (lines 3 and 4). The accretion rates of $\dot{m} = 4 \times 10^{-3}$ (lines 1 and 3) and $\dot{m} = 10^{-4}$ (lines 2 and 4) have been used.

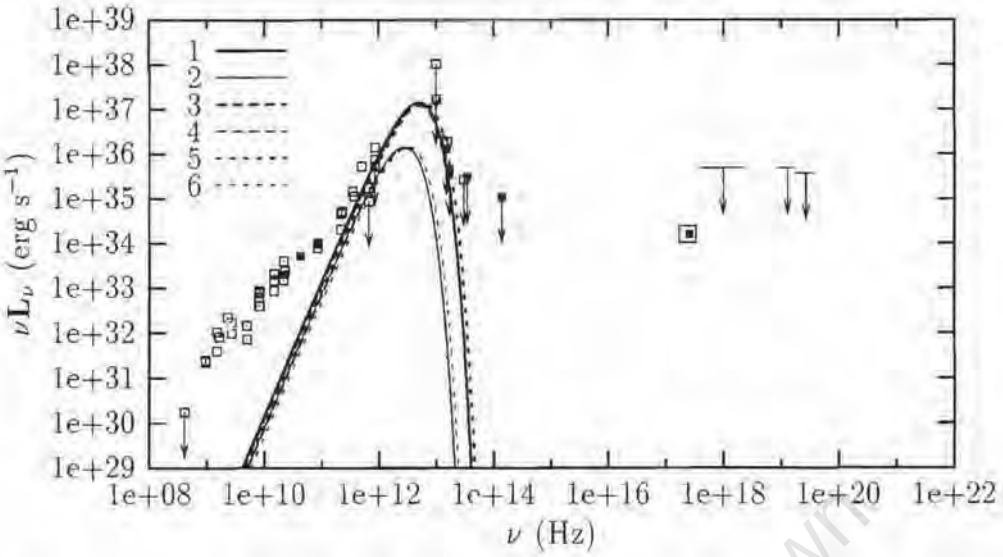

Figure 4.19: The Sgr A* emission spectrum as a function of the mass of the neutrino ball $M = 2.4, 2.6$ and 2.8×10^6 solar masses. The thick lines (1,3,5) correspond to $\dot{m} = 10^{-3}$ while the thin lines (2,4,6) are drawn for $\dot{m} = 10^{-4}$. The error bars in the total mass of the neutrino ball do not have a significant effect on the spectrum of Sgr A*.

the observed emission spectrum has a sharp drop in the infrared region, we require the theoretical spectrum not to extend to frequencies beyond the innermost data points of the infrared drop of the observed spectrum, yielding an upper bound for the neutrino mass. For each value of the accretion rate, an upper bound for the neutrino mass is obtained using that condition. This is reflected in Fig. 4.21, where we plot the neutrino mass, $m_\nu c^2$ as a function of the accretion rate $\dot{m}$. The vertical arrows pointing down show the inferred upper limits for the neutrino mass. For $\dot{m} = 10^{-4}$, the upper limit is $m_\nu c^2 \leq 25$ keV; For $\dot{m} = 8 \times 10^{-4}$, the range of the neutrino mass is $m_\nu c^2 \leq 16.6$ keV; For $\dot{m} = 10^{-3}$, the neutrino mass can be constrained to be $m_\nu c^2 \leq 15.92$ keV; and finally for $\dot{m} = 4 \times 10^{-3}$, the upper limit is found to be $m_\nu c^2 \leq 14$ keV. The horizontal line shows the lower limit on the neutrino mass obtained by fitting the mass distribution of the neutrino ball with the current observational data [28]. Combining both the upper and lower limits for the neutrino mass, we arrive at the following constraints for the neutrino mass

$$15.92 \text{ keV} \leq m_\nu c^2 \leq 25 \text{ keV for } \dot{m} = 10^{-4}, \tag{4.21}$$

$$15.92 \text{ keV} \leq m_\nu c^2 \leq 16.6 \text{ keV for } \dot{m} = 8 \times 10^{-4}. \tag{4.22}$$

From Fig. 4.21, we may conclude that i) in order to be consistent with the observational data [28], the accretion rate $\dot{m}$ onto the neutrino ball should

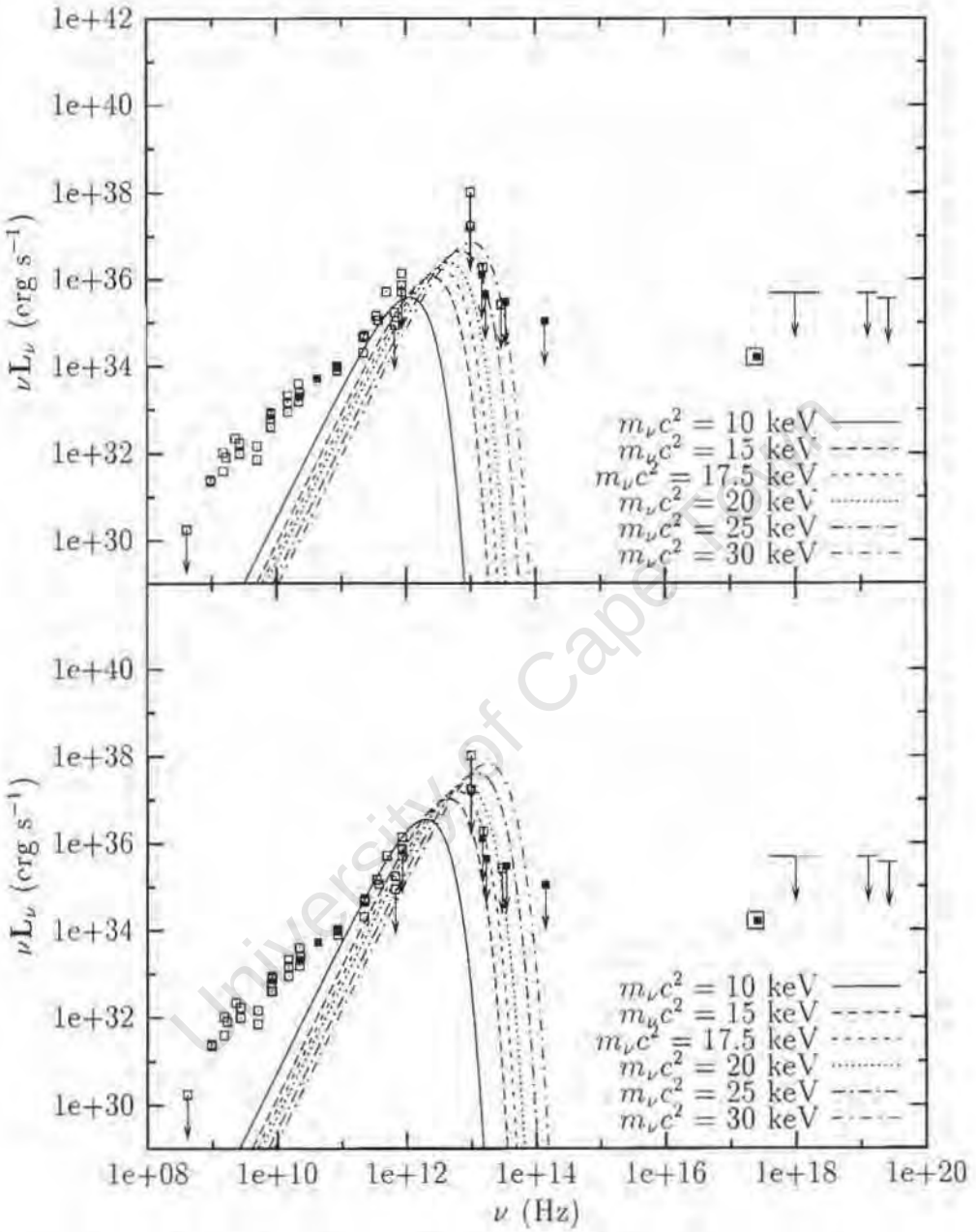

Figure 4.20: The Sgr A* emission spectrum as a function of the neutrino mass m_ν. The top panel corresponds to $\dot{m} = 10^{-4}$ while the lower one is plotted for $\dot{m} = 10^{-3}$. An upper limit for the neutrino mass is inferred by requiring that the theoretical spectrum cannot go beyond the innermost points of the infrared drop of the observed spectrum.

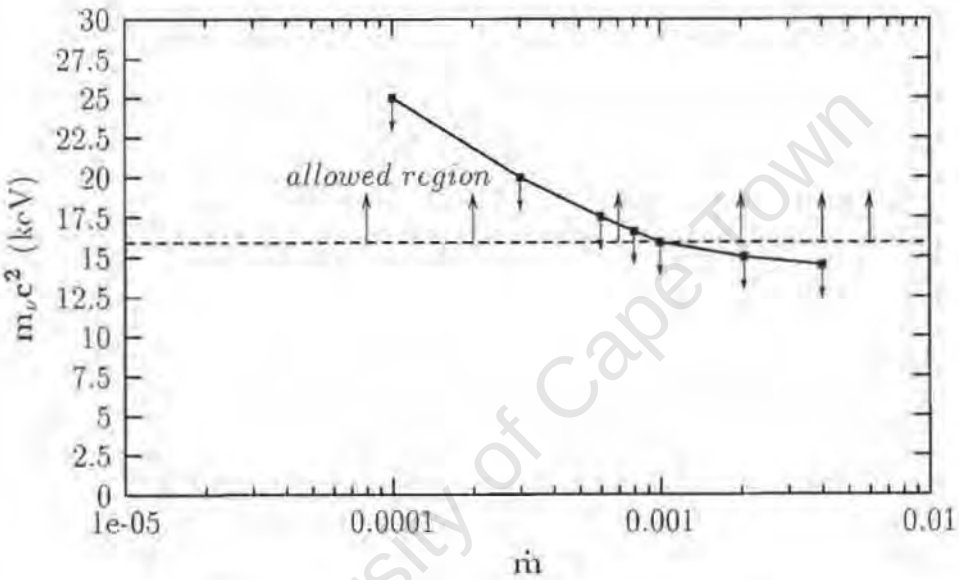

Figure 4.21: The neutrino mass m_ν as a function of the accretion rate $\dot{m}$. The horizontal line shows the lower limit from the dynamics of stars. The arrows pointing down show the upper limit from the drop of the spectrum in the infrared region of the observed spectrum. The range of the neutrino mass narrows as the accretion rate $\dot{m}$ increases. For $\dot{m} > 10^{-3}$, the upper limit on the neutrino mass becomes inconsistent with the lower limit from the dynamics of stars.

be less than $\sim 10^{-3}$ implying an accretion rate $\dot{M}$ onto the neutrino ball not more than $\sim 5.7 \times 10^{-5} M_{\odot}$ yr^{-1}. ii) The neutrino mass range is bounded from below by the Galactic kinematics and also bounded from above by the spectrum. The range of allowed values of the neutrino mass narrows as the accretion rate increases.

4.5 Conclusion

We have demonstrated that the orbits of S0-1 differ substantially for the BH and neutrino ball scenarios of the Galactic center, especially with the new data [28]. We have shown that using these data, both the error bars in velocities of S0-1 and mass of the central object do not change the pattern of the orbits of S0-1. In the case of a BH, the orbit of S0-1 is much more curved than in the neutrino ball scenario, as long as $|z|$ is lower than the radius of the neutrino ball. Increasing $|z|$ and $|v_z|$ shifts the orbits to the lower right corner of the graph, and due to this effect, we have established the allowed regions of S0-1 (see Fig. 4.14) depending on whether the Galactic center harbours a BH or a neutrino ball, *irrespective* of the values of the parameters z and v_z.

Fig. 4.14 serves as a test to distinguish the supermassive BH scenario from the neutrino ball model of the Galactic center and it is clear that, as the observations proceed within the next year, one might be able to tell the difference between the two models of the supermassive compact dark object at the center of our Galaxy.

We have studied the emission spectrum of Sgr A* assuming that it is a neutrino ball of mass $M = (2.6 \pm 0.2) \times 10^6 M_{\odot}$ and size of a few tens of light days. We have shown that in this case, the theoretical spectrum fits the observed points in the radio and infrared region of the spectrum much better than in the black hole scenario as seen from Fig. 4.16. In the neutrino ball scenario, the accreting matter experiences a much shallower gravitational potential than in the case of a black hole with the same mass, and therefore less viscous torque will be exerted. Here, we note that the emitting region for this region of the spectrum is of the order of the size of the neutrino ball, i.e. a few tens of light days. By a considering the emission spectrum due to a neutrino ball at the OV limit of mass of $2.6 \times 10^6 M_{\odot}$, we have shown that the neutrino ball and the black hole scenarios become almost indistinguishable. We have shown that the error bars in the total mass of the neutrino ball have practically no significant effect on the spectrum of Sgr A*. By assuming that the emitted spectrum cannot go beyond the observed innermost data points in the infrared drop of the Sgr A* spectrum, we have shown that the range of possible values of the neutrino mass narrows as the accretion rate $\dot{m}$ increases. We have also established that an accretion rate of more than $\dot{M} > 5.7 \times 10^{-5} M_{\odot} \mathrm{yr}^{-1}$ would render the possible range of the neutrino mass

inconsistent with the lower limit obtained from the observational data based on the kinematics of stars.

The thin accretion disk neutrino ball scenario alone can, of course, neither explain the lower part of the radio-spectrum, i.e. $\nu \lesssim 2 \times 10^{11}$ Hz nor can it explain the spectrum for $\nu \gtrsim 10^{14}$ Hz. The latter is a consequence of the fact that, the escape velocity from the center of the neutrino ball of $2.6 \times 10^6 M_\odot$ is only about 1700 km/s. In order to get X-rays, the particles need to reach a sizable fraction of the velocity of light, which would be impossible in the scenario of a pure neutrino ball. However, as the heavy neutrinos presumably decay radiatively ($\nu_\tau \rightarrow \nu_\mu + \gamma$ or $\nu_\tau \rightarrow \nu_e + \gamma$) with a lifetime of $\gtrsim 10^{18}$ yr (assuming Dirac neutrinos and the current limits for the mixing angles), there will be some X-ray emission of the order of $\lesssim 10^{34}$erg s^{-1} at an energy of $m_\nu c^2/2$. Moreover, if both neutrinos and antineutrinos are present in the neutrino ball, annihilation ($\nu_\tau + \bar{\nu}_\tau \rightarrow \gamma + \gamma$) will also contribute to the X-ray spectrum at an energy $m_\nu c^2$, concentrated at the center of the neutrino ball, albeit with a much smaller luminosity [36]. Furthermore, by considering a scenario with a much more compact star at the Galactic center surrounded by a neutrino ball of $2.6 \times 10^6 M_\odot$, one might be able to explain the full observed spectrum of Sgr A*. The compact object at the Galactic center may be a neutron star. A similar idea was proposed [142], where the radio emission of Sgr A* was identified to be due to an otherwise unobservable radio pulsar. However, as the accretion rate onto the neutrino ball is of the order of $\dot{M} = 10^{-5} M_\odot$ yr^{-1} in such scenario, i.e. 3 orders of magnitude larger than the Eddington accretion rate of $\sim 10^{-8} M_\odot$ yr^{-1} onto a neutron star, much of the the baryonic matter falling towards the neutron will have to be expelled before reaching the neutron star surface.

Chapter 5

Summary

In this thesis, we have investigated degenerate neutrino balls and have shown that these objects might have important astrophysical implications. Neutrinos in the mass window of 10 to 25 keV/c^2 are quite unique as they might form supermassive degenerate neutrino balls and degenerate neutrino halos around ordinary stars.

By considering neutrino halos around the sun, we have established the upper bound on the neutrino mass in order to be consistent with the observed mass excesses within the orbits of various outer planets, as obtained from Voyager and Pioneer 10/11. Within Neptune's orbit, the bound on the neutrino mass is $m_\nu c^2 \leq 17$ keV for $g_\nu = 2$ and $m_\nu c^2 \leq 14.3$ keV for $g_\nu = 4$. The mass of degenerate neutrino matter would be a few times $10^{-6} M_\odot$ within Neptune's orbit and is consistent with the observations. We have shown that the perihelion shifts due to an assumed neutrino halo are negative in contrast to the general relativistic ones which are positive. In addition, the planetary perihelion shifts due to a neutrino halo depend only on the eccentricity while those due to general relativistic effects depend on the eccentricity and the semi-major axis of the planet. In order to be consistent with the experimental data on the perihelion shifts of Icarus, the constraints on the neutrino mass have been established $m_\nu c^2 \leq 16.4$ keV for $g_\nu = 2$ or $m_\nu c^2 \leq 13.8$ keV for $g_\nu = 4$. We have also shown that if a neutrino halo exists around the sun, it cannot be heavier than $\sim 100 M_\odot$. It has also been shown that there is a solution with a mass of about 3 $M_\odot$ and a maximal size of a few light years.

We have studied the general relativistic effects on degenerate neutrino balls and have shown that the Tolman-Oppenheimer Volkoff equations admit a solution with a maximum mass called the Oppenheimer-Volkoff limit. For a neutrino mass in our interesting range of 10 to 25 keV/c^2, the Oppenheimer-Volkoff limit is of the order of a few times $10^9 M_\odot$ which is the upper limit for the purported black holes at the galactic centers. Assuming that the most massive dark object at the center of M87 is a neutrino ball of mass $M \simeq 3 \times 10^9 M_\odot$ at the Oppenheimer-Volkoff limit, a neutrino mass range

has been established 12.4 keV $\leq m_\nu c^2 \leq$ 16.5 keV for $g_\nu = 2$, or 10.4 keV $\leq m_\nu c^2 \leq$ 13.9 keV for $g_\nu = 4$. The supermassive dark object of mass $M = 2.6 \times 10^6 M_\odot$ at the Galactic center could be a a neutrino ball rather than a black hole. The upper limit for the size of the dark object provides us with a lower limit for the neutrino mass, i.e. $m_\nu c^2 \geq 15.9$ keV for $g_\nu = 2$ and $m_\nu c^2 \geq 13.4$ keV for $g_\nu = 4$. We have shown that a neutrino ball at the Oppenheimer-Volkoff limit differs very slightly from a black hole of the same mass as its radius is only ~ 4.4 times the Schwarzschild radius corresponding to the mass of the neutrino ball. A neutrino ball of $2.6 \times 10^6 M_\odot$ with a radius of 1.88×10^{-2}pc or 22.1 ld is consistent with the most recent recent observations at the Galactic center for the chosen neutrino mass. Comparing all the bounds on the neutrino mass, i.e. Eqs. (2.61), (2.68), (2.85) and (3.25), we conclude that a neutrino mass range 15.9 keV $\leq m_\nu c^2 \leq$ 16.4 keV for $g_\nu = 2$, or 13.4 keV $\leq m_\nu c^2 \leq$ 13.8 keV for $g_\nu = 4$, is consistent with all reliable data. Of course, the lower limit of neutrino mass strongly depends on the size of the central object at the Galactic center. For a size of 0.016 pc, the lower limit on the neutrino mass could be as 14.35 keV/c^2 for $g_\nu = 2$ and 12.07 keV/c^2 for $g_\nu = 4$.

We have investigated the detailed properties of degenerate neutrino halos around compact stars using the general relativistic Tolman-Oppenheimer Volkoff equations of hydrostatic equilibrium. We have found that that there is always a maximal mass and radius of the compact star within a neutrino halo of a given mass. For a fixed mass of the compact star, the neutrino ball will have a maximum radius which obviously depends on the mass of the compact star. In addition, the neutrino halo will have an Oppenheimer Volkoff mass limit that is equal to the one in the pure case (without a compact star). Here, the compact star might be a white dwarf, a neutralino (neutron) star, or even a baryonic star of constant density. For neutralinos masses between 4.22 MeV and 1.25 GeV, neutralino stars could mimic the properties of "machos". We have calculated the escape and circular velocities of baryonic matter falling onto a compact star surrounded by a neutrino ball of mass $M = 2.6 \times 10^6 M_\odot$. In the case of a neutron star at the center of the neutrino ball, the escape velocity from the center of the neutron star can reach a half the velocity of light.

We have shown that the supermassive dark object of $\sim 2.6 \pm 10^6 M_\odot$ at the Galactic center could be an extended object rather than a black hole. This has been achieved by investigating the orbits of the fast moving star S1 (S0-1) in the black hole or neutrino ball scenarios of the supermassive dark object. We have shown that using the most recent data on the dynamics of stars around the Galactic center. the orbit of S0-1 is much curved in the black hole scenario than in the neutrino ball scenario. By investigating the orbits dependence on error bars in velocities and mass of the central object, and also on uncertainties in z and v_z, we have established that within a few

years, the orbit of S0-1 may indeed reveal the nature of the supermassive compact dark object at the Galactic center.

Assuming that the compact dark object at the Galactic center is a neutrino ball (extended object) of $M = (2.6 \pm 0.2) \times 10^6 M_\odot$ rather than a black hole, we have studied the emission spectrum of Sgr A*. We have shown that the neutrino ball scenario has the advantage that it could explain naturally the observed radio and infrared emission spectrum of the Galactic center for wavelengths between $\lambda = 0.3$ cm and $\lambda = 10^{-3}$ cm, if the neutrino mass and the accretion rate fulfil some constraints. We have established that by restricting the theoretical spectrum to innermost data points of the infrared drop of observed spectrum, the neutrino mass becomes dependent on the accretion rate and there is an upper limit on the neutrino mass for each value of the accretion rate. For an accretion rate $\dot{m} > 10^{-3}$, the constraints on the neutrino mass become inconsistent with the lower limit obtained from the size of the central object. The maximum accretion rate onto the neutrino ball would be $\dot{M} = 5.7 \times 10^{-5} M_\odot$ yr^{-1}. The neutrino ball scenario cannot explain the lower part of the radio-spectrum, i.e. $\nu \lesssim 2 \times 10^{11}$Hz nor can it explain the emission spectrum at $\nu \gtrsim 10^{14}$ Hz as the escape velocity from the center of the neutrino ball of $M = 2.6 \times 10^6 M_\odot$ is only about 1700 km/s. A much more compact object seems to be unavoidable at the center of the neutrino ball in order to explain the full observed spectrum at the Galactic center. This compact object might be a neutron star.

In table 1, we summarize all the constraints on the neutrino mass m_ν as discussed in various chapters of this thesis.

Object	neutrino mass
Neptune	$m_\nu c^2 \leq 17$ keV
Jupiter	12.8 keV $\leq m_\nu c^2 \leq 14.2$ keV
Icarus	$m_\nu c^2 \leq 16.4$keV
Sgr A*	$15.9 \leq m_\nu c^2 \leq 25$ keV
M87	$12.4 \leq m_\nu c^2 \leq 16.5$ keV

Table 5.1: Neutrino mass range for $g_\nu = 2$. The corresponding neutrino mass values for $g_\nu = 4$ are obtained by multiplying the values for $g_\nu = 2$ by a factor of $2^{-0.25}$.

Appendix A

Lané-Emden equation

The Lané-Emden equation is obtained as a result of three main equations: i) the Poisson's equation

$$\Delta\Phi = 4\pi G\rho; \tag{A.1}$$

ii) the equation of hydrostatic equilibrium

$$\frac{dP}{dr} = -\rho\frac{d\Phi}{dr}; \tag{A.2}$$

and iii) the polytropic equation of state

$$P = K\rho^{\frac{n+1}{n}}. \tag{A.3}$$

In the equations (A.1), (A.2) and (A.3), Φ stands for the gravitational potential of the self-gravitating gas, ρ denotes its mass density, P denotes the gas the pressure, K is the polytropic constant and n is the polytropic index. Assuming spherical symmetry, equation (A.1) can be rewritten as

$$\frac{1}{r^2}\frac{d}{dr}\left(r^2\frac{d\Phi}{dr}\right) = 4\pi G\rho. \tag{A.4}$$

Using the equation of hydrostatic equilibrium (A.2), the Poisson's equation (A.1) can be transformed to

$$\frac{1}{r^2}\frac{d}{dr}\left(\frac{r^2}{\rho}\frac{dP}{dr}\right) = -4\pi G\rho. \tag{A.5}$$

Introducing new dimensionless variables

$$x = \frac{r}{a}, \quad \rho = \rho_0\Theta^n, \tag{A.6}$$

with

$$a = \sqrt{\frac{(n+1)K}{4\pi G}\rho_0^{\frac{1}{n}-1}}, \tag{A.7}$$

where ρ_0 is the central density. The Poisson's equation (A.5) can be simplified to the form

$$\frac{1}{x^2}\frac{d}{dx}\left(x^2\frac{d\Theta}{dx}\right) = -\Theta^n, \tag{A.8}$$

with the following initial conditions on the function Θ

$$\Theta(0) = 1 \quad \text{and} \quad \Theta'(0) = 0, \tag{A.9}$$

obtained from the condition that the density $\rho(r)$ has a maximum value $\rho(0) = \rho_0$ at the center of the gas sphere. Equation (A.8) is known as the Lané-Emden equation with polytropic index n. Its solution is called the n-th Emden function and is denoted by Θ_n. Instead of using the function Θ, one could introduce the reduced function $v = x\Theta$. The equation for v takes the following form

$$\frac{d^2v}{dx^2} = -\frac{v^n}{x^{n-1}}. \tag{A.10}$$

with

$$v(0) = 0 \quad \text{and} \quad v'(0) = 1. \tag{A.11}$$

The function v plays the role of the dimensionless potential used in this thesis. The Lané-Emden equation (A.10) as well as other nonlinear differential equations in this thesis have been solved using fifth order adaptive stepsize control for Runge-Kutta [143]. In the case of n=3/2, we recover the equation of state of a cold Fermi Fermi gas, i.e.

$$P = K\rho^{5/3}, \tag{A.12}$$

with $K = (6/g)^{2/3}(\pi^{4/3}\hbar^2)/(5m^{8/3})$, m being the mass of the gas particles, and v satisfies the equation

$$\frac{d^2v}{dx^2} = -\frac{v^{3/2}}{x^{1/2}}, \tag{A.13}$$

An other interesting case corresponds to $n = 3$, and we recover the equation of state of a relativistic degenerate Fermi gas [92], i.e.

$$\rho = K\tilde{n}^\gamma \quad \text{and} \quad P = c^2(\gamma - 1)\rho. \tag{A.14}$$

Here $\gamma = 4/3$, $\tilde{n}$ is the gas number density, ρ is the mass-energy density , and the constant $K = 1/4 \times (3^{4/3}\pi^{2/3}) \times \hbar G/c^3$.

Let us point us that near the origin, Emden's function Θ with index n has the expansion [144]

$$\Theta = 1 - \frac{1}{3!}x^2 + \frac{n}{5!}x^4 - \frac{8n^2 - 5n}{3.7!}x^6 + \cdots . \tag{A.15}$$

Using the relation between v and Θ, we arrive at the following expansion for the normalized function v

$$v = x\Theta(x) = x - \frac{1}{3!}x^3 + \frac{n}{5!}x^5 - \frac{8n^2 - 5n}{3.7!}x^7 + \cdots . \tag{A.16}$$

Appendix B

Elliptic integrals

We have dealt with elliptic integrals [145] in chapter 2. Here we just provide some useful relations that have been used. An elliptic integral of first kind is defined as

$$F(\pi/2,k)=\int_0^{\pi/2}\frac{d\varphi}{\sqrt{1-k^2sin^2\varphi}}, \tag{B.1}$$

while

$$E(\pi/2,k)=\int_0^{\pi/2}\sqrt{1-k^2sin^2\varphi}d\varphi, \tag{B.2}$$

is known as an elliptic integral of second kind. In order to differentiate these elliptic integrals, the following rules apply

$$\frac{dE}{dk}=\frac{E(k)-F(k)}{k}, \tag{B.3}$$

$$\frac{dF}{dk}=\frac{E(k)}{kk'^2}-\frac{F(k)}{k}, \quad k'^2=1-k^2. \tag{B.4}$$

For small values of the argument k, the elliptic integrals $F(k)$ and $E(k)$ have the following expansions

$$F(k)=\frac{\pi}{2}\left(1+\frac{1}{4}k^2+\frac{9}{64}k^4+\frac{25}{256}k^6+\cdots\right), \tag{B.5}$$

$$E(k)=\frac{\pi}{2}\left(1-\frac{1}{4}k^2-\frac{3}{64}k^4-\frac{5}{256}k^6-\cdots\right). \tag{B.6}$$

Appendix C

Orbit of S0-1 in the neutrino ball scenario

The orbits of S0-1 have been investigated in chapter 4. Here, we just provide the full solution of the equations of motion (4.1),(4.2) and (4.3) in the neutrino ball scenario. A part of this orbit has been plotted in Fig. 4.5. In the case of the neutrino ball, the orbit of S0-1 is bound but not closed as it can be seen from Fig. C.1.

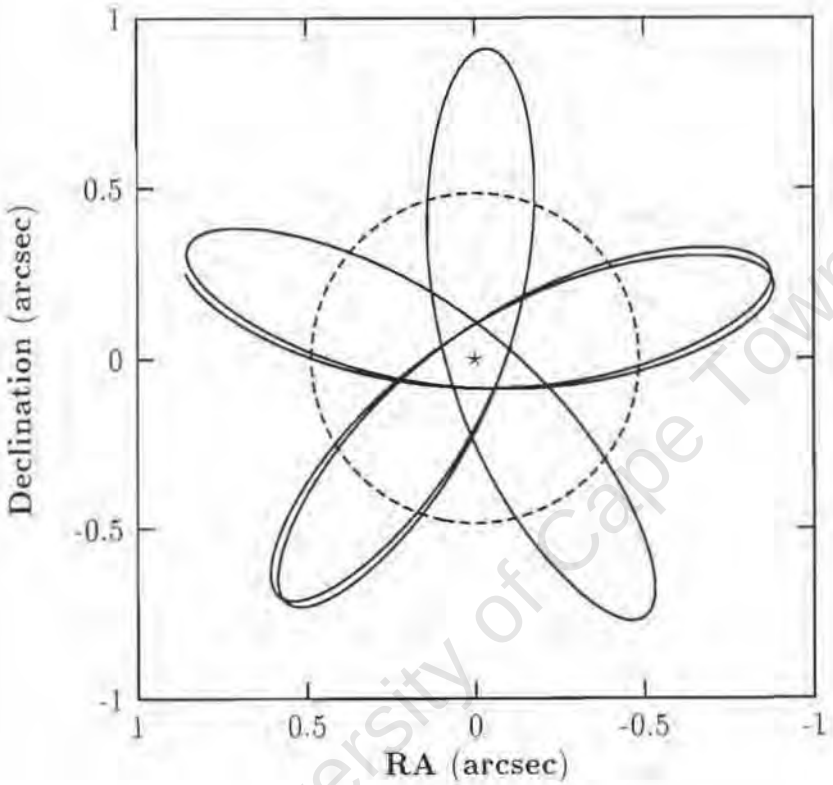

Figure C.1: The orbit of S0-1 in the neutrino ball scenario. The input values are $v_x = 470$ km/s, $v_y = -1330$ km/s, RA $= -0.107''$, DEC $= 0.039''$ and $v_z = z = 0$. The neutrino ball has a mass $M = 2.6 \times 10^6 M_\odot$. The orbit of S0-1 is bound but not closed with a minimal distance and maximal distances from Sgr A* of 3.98 ld and 12.07 ld, respectively. The dashed line represents the neutrino ball surface and the star denotes the center of the coordinate system. The radius of the neutrino ball is found to be $R = 0.4849''$ or $R = 22.4$ ld.

Bibliography

[1] S. M. Faber and J. S. Gallagher, Ann. Rev. Astron. Astrophys. **25**, 135 (1979).

[2] V. Trimble, Ann. Rev. Astron. Astrophys. **25**, 425 (1987).

[3] C. J. Copi, D. N. Schramm, and M. S. Turner, Science **267**, 192 (1995).

[4] J. H. Oort, Bull. Astron. Inst. Netherlands **6**, 242 (1932).

[5] F. Zwicky, Helv. Phy. Acta **6**, 110 (1933).

[6] P. J. E. Peebles, *Principles of Physical Cosmology* (Princeton University Press, Princeton, 1993).

[7] G. Raffelt , in *The Evolution of the Universe*, ed. G. Börner & S. Gottlöber (Dahlem Workshop Report ES 19; New York; Wiley,1995).

[8] M. Milgrom, ApJ **270**, 365 (1983).

[9] R. H. Sanders , A&A Rev. **2**, 1 (1990).

[10] S. M. Kent , ApJ **93**, 816 (1987).

[11] M. Milgrom , ApJ **333**, 689 (1988).

[12] K. G. Begeman, A. H. Broeils, and R. H. Sanders, MNRAS **249**, 523 (1991).

[13] M. Milgrom , Ann. Phys. **229**, 384 (1994).

[14] M. Milgrom, ApJ **496**, L89 (1998).

[15] V. V. Zhytnikov and J. M. Nestor, Phys. Rev. Lett. **73**, 2950 (1994).

[16] P. D. Mannheim, ApJ **479**, 659 (1997).

[17] J. D. Benkenstein and R. H. Sanders, ApJ **429**, 480 (1994).

[18] Particle Data Group, C. Saso *et al.*, Eur. Phys. J. **C3**, 1 (1998).

[19] M. Gell-Mann, P. Ramond, and R. Slansky, in *Supergravity*, edited by F. van Nieuwenhuizen and D. Freedman (North Holland, Amsterdam, 1979).

[20] T. Yanagida, *Proceedings of the Workshop on Unified Theory and the Baryon Number of the Universe* (KEK, Japan, 1979).

[21] Y. Suzuki, Superkamiokande Collaboration, Talk presented at *17th International Workshop on Weakly Interactions and Neutrinos (WIN99)*, Cape Town, January 24-30, 1999, World Scientific, Singapore 1999.

[22] J. Kormendy and D. Richstone, Ann. Rev. Astron. Astrophys. **33**, 581 (1995).

[23] J. Kormendy *et al.*, ApJ. **459**, L57 (1996).

[24] M. Myoshi *et al.*, Nature **373**, 127 (1995).

[25] F. Macchetto *et al.*, ApJ. **489**, 579 (1997).

[26] R. Genzel and C. H. Townes. Ann. Rev. Astron. Astrophys. **25**, 377 (1987).

[27] A. Eckart and R. Genzel, Nature **383**, 415 (1996).

[28] A. M. Ghez, B. L. Klein, M. Morris, and E. E. Becklin, ApJ **509**, 678 (1998).

[29] M. Morris, Nature **383**, 389 (1996).

[30] N. Bilić, D. Tsiklauri, and R. D. Viollier, Prog. Part. Nucl. Phys. **40**, 17 (1998) .

[31] D. Tsiklauri and R. D. Viollier, ApJ **500**, 591 (1998).

[32] D. Tsiklauri and R. D. Viollier, Astropart. Phys. to be published, astro-ph/9805272.

[33] J. F. Navarro, C. S. Frank, and S. D. M. White, ApJ **462**, 563 (1996).

[34] KARMEN Collaboration, R. Maschuw , Talk at *17th International Workshop on Weak Interactions and Neutrinos (WIN99)*, Cape Town, South Africa, 24-30 January 1999, astro-ph/9906004, World Scientific, Singapore, 1999.

[35] C. Athanassopoulos *et al.*, Phys. Rev. Lett. **77**, 3022 (1996); Phys. Rev. **C54**, 2685 (1996).

[36] R. D. Viollier, Progr. Part. Nucl. Phys. **32**, 51 (1994).

[37] N. Bilić and R. D. Viollier, Nucl. Phys. (Proc. Suppl.) **B66**, 256 (1998).

[38] E.W. Kolb and M.S. Turner, Phys. Rev. Lett. **67**, 5 (1991) .

[39] N. Bilić, F. Munyaneza, and R. D. Viollier, Phys. Rev. **D59**, 024003 (1999) .

[40] D. Lurie, G. B. Tupper, and R. D. Viollier, in *Proceedings of the Symposium in Honor of J. D. Walecka 's Sixtieth Birthday*, CEBAF, Newport News, Va., edited by W. W. Buck *et al.*, (World Scientific, Singapore, 1993), p. 105 .

[41] R. J. Lindebaum, G. B. Tupper, and R. D. Viollier, Talk presented at *17th International Workshop on Weak Interactions and Neutrinos (WIN99)*, Cape Town, South Africa, 24-30 January 1999, astro-ph/9906004, World Scientific, Singapore, 1999.

[42] N. Bilić and R. D. Viollier, Phys. Lett. **B408**, 75 (1997) .

[43] N. Bilić and R. D. Viollier, Gen. Rel. Grav. to be published, gr-qc/9706019.

[44] N. Bilić and R. D. Viollier, Eur. Phys. J. **C** to be published, hep-ph/9809563.

[45] R. D. Viollier, F. R. Leimgruber, and D. Trautmann, Phys. Lett. **B297**, 132 (1992).

[46] R. D. Viollier, D. Trautmann, and G. B. Tupper, Phys. Lett. **B306**, 79 (1993).

[47] F. Munyaneza and R. D. Viollier, ApJ submitted, astro-ph/9910566

[48] R. M. Barnett *et al.*, Phys. Rev. **D51**, 1 (1996).

[49] H. E. Haber and G.L. Kane, Phys. Rep. **117**, 75 (1985).

[50] G. Farrar, Phys. Rev **D51**, 3904 (1995); E.W. Kolb and A. Riotto, *Phys. Rev.* **D54**, 3722 (1996).

[51] G. Farrar and E.W. Kolb, Phys. Rev. **D53**, 2990 (1996).

[52] MACHO collaboration, C. Alcock *et al.*, ApJ **486**, 697 (1997) .

[53] Planet Collaboration, M. D. Albrow *et al.*, ApJ to be published, astro-ph/9807086.

[54] L. C. Ho, Invited review paper to appear in Observational Evidence for Black Holes in the Universe, ed. S.K. Chakrabarti (Dordrecht: Kluwer 1998), astro-ph/9803307.

[55] Ya. B. Zeldovich and I. D. Novikov, Sov. Phys. Dokl. **158**, 811 (1964).

[56] E. E. Salpeter, ApJ **140**, 796 (1964).

[57] D. Lynden-Bell, Nature **223**, 690 (1969) .

[58] M. J. Rees, ARA&A **22**, 471 (1984).

[59] J. Kormendy and D. Richstone, ARA&A **33**, 581 (1995) .

[60] E. Maoz, ApJ **494**, L181 (1998) .

[61] J. W. Haller, M. J. Rieke, G. H. Rieke, P. Tamblyn, L. Close, and F. Melia. ApJ **456**, 194 (1996) .

[62] R. H. Sanders, Nature **359**, 131 (1992) .

[63] E. Maoz, ApJ **447**, L91 (1995).

[64] D. Tsiklauri and R. D. Viollier, MNRAS **282**, 1299 (1996).

[65] D. Tsiklauri and R. D. Viollier, ApJ **501**, 186 (1998).

[66] A. Eckart and R. Genzel, MNRAS **284**, 576 (1997).

[67] R. Genzel, N. Thatte, A. Krabbe, H. Kroker, and L. E. Tacconi-Garman, ApJ **472**, 153 (1996) .

[68] R. Genzel, A. Eckart, T. Ott, and F. Eisenhauer, MNRAS **291**, 219 (1997) .

[69] F. Munyaneza and R. D. Viollier, MNRAS submitted, astro-ph/9907318.

[70] J. J. Binney and S. C. Tremaine, *Galactic Dynamics* (Princeton: Princeton Univ. Press 1987) .

[71] F. Munyaneza, D. Tsiklauri, and R. D. Viollier, ApJ **509**, L105 (1998).

[72] F. Munyaneza, D. Tsiklauri. and R. D. Viollier, ApJ **526**, to be published, astro-ph/9903242.

[73] J. H. Lane, Amer. J. Sci. **50**, 57 (1870).

[74] R. Emden , **Gaskugeln** (B. G. Teubner, Leipzig, 1907).

[75] L. H. Thomas, Proc. Camb. Phil. Soc. **23**, 542 (1927).

[76] E. Fermi, Z. Physik **48**, 73, 1928

[77] A. Krabbe *et al.*, ApJ **447**, L95 (1995).

[78] D. Lynden Bell and M. J. Rees, MNRAS **152**, 461 (1971) .

[79] L. D. Landau and E. M. Lifshitz, *Mechanics*, Pergamon Press, 1960.

[80] J. D. Anderson *et al.*, ApJ **448**, 885 (1995).

[81] J. D. Anderson *et al.*, ApJ **464**, 1054 (1996).

[82] J. D. Anderson *et al.*, Phys. Rev. Lett. **81**, 2858 (1998).

[83] J. D. Anderson *et al.*, astro-ph/9903024.

[84] S. Weinberg, *Gravitation and Cosmology*, John Wiley and Sons ed. (1972).

[85] G. Öyvind and H. Soleng, ApJ **456**, 415 (1996).

[86] D. R. Mikkelsen and M. J. Newman, Phys. Rev. **D16**, 919 (1977).

[87] Ya. B. Zeldovich and I. D. Novikov, *Stars and Relativity*, Relativistic Astrophysics, Vol. 1 (The University of Chicago Press, Chicago. 1971).

[88] M. Demiański, *Relativistic Astrophysics* (Polish Scientific Publishers, Warszawa, 1985) .

[89] R. C. Tolman, *Relativity , Thermodynamics and Cosmology* (Clarendon Press, Oxford, 1934).

[90] J. R. Oppenheimer and G. M. Volkoff, Phys. Rev. **55**, 374 (1939).

[91] S. L. Shapiro and S. A. Teukolsky, *Black Holes, White Dwarfs and Neutron stars* (Wiley Interscience, New York, 1983).

[92] B. K. Harrison, K. S. Thorne, M. Wakano, and J. A. Wheeler, *Gravitation and Gravitational Collapse* (The University of Chicago Press, Chicago, 1965) .

[93] S. Chandrasekhar, *Introduction to the Study of Stellar Structure* (Dover Publications, New York, 1957).

[94] S. Chandrasekhar, MNRAS **95**, 207 (1935).

[95] L. D. Landau, Phys. Zs. Sowjetunion **1**, 285 (1932).

[96] S. Tsuruta and A. G. W. Cameron, Canadian Journ. of Phys. **44**, 1895 (1966).

[97] C. Kettner, F. Weber, and M. K. Weigel, Phys. Rev. D **54**, 1440 (1995).

[98] J. Oort, ARA&A, **15**, 295 (1977).

[99] R. Genzel, D. J. Hollenbach, and C. H. Townes, Rep. Prog. Phys. **57**, 417 (1994).

[100] K. Sellgren, D. N. B. Hall, S. G. Kleinmann, and N. Z. Scoville, ApJ **317**, 881 (1987).

[101] G. H. Rieke and M. J. Rieke, ApJ **330**, L33, (1988).

[102] J. T. McGinn, K. Sellgren, E. E. Becklin, and D. N. B. Hall, ApJ **338**, 824 (1989) .

[103] K. Sellgren, M. T. McGinn, E. E. Becklin, and D. N. B. Hall, ApJ **359**, 112 (1990) .

[104] M. Lindqvist, H. J. Habing, and A. Winnberg, A&A **259**, 118 (1992).

[105] J. H. Lacy, C. H. Townes, and D. J. Hollenbach, ApJ **241**, 132 (1980).

[106] J. H. Lacy, J. M. Achtermann, and E. Serabyn, ApJ **380**, L71 (1991).

[107] E. Serabyn, J. Carlstrom, O. Lay, D. C. Lis, T. R. Hunter, and J. H. Lacy, ApJ **490**, L77 (1997).

[108] A. E. E. Rogers, S. Doeleman, M. C.H. Wright, G. C. Bower, D. C. Backer, S. Padin, J. A. Philips, D. T. Emerson, L. Greenhill , J. M. Moran, and K. I. Kellermann, ApJ **434**, L59 (1994).

[109] T. P. Krichbaum *et al.*, A&A **335**, L106 (1998).

[110] D. C. Backer, in *Unsolved problems in the Milky Way*, eds. L. Blitz and P. Teuben, Proc. of IAU Symp. No. 169 (Dordrecht: Kluwer) (1996).

[111] M. J. Reid *al. 1999*, ApJ submitted, astro-ph/9905075

[112] H. C. Ford, R. J. Harms, Z. I. Tsvetanov, G. F. Hartig, L. L. Dressel, G. A. Kriss, R. C. Bohlin, A. F. Davidsen, B. Margon, and A. K. Kochhar, ApJ **435**, L27 (1994).

[113] R. J. Harms, H. C. Ford, Z.I. Tsvetanov, G. F. Hartig , L. L. Dressel, G. A. Kriss, R. Bohlim, A. F. Davidsen, B. Margon, and A. K. Kochhar, ApJ **435**, L35 (1994).

[114] L. J. Greenhill, D. R. Jiang, J. M. Moran , M. J. Reid, K. Y. Lo, and M. J. Claussen, ApJ **440**, 619 (1995).

[115] M. Myoshi, J. M. Moran, J. Hernstein, L. Greenhill, N. Nakai, P. Diamond, and M. Inoue, Nature **373**, 127 (1995).

[116] F. Melia, ApJ **426**, 577 (1994).

[117] R. Narayan, I. Yi, and R. Mahadevan, Nature **374**, 623 (1995).

[118] F. Melia , ApJL **387**, L25 (1992).

[119] K. M. Menten, M. J. Reid, A. Eckart, and R. Genzel, ApJ **475**, L111 (1997).

[120] P. Predehl and J. Trümper, A&A **290**, L29 (1994).

[121] M. Merc *et al.* , Astron. Astrophys. Suppl. **120**, 465 (1996).

[122] H. Falcke *et al.*, ApJ **499**, 731 (1998)

[123] H. Falcke. K. Mannheim, and P. Biermann, A&A **278**, L1 (1993) .

[124] H. Falcke and P. I. Biermann, A&A **308**, 321 (1996).

[125] H. Falcke, astro-ph/9909439

[126] T. Beckert and W. J. Duschl, A&A **328**, 95 (1997).

[127] R. Narayan, R. Mahadevan, J. E. Grindlay, R. G. Popham, and C. Gammie, ApJ **492**, 551 (1998).

[128] F. Mahadevan , Nature **394**, 651 (1998) .

[129] T. Manmoto, S. Mineshige, and M. Kusunose, ApJ **489**, 791 (1997) .

[130] R. Narayan and I. Yi, ApJ **452** , 710 (1995).

[131] M. A. Abramowicz, X. Chen, S. Kato, J. P. Lasota, and O. Regev, ApJ **438**, L37a (1995).

[132] G. S. Bisnovatyi-Kogan and R. V. E. Lovelace, astro-ph/9902341.

[133] R. Blandford and M. C. Begelman, MNRAS **303**, L1 (1999)

[134] R. D. Davies, D. Walsh, and R. S. Booth , MNRAS **177**, 319 (1976).

[135] K. Y. Lo *et al.* , Nature **315**, 124 (1985) .

[136] K. Y. Lo *et al.* , Nature **362**, 38 (1993).

[137] G. C. Bower and D. C. Backer, ApJ **496**, L97 (1998).

[138] J. W. Moffat, astro-ph/9704232 .

[139] G. G. Raffelt, Ann. Rev. Nucl. Part. Sci. **49**, to be published, hep-ph/9903472.

[140] J. J. Perry and R. Williams, MNRAS **260**, 437 (1993) .

[141] J. Frank , A. King, and D. Raine, *Accretion Power in Astrophysics* (Cambridge Univ. Press, Cambridge 1992).

[142] S. P. Reynolds and C. F. McKee, ApJ **239**, 893 (1980).

[143] W. H. Press, B. P. Flannery, S. A. Teukolsky, and W. T. Vetterling, *Numerical Recipes*, (Cambridge University Press, 1986).

[144] S. Chandrasekhar , MNRAS **93** , 390 (1933).

[145] M. Abramowitz and I. S. Stegun (eds.), *Pocket Book of Mathematical Functions*, (Verlag Harri Deutsch, Frankfurt, 1984).